Soft x-ray spectroscopy
of organic molecules and liquids

Dissertation zur Erlangung des
naturwissenschaftlichen Doktorgrades
der Julius-Maximilians-Universität Würzburg

vorgelegt von

Oliver Fuchs
aus Ochsenfurt

Würzburg 2009

Eingereicht am: 25.02.2009

bei der Fakultät für Physik und Astronomie

1. Gutachter: Prof. Dr. E. Umbach

2. Gutachter: Prof. Dr. K. Fauth

der Dissertation.

1. Prüfer: Prof. Dr. E. Umbach

2. Prüfer: Prof. Dr. K. Fauth

3. Prüfer: Prof. Dr. G. Reents

im Promotionskolloquium.

Tag des Promotionskolloquiums: 12.06.2009

Doktorurkunde ausgehändigt am:

CURRICULUM VITAE

Persönliche Daten

Name:	Fuchs
Vornamen:	<u>Oliver</u> Karl
Geburtsdatum:	21. März 1975
Geburtsort:	Ochsenfurt
Familienstand:	verheiratet, zwei Kinder

Ausbildung und Beruf

1985 – 1994:	Gymnasium Marktbreit, Abitur
1994 – 1995:	Grundwehrdienst in Ingolstadt
1995 – 2001:	Studium der Physik, Universität Würzburg, Diplom mit Auszeichnung
	Thema der Diplomarbeit: *Resonante inelastische Röntgenstreuung an Berylliumsulfid*
2002 – 2008:	wissenschaftlicher Angestellter der Universität Würzburg, Experimentelle Physik II
seit März 2008:	Entwicklungsingenieur bei der Robert Bosch GmbH

Zusatzqualifikationen

Juni – August 1999:	Auslandspraktikum am M.I.T., Cambridge
Sept. 2002:	Teilnahme an der "3. Dresdner Sommerschule Mikroelektronik"

CONTENTS

INTRODUCTION AND OUTLINE

This thesis focuses on the investigation of the electronic structure of organic molecules, which have attracted considerable attention in the last decade. The intense research activities related to these materials have two main motivations: On the one hand, organic molecules have a technological application as the building blocks of organic semiconductors. Working transistors [1], solar cells [2], and especially optoelectronic devices [3, 4] based on organic materials were produced in the last decade. In order to cost-effectively produce optimized organic electronic devices, a fundamental knowledge of the electronic properties of the overwhelming manifold of organic molecules and the metal-organic interface is necessary. Therefore, many studies of the electronic structure of potential candidates for organic electronics exist. Two of these candidates, namely C_{60} (the 'Buckminsterfullerene') and 3,4,9,10-perylene tetracarboxylic acid dianhydride (PTCDA), which also acts as a model system for many fundamental studies of organic molecules [5–17], are investigated in this thesis.

On the other hand, organic molecules are the functional elements in biological systems. A detailed understanding of the interaction of bio-molecules in aqueous solution with each other, with the solvent, i.e. water, and with other solutes (e.g. ions) is essential for the life sciences. Since many biologically important interactions are related to steric properties of these bio-molecules, the subject of many investigations is the geometric structure of bio-molecules, and especially proteins, carried out by x-ray crystallography on protein crystals and nuclear magnetic resonance spectroscopy on protein solutions. However, in many cases, the knowledge of their geometry is not sufficient to understand the behavior of biological macromolecules. An example is the denaturation of proteins due to the presence of salts. The denaturation strengths of salts follow the Hofmeister series known since 1888, but it still defies a comprehensive explanation [18, 19]. Another example is the yet unknown mechanism of the selective permeation of ion channels in bio-membranes [20, 21].

Since all (bio-)chemical interactions are ultimately of electronic nature, the knowledge of the microscopic electronic interactions is often the missing key to understand the biologically relevant behavior. And, like for all solutes, the electronic structure of bio-molecules is heavily influenced by the solvent (forming a solvation complex) and other solutes, like salts. Therefore, it is necessary to study the electronic structure of bio-molecules in their native environment, namely in aqueous solution.

As the study of the electronic structure of liquids is a very young field of research, the necessary equipment is not yet commercially available, and only few scientific results on comparatively simple liquids are reported in literature. X-ray-induced damage effects further exacerbate the already very restrictive requirements to the experimental techniques and the instrumentation used. Consequently, the technical developments necessary to investigate the fascinating world of liquids and organic molecules are a fundamental part of this thesis, and the studied systems therein are naturally among the more basic examples, far from the enormously complex biologically active macromolecules like proteins or even bio-membranes. In the beginning, some inorganic liquids were investigated: water (H_2O), heavy water (D_2O), sodium hydroxide (NaOH) and sodium deuteroxide (NaOD) solutions. The next step towards biologically relevant molecules were preliminary pH-dependent studies of amino acid solutions, since amino acids are the building blocks of peptides and proteins.

The thesis is organized as follows: in Chapter 2, the applied soft x-ray photon-in photon-out techniques are introduced and the novel experimental approach of recording comprehensive 2-dimensional resonant soft x-ray scattering maps is developed. Chapter 3 describes the two main pieces of instrumentation emerging from this work: a high-transmission soft x-ray spectrometer and a temperature-controlled flow-through liquid cell. Chapter 4 contains the presentation and discussion of the experimental results: in Section 4.1, the novel possibilities of the high-transmission x-ray spectrometer are demonstrated with the study of the electronic structure of C_{60}, and Section 4.2 is dedicated to the symmetry-resolved study of the electronic structure of PTCDA. Afterwards, the above-mentioned liquids were investigated, with the focus on water in Section 4.3, and on the amino acid solutions at different pH-values in Section 4.4. The Appendix contains technical detail information on the methods developed for the design of the new spectrometer and important hints on its calibration and usage.

SPECTROSCOPIC METHODS

In this thesis exclusively soft x-ray 'photon-in photon-out' methods were used. These techniques probe the local partial density of states (LPDOS). They turned out to be an excellent choice for the investigated material systems, as will be motivated in the respective Sections.

X-ray absorption spectroscopy (XAS) probes the unoccupied states, while x-ray emission spectroscopy (XES) yields information on the occupied states. Resonant inelastic x-ray scattering (RIXS, see Section 2.2) offers combined information of all valence states, both occupied and unoccupied. These experimental techniques require a 3rd generation synchrotron source with tunable monochromatic photon energy and high intensity. The experiments were performed at beamline U41 PGM at BESSY, Berlin, Germany and at beamline 8.0 of the Advanced Light Source (ALS), Berkeley, USA. Combined with the latter, the novel x-ray spectrometer described in 3.1 allows to record comprehensive 2-dimensional RIXS maps (see Section 2.3.1). The examples discussed in Sections 4.1 and 4.3 demonstrate, that this novel approach yields an unprecedentedly detailed picture of the electronic structure. For these RIXS maps, the differentiation between XAS, XES and RIXS as experimental methods is no longer sensible, since a RIXS map contains a multitude of XAS, XES, and RIXS spectra in one data set. In this Chapter, however, we will still distinguish between XAS, XES and RIXS in order to introduce the fundamental physics step by step.

All three methods are based on the two processes illustrated in Fig. 2.1, namely excitation of a core electron to an unoccupied state or into the continuum by an x-ray photon (absorption), and subsequent radiant de-excitation of an electron from occupied valence states into the core vacancy (emission). Both processes are dipole transitions and therefore follow dipole selection rules. In the case of narrow-band resonant excitation, these two transitions have to be treated as a single quantum mechanical photon scattering process (the RIXS process as discussed below) in order to explain the experimental findings.
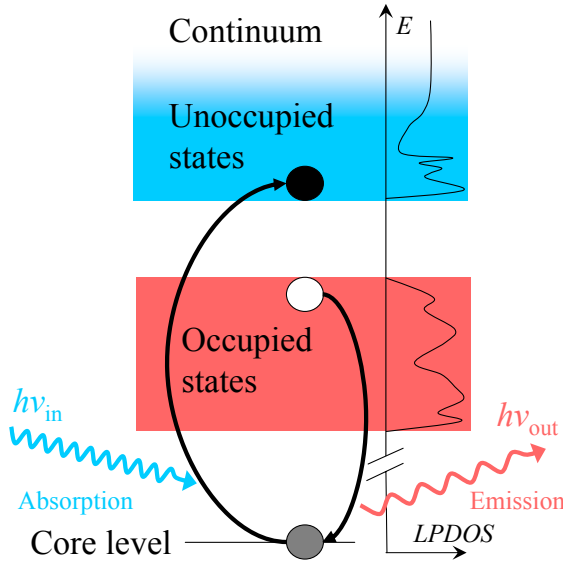
Figure 2.1: Energy diagram of the absorption and emission processes relevant for XAS, XES, and RIXS.

2.1 X-ray absorption and emission spectroscopy

X-ray absorption spectroscopy (XAS) gives information on the unoccupied density of states by measuring the absorption probability of an x-ray photon as a function of the photon energy $h\nu_{in}$, while x-ray emission spectroscopy (XES) probes the occupied density of states by recording the emission probability as a function of $h\nu_{out}$. The electronic transitions involved in the absorption and emission processes are illustrated in Fig. 2.1. In first order perturbation theory, the probability $W_{i \to f}$ for a transition from the initial state i to the final state f caused by a perturbation Hamiltonian $\mathbf{H}'$ is governed by the transition matrix element $\langle f|\mathbf{H}'|i\rangle$ as derived by Dirac in 1927 [22]:

$$W_{i \to f} \propto |\langle f|\mathbf{H}'|i\rangle|^2 \delta(E_f - E_i \mp h\nu). \tag{2.1}$$

Dirac's δ-function ensures energy conservation. Note that for absorption the minus sign has to be used, while the plus sign describes the emission process.

Disregarding multi-photon processes (which can safely be done for synchrotron radiation) and applying the dipole approximation yields:

$$W_{i \to f} \propto \left|\sum_k \langle f|\hat{\mathbf{e}}\mathbf{x}_k|i\rangle\right|^2 \delta(E_f - E_i \mp h\nu). \tag{2.2}$$

The sum accounts for all electrons k at positions $\mathbf{x}_k$ interacting with the photon field, the polarization vector of which is $\hat{\mathbf{e}}$. The dipole approximation considers the electric field to be constant over the spatial distribution of the affected electron

wave functions, which is a sufficiently good approximation for our purpose, since the smallest wavelength used in this work is 2.3 nm at 550 eV, much larger than a *1s* orbital and also significantly larger than a molecular orbital for the studied molecules. However, in angle-resolved photoemission studies of molecules in gas phase, differences in the experimental angular distribution compared to theoretical dipole calculations were detected even for photon energies below 100 eV [23–26]. Such deviations from the dipole approximation are of no relevance for this work.

If we integrate Equation 2.2 over all possible valence states while accounting for the energy-restricting δ-function, we get an expression for the spectral XAS intensity $I_{\mathrm{XAS}}(h\nu_{\mathrm{in}})$, also known as *Fermi's Golden Rule* [27]:

$$I_{\mathrm{XAS}}(h\nu_{\mathrm{in}}) \propto \left| \sum_k \langle f| \hat{\mathbf{e}}\mathbf{x}_k |i\rangle \right|^2 \rho_f(E_f) \text{ with } E_f = E_i + h\nu_{\mathrm{in}}. \qquad (2.3)$$

and for XES:

$$I_{\mathrm{XES}}(h\nu_{\mathrm{out}}) \propto \left| \sum_k \langle f| \hat{\mathbf{e}}\mathbf{x}_k |i\rangle \right|^2 \rho_i(E_i) \text{ with } E_i = E_f + h\nu_{\mathrm{in}}. \qquad (2.4)$$

Since the spectral intensities in Equations 2.3 and 2.4 are weighted with the dipole transition matrix elements, only states having a local overlap with the localized core state are accessible. Furthermore, transitions involving states with certain symmetries are not allowed due to vanishing matrix elements. Therefore only the *local partial* density of states (LPDOS) is probed by XAS and XES, as illustrated in Fig. 2.1. This is a valuable feature, since it makes these methods very specific, far beyond the intrinsic sensitivity for a chemical element: by choosing an excitation energy which resonantly excites a certain species of molecules or an atom at a specific site within a molecule, the local specificity of the XES technique will only allow emission from this distinct species or site. Additional symmetry-specificity is accessible for well-oriented samples: the appropriate choice of the direction of the electric field vector with respect to the sample selects certain symmetries of valence states. Only orbitals of these symmetries can then participate in the excitation or emission process. In this work, examples of site- and symmetry-selective XES and XAS spectra can be found for C_{60} and PTCDA molecules in Sections 4.1 and 4.2.

According to the final-state rule [28–30], the observed spectra represent the LPDOS of the final state, i.e. for XAS the spectrum is influenced by core hole effects (e.g. excitons), while the XES spectrum does not reflect the core hole, but a valence hole instead, similar to photoemission spectroscopy (PES). Therefore, XES spectra can be conveniently interpreted in a one-electron picture on the basis of ground
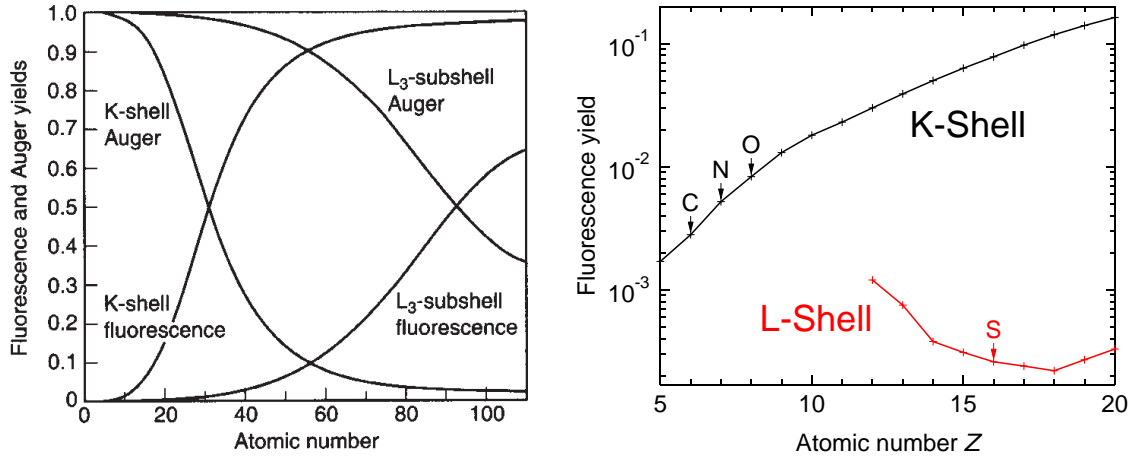
Figure 2.2: Left: Comparison of the fluorescence and the competing Auger yields for K and L core levels as a function of the atomic number Z (taken from [35]). Right: The fluorescence yield of light elements. The elements relevant for this work (C, N, O, and S) are marked. Numbers taken from [36].

state calculations, while for XAS the more complicated calculation of the core-excited final state is necessary. A simplification is the $Z+1$ approximation [31], for which the static influence of the additional positive charge is mimicked by replacing the excited atom by an atom with the next higher atomic number $Z + 1$ in the calculations .

When recording an XAS spectrum over a wide energy range above the absorption edge, the wave function of the ejected electron gets backscattered by adjacent atoms, causing oscillations in the absorption coefficient which carries information on the next-neighbor distances. This method is called EXAFS (extended x-ray absorption fine structure) [32] and is in principle applicable to liquids with the newly developed equipment described in Chapter 3. However, for the past experiments the stability of the synchrotron beam was not sufficient over the required wide energy range. Meanwhile these purely technical problems are solved, so in future experiments it might be possible to determine next neighbor distances in liquids without the need for additional instrumentation. This is especially interesting for collecting information on water and aqueous solutions, since EXAFS has proven to be sensitive even to hydrogen atoms, as EXAFS studies on ice demonstrate [33, 34]. In contrast, for the spectroscopic methods of XES and XAS, hydrogen atoms are invisible due to their low x-ray scattering cross section.

The XES process is not the only possible relaxation of the core excitation. The non-radiant Auger decay is much more likely for light elements, as Fig. 2.2 shows. It compares the fluorescence with the competing Auger yield as a function of the atomic number (left graph). In this thesis, the K-shell of elements with atomic

numbers Z between 6 and 8 (carbon, nitrogen and oxygen) and the L-shell of sulfur (Z=16) were used. The fluorescence yields of these elements are marked with tags in the right panel of Fig. 2.2, which shows a close-up view of the light elements. In our case, the respective fluorescence yields range between $2 \cdot 10^{-4}$ (S L) and $8 \cdot 10^{-3}$ (O K). This is the reason, why a high-brightness source and a spectrometer with a high detection efficiency are so important for XES.

A detailed introduction to XAS can be found in [31], and a discussion of the combined possibilities of XAS and XES in [37–40].

2.2 Resonant inelastic x-ray scattering

Many resonant effects such as site-, species-, and symmetry-selective XES and XAS can be readily explained by the theoretical framework of the previous Section 2.1, which describes the absorption and emission as two independent dipole transitions. However, some experimental observations are a manifestation of the interference of the combined excitation and emission event, which can only be explained by treating the excitation and emission as one single quantum mechanical photon scattering process (called RIXS or sometimes 'electronic Raman scattering'). This is a typical quantum mechanical phenomenon: if the system remains undisturbed between excitation and de-excitation and, in particular, if no attempt is made to identify the intermediate state, all alternative intermediate states leading to the same observable final state interfere with each other, carrying information about the excitation which can influence the emission process. Examples of such information, which could not be conveyed by an intermediate state with a single localized core hole, are the parity in centro-symmetric molecules or the crystal momentum in solid state samples. Both cases will be discussed in detail below.

This description as a photon scattering process requires second order perturbation theory, leading to the Kramers-Heisenberg formalism [41]. The application of this formalism to resonant effects in XES spectra was first proposed by Y. Ma *et al.* [42, 43]. Since the intermediate state was historically treated by H.A. Kramers and W. Heisenberg as infinitely sharp (i.e. with an infinite lifetime), it was later modified by V. Weisskopf and E. Wigner for intermediate states with finite lifetime [44]. This modification results in the following resonant term, as developed in detail in [45]:

$$I_{\mathrm{RIXS}}(h\nu_{\mathrm{in}}, h\nu_{\mathrm{out}}) \quad \propto \quad \frac{\nu_{\mathrm{out}}}{\nu_{\mathrm{in}}} \sum_f \sum_m \frac{\left|\langle f|\mathbf{p} \cdot \hat{\mathbf{e}}_{\mathrm{out}}|m\rangle \langle m|\mathbf{p} \cdot \hat{\mathbf{e}}_{\mathrm{in}}|i\rangle\right|^2}{(E_m - E_i - h\nu_{\mathrm{in}})^2 + \Gamma_m^2/4}$$

$$\cdot \delta(h\nu_{\mathrm{in}} - h\nu_{\mathrm{out}} - E_f + E_i), \tag{2.5}$$
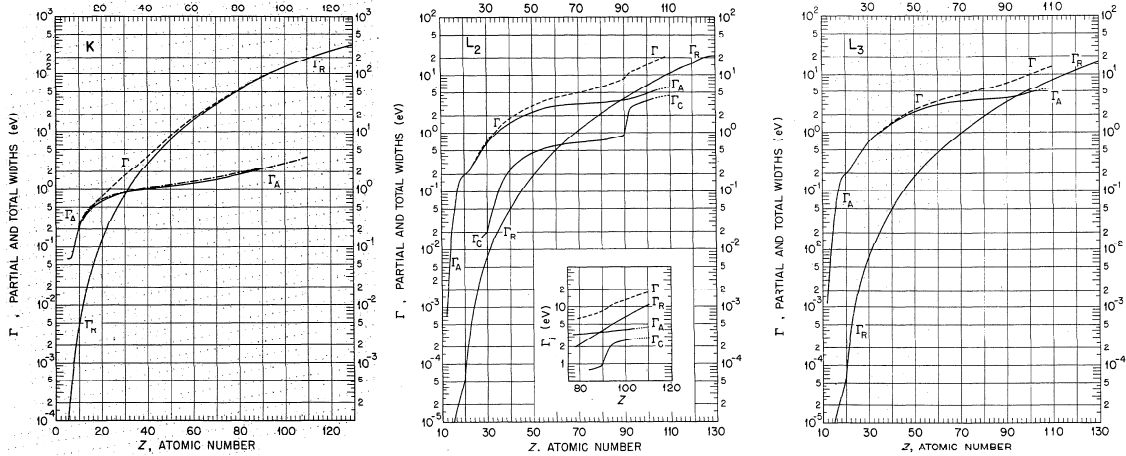
Figure 2.3: Total (Γ) and partial line widths of the K- (left), L_2- (middle), and L_3-shell (right). Γ_A and Γ_C are the Auger-limited line widths, which dominate for light elements compared to the radiation-limited line width Γ_R. Graphs taken from [36].

where i, m, and f are initial, intermediate, and final state (since in our case i is the ground state, we sum only over all possible m and f). The δ-function strictly determines the energy of the emanating photon, while the incident photon energy $h\nu_\text{in}$ can be detuned within the limits of Γ_m. It is the full width at half maximum (FWHM) of the Lorentzian broadening of the intermediate state due to its finite lifetime τ_m according to Heisenberg's uncertainty principle:

$$\tau_m \Gamma_m \geq \hbar. \tag{2.6}$$

The condition for the *on-resonance* case [46] is a small delimiter in Equation 2.5, i.e. $|E_m - E_i - h\nu_\text{in}| \leq \Gamma_m$. Resonance effects which can only be explained by a one-step scattering process, are detected with high intensity if this condition is met.

The lifetime broadening of the core-excited state is proportional to its decay rate. Possible decay mechanisms are the non-radiative Auger-process and the radiative fluorescence decay. Fig. 2.3 (taken from [36]) gives approximate lifetime-limited line widths of core-excited intermediate states as a function of the atomic number Z for the relevant K- and $L_{2,3}$-shells. For the light elements studied in this work ($Z = 6, 7, 8, 16$), the total width Γ is strongly dominated by the Auger-limited widths Γ_A and Γ_C, which is another manifestation of the overwhelming Auger yield for light elements compared to the radiative decay as discussed in Section 2.1. Γ_C is the width limited by Coster-Kronig transitions, which are a special group of Auger processes. Newer experiments [47–50] confirm the total lifetime widths given by Krause *et al.* [36, 51] of 100 meV (lifetime of 6.6 fs) for the carbon *1s* hole,
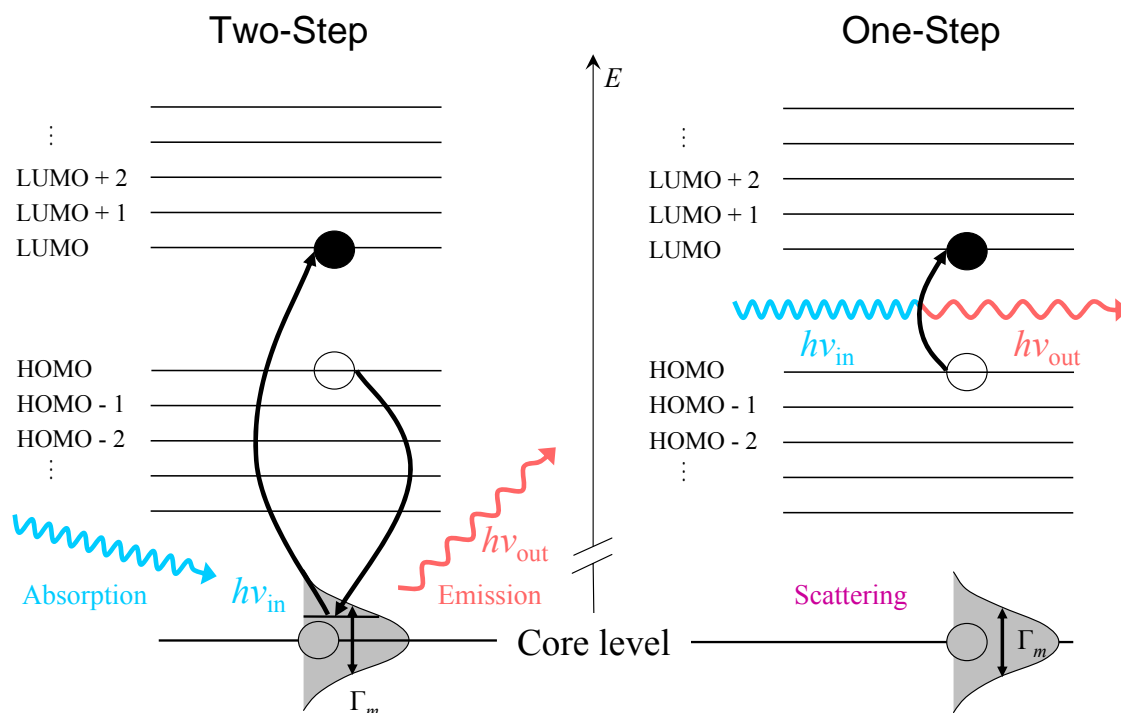
Figure 2.4: Two different views of the same HOMO–LUMO transition with detuned excitation. Left: Two-step model of excitation and emission. Right: One-step photon scattering process.

120 meV (5.5 fs) for the nitrogen *1s* hole, 190 meV (3.5 fs) for the oxygen *1s* core hole, and 60 meV (11.0 fs) for sulfur *2p*.

The important difference of the Kramers-Heisenberg formalism compared to the simpler two-step model is the occurrence of a mixed second-order term, which allows several alternative intermediate states to interfere with each other. In the two-step model, the absolute values of the two transition matrix elements are squared before multiplication, which does not allow for interference of alternative intermediate states. Fig. 2.4 illustrates the two different views by the example of a HOMO–LUMO (highest occupied molecular orbital to lowest unoccupied molecular orbital) transition in a molecule, mediated by the core state, which is represented by a Lorentzian peak with the width Γ_m due to lifetime broadening, making detuned excitation possible. The left side shows absorption and emission as two subsequent transitions, while in the right diagram, a single scattering event is depicted, i.e., the photon is scattered rather than absorbed and re-emitted, thereby losing the amount of energy required to excite an electron from the HOMO to the LUMO. However, when looking at the one-step scattering process, one should not forget, that an appreciable scattering cross section is only available to photons with an energy close to an allowed electronic transition, in our case the *1s* to LUMO transition.

Both descriptions are indistinguishable, since the energy balance is the same, always leading to an emitted photon energy of:

$$h\nu_{\text{out}} = h\nu_{\text{in}} - E_{\text{LUMO}} + E_{\text{HOMO}}. \tag{2.7}$$

In the following, frequently observed effects based on (and only explained by) the one-step Kramers-Heisenberg formalism, are briefly described.

2.2.1 Raman shift

The energy-loss of the photon $h\nu_{\text{in}} - h\nu_{\text{out}}$ is called *Raman shift*, if it is constant over an extensive excitation energy range. Slightly below the absorption edge, this effect is characteristic of RIXS and can be observed for most sample systems (compare Sections 4.1 and 4.3). It is the direct consequence of the Lorentzian resonance condition and the energy-conserving δ-function of Equation 2.5. Since the lifetime broadening of the intermediate state allows for detuned excitation into short-lived so-called *virtual* states, the emitted photon energy, which is governed by the δ-function, has to make up for the detuned excitation, i.e. the excitation process can 'borrow' small amounts of energy from the emitted photon and vice versa within the limitations of Heisenberg's uncertainty principle, leading to a shift in the emission spectrum for detuned excitation, as previously illustrated in Fig. 2.4 for a HOMO–LUMO transition with a resulting emitted photon energy given by Equation 2.7. In the excitation energy window, in which this process is resonantly enhanced, the emission energy shifts parallel with the excitation energy, i.e. with a constant energy difference of $E_{\text{LUMO}} - E_{\text{HOMO}}$. Within this work, the Raman shift is most obvious for the C_{60} molecule (Section 4.1).

2.2.2 Elimination of lifetime broadening

An interesting property of the energy balance of the scattering process is its independence from the core state energy (compare Equation 2.7 and the right energy diagram in Fig. 2.4). This allows in principle to acquire both XAS and XES spectra with a resolution better than the lifetime broadening of the core-excited state. A prerequisite for eliminating the lifetime broadening in XAS is an isolated sharp occupied valence state ψ_O, while for XES an isolated sharp unoccupied state ψ_U is required. 'Isolated' in this context means, that there are no adjacent states within the lifetime width Γ_m, and 'sharp' means sharper than Γ_m. Further, the combined experimental resolution of beamline and spectrometer has to be better than Γ_m. In the ideal limit of infinitely sharp ψ_O and ψ_U, a partial fluorescence yield XAS scan

with the emission energy detection window smaller than the lifetime broadening right at the ψ_O emission energy then results in an XAS spectrum with an energy resolution merely limited by the combined experimental resolution of beamline and spectrometer. The same is true for an XES spectrum excited sharply at the ψ_U absorption energy. In practice, this is only feasible for elements with high atomic numbers Z, since, as can be seen in Fig. 2.3, the lifetime broadening of their core-excited state is high enough to be beaten by the experimental resolution. For XAS, this was first demonstrated at the Dysprosium L_3-edge [52].

2.2.3 The parity selection rule for centro-symmetric molecules

In addition to the symmetry-selectivity of the dipole selection rules introduced in Section 2.1, the parity selection rule applies to molecules with inversion symmetry [53]. It can be observed in the RIXS spectra of C_{60} (Section 4.1). This rule states, that for excitation to a *gerade* (centro-symmetric) unoccupied orbital, emission is only allowed from a *gerade* occupied state, and for excitation to an *ungerade* state, emission is allowed only from an *ungerade* state. In the two-step model, this rule can not be explained, since the localized core hole of the intermediate state breaks the molecular symmetry, if it is not located right at the inversion center. And for an intermediate state without defined parity, no parity-derived selection rule exists for the emission process. However, in the one-step model and for coherent excitation of all identical atoms within the molecule, the intermediate state is a linear combination of all wave functions belonging to possible excited states, which interfere with each other as long as they remain undisturbed. Such an intermediate state is delocalized over all identical atoms and possesses the symmetry of the molecule, conveying the parity information of the excited electron to the emission process [45].

2.2.4 Crystal momentum-selective RIXS in solids

Another resonant effect which can only be explained on the basis of a one-step scattering process is the conservation of the crystal momentum k in solids. This was first found and interpreted by Y. Ma *et al.* [42, 43, 54], and allows for k-selective x-ray emission, which is the prerequisite for band structure studies. The theoretical framework is again provided by the Kramers-Heisenberg formalism (equation 2.5). If the excitation is coherent over many lattice unit cells, the intermediate state is a linear combination of all wave functions belonging to possible core-excited states at all coherently illuminated atoms. This linear combination is delocalized over
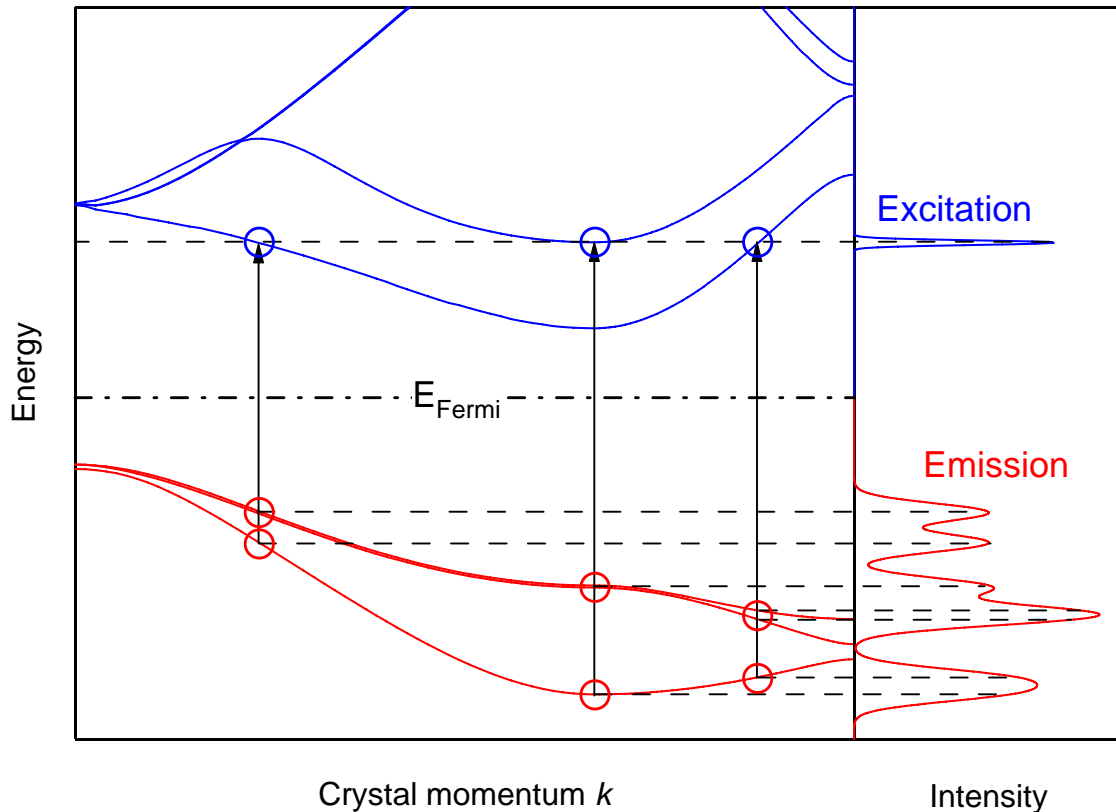
Figure 2.5: The bandmapping concept of RIXS. All transitions are marked with blue (excitation) and red (emission) circles. The excitation energy selects possible k-vectors (vertical arrows), and due to k-conservation, emission is only allowed from the same place in the Brillouin zone.

several unit cells, having the form of periodic Bloch wave functions therein. As such, they carry a defined crystal momentum as long as no disturbance breaks the equivalence of the coherently excited atoms.

If the momentum transfer of the x-ray photon involved in the RIXS process can be neglected, k is conserved during the scattering, i.e., the emission must take place at the same position in the 3-dimensional Brillouin zone of the reduced zone scheme as the excitation. In the one-step scattering picture, only k-conserving ('vertical') transitions can take place. This situation is illustrated in Fig. 2.5.

A review paper with a detailed introduction and examples of band structure mapping was written by S. Eisebitt and W. Eberhardt [55].

2.2.5 RIXS dynamics

The lifetime of the core-excited state, which is a few femtoseconds for light elements (see Section 2.2), can be used as 'core hole clock' in order to study dynamics taking place on the same timescale. In this work, examples for such dynamics are the dissociation of water molecules in Section 4.3, vibrational symmetry-breaking in the C_{60} molecule (Section 4.1), and electron-phonon scattering in solids, leading to an incoherent fraction in RIXS spectra of band structure studies (introduced in Section 2.2.4). If the core hole lifetime is known, the characteristic time governing the dynamics (also called 'dephasing time') can often be determined from the RIXS spectra [54–57]. In addition, it is possible to artificially shorten the core hole lifetime by detuning the excitation energy according to Heisenberg's uncertainty principle in Equation 2.6.

A RIXS study of the dissociation of HCl molecules dynamics is reported in [58]. Since the intermediate state of HCl is dissociative, the atoms will start to move apart as a consequence of the electronic excitation. Especially hydrogen atoms can move sufficiently far during the core hole lifetime for a significant change in the resulting emission spectra. Then, the emission spectrum is composed of two contributions: a molecular fraction with a still significant overlap of electron density between the atoms, and a dissociated atomic fraction with negligible overlap, i.e. the molecular bond is no longer existent. This concept, which will be referred to in Section 4.3, is based on the final state rule introduced in Section 2.1: the final state with the displaced protons is reflected in the emission spectra. Upon detuning the excitation energy in [58], the molecular fraction increases: the more detuned the excitation energy, the shorter the core hole lifetime (Equation 2.6) and the less emission from dissociated molecules occurs.

Another application of the core hole clock can be found in [59]. Therein, the characteristic time of charge transfer screening of N_2 on graphite was determined.

In order to calculate the characteristic time of dynamics, we have to distinguish between probabilistic and deterministic dynamics. In the former case (e.g. for a quantum mechanical tunneling or scattering process), the dynamics has a constant probability to happen, causing the dynamics to evolve exponential in time. Then, according to [55, 59], the fraction $f_{prob.}$ of the spectral intensity which represents the system before the dynamics took place, is given by:

$$f_{\text{prob.}} = \frac{\tau_{\text{d}}}{\tau_{\text{d}} + \tau_{\text{m}}} \tag{2.8}$$

where τ_{d} is the time constant of the dynamics, while τ_{m} is the lifetime of the intermediate core-excited state. For deterministic or quasi-classical dynamics such

as the ballistic motion of a hydrogen atom, it is more appropriate to consider the dynamics taking a constant time to happen. In this case it is obvious, that the fraction $f_{\text{det.}}$ is given by:

$$f_{\text{det.}} = e^{-\frac{\tau_{\text{d}}}{\tau_{\text{m}}}}. \tag{2.9}$$

Of course, this assumption of a constant duration of the dissociation process is only an approximation for real molecules, since the ongoing molecular vibrations lead to an ensemble of interatomic distances and velocities for the initial state of the electronic excitation. It is also known, that protons can be displaced by tunneling processes rather than by ballistic motion if the potential energy surface has a suitable shape. In such cases, Equation 2.8 applies.

A more detailed introduction into RIXS dynamics is given in [56].

2.3 Experimental details

The first half of Chapter 2 briefly described the theoretical framework of the applied spectroscopic techniques originally developed and published by others. In this Section, we will address the question how the spectral intensities for XES and XAS are measured in practice, with the focus on their application to the systems studied in this work. The methods presented here (namely the RIXS map approach in the soft x-ray regime and the correction of saturation effects in XAS spectra and RIXS maps) were developed in this work.

The resonant XES and fluorescence yield XAS experiments shown in Chapter 4 require a high monochromatic photon flux only delivered by undulator beamlines, which are exclusively available at modern 3rd generation synchrotron sources like the ones used in this work, namely the Advanced Light Source in Berkeley, USA, and BESSY II in Berlin. The use of such bright sources for XES is mandatory due to the minuscule fluorescence yield of light elements discussed in Section 2.1, which is exacerbated by the shortcomings of earlier XES spectrometer designs, in particular their small accepted solid angle and moderate detection efficiency. The latter could be overcome by a novel spectrometer design, which will be introduced in Section 3.1.

In XAS experiments, the photon energy-dependent absorption coefficient $\kappa(h\nu_{\text{in}})$ of the sample, in the following simplified as κ_{in}, is determined. There are several substantially different approaches.

The most direct way is to measure the photon energy-dependent transmission of a thin homogenous sample, since it directly probes the primary process, i.e. the

absorption itself. The transmitted intensity $I_T(h\nu_{in})$ of a sample with a thickness z and an absorption coefficient κ_{in}, illuminated with an intensity I_0 and a photon energy $h\nu_{in}$ is according to Lambert-Beer's law:

$$I_T(h\nu_{in}) = I_0 \cdot e^{-z \cdot \kappa_{in}}. \tag{2.10}$$

The negative natural logarithm of the transmission $I_T(h\nu_{in})/I_0$ is then proportional to the desired absorption coefficient. However, this direct approach is only possible for materials which can be prepared as a very thin homogenous and freestanding film.

In most cases, the absorption event has to be detected indirectly via secondary processes which occur as a consequence of the core hole produced by the absorption event, one of which is the radiant XES process (fluorescence yield (FY) XAS). Other examples are the non-radiant electron-emitting Auger process (electron yield XAS), or the ejection of an ion as a consequence of photon-induced decomposition (ion yield XAS). The excitation energy-dependent rates of these processes normalized to the incident intensity are a measure of the absorption coefficient.

If only particles in a certain energy window are detected, one speaks of *partial* as opposed to *total* yield XAS. In the case of electron yield, this can be used to tune the escape depth. For partial FY, one possible application is the elimination of the lifetime broadening as it has been discussed in Section 2.2.2. Other concepts of partial FY spectra will be discussed in the next Section, since they are some of many possibilities offered by a novel experimental approach introduced there.

2.3.1 RIXS maps

Due to the high detection efficiency of the novel soft x-ray spectrometer presented in Section 3.1, it is possible to record entire 2-dimensional RIXS-maps within 10 to 45 minutes. This concept of recording and displaying the emission intensity as a function of both excitation and emission energy in a 2-dimensional color-coded plot and its potential are introduced in detail in Section 4.1. The good statistics of the RIXS map allows the extraction of emission spectra at any excitation energy, as well as partial fluorescence yield absorption spectra at any emission energy inside the map. This is due to the fact that a RIXS map contains the full electronic information accessible by soft x-ray techniques. Compared to conventional RIXS studies with only a few resonant emission spectra at selected excitation energies, the 2D map is clearly superior, making resonant effects, which are often a complex interplay of both intensity variations and energy shifts, much more apparent and comparatively easy to characterize.
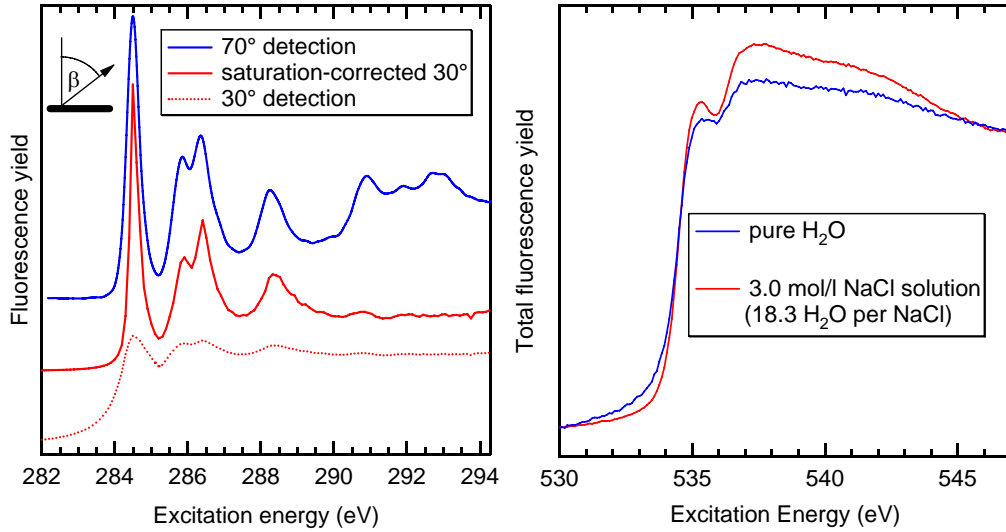
Figure 2.6: Left: Comparison of C K fluorescence yield XAS spectra of C_{60} with incidence angles β of 70° (blue, reproduced from [63]) and 30° (red dotted line). The solid red line is the saturation-corrected version of the latter. Right: O K FY XAS spectra of water (blue) and half-saturated NaCl solution (red).

The extraction of partial fluorescence yield spectra with an arbitrary emission energy detection window is described in literature as 'selective XAS' [40]. Apart from the potential to eliminate the lifetime broadening in XAS spectra as described in Section 2.2.2, species- or site-selective XAS spectra can be extracted, if emission features are present which are indicative of a certain species or a special site. Finally, the intensities of different decay channels can be compared as a function of the excitation energy (decay channel-specific XAS [60]), yielding local information on the wave function overlap of the local partial density of involved electronic states. Examples of such decay channel-specific XAS spectra are shown for the C_{60} molecule in 4.1 together with a detailed analysis of the RIXS map of C_{60}. More RIXS maps can be found in Chapter 4.3 and in [60–62].

2.3.2 Saturation effects in XAS

FY experiments have a large probing depth of hundreds of nanometers, making this detection channel ideally suited for this work, since it allows the study of buried systems like liquids behind a membrane (Sections 4.3 and 4.4). Other often important advantages of the FY are its insensitivity to charging and surface contaminations.

However, the large probing depth of the FY signal leads to a compression of the resulting XAS spectra, called *self absorption* or *saturation* in the literature [64–68].

This effect needs to be addressed in detail, since all absorption measurements (and RIXS maps) in this work are fluorescence yield data and therefore prone to such artifacts. In order to explain and quantify this effect, it is sufficient to consider the simple model of an infinitely thick sample with a smooth surface illuminated with an intensity I_0 of photons of an energy $h\nu_{\mathrm{in}}$. For the sake of simplicity, we first assume normal incidence and detection geometry. The amount of radiation $\delta I_{\mathrm{in}}(h\nu_{\mathrm{in}}, z)$ absorbed in the depth z is given by the negative derivative of Equation 2.10:

$$\delta I_{\mathrm{in}}(h\nu_{\mathrm{in}}, z) = I_0 \cdot \kappa_{\mathrm{in}} \cdot e^{-z \cdot \kappa_{\mathrm{in}}}. \tag{2.11}$$

If A is a constant factor representing the probability per absorbed photon of emitting a photon in the direction of the detector, the intensity $I_{\mathrm{out}}(h\nu_{\mathrm{in}})$ reaching the detector is:

$$I_{\mathrm{out}}(h\nu_{\mathrm{in}}) = \int_0^\infty A \cdot \delta I_{\mathrm{in}}(h\nu_{\mathrm{in}}, z) \cdot e^{-z \cdot \kappa_{\mathrm{out}}} dz = A \cdot I_0 \frac{\kappa_{\mathrm{in}}}{\kappa_{\mathrm{in}} + \kappa_{\mathrm{out}}}. \tag{2.12}$$

Only in the limit of $\kappa_{\mathrm{in}} \ll \kappa_{\mathrm{out}}$, the detected FY signal $I_{\mathrm{out}}(h\nu_{\mathrm{in}})$ is proportional to the sought absorption coefficient κ_{in}, which is the ideal case only reached for ion yield with its extremely short escape depth of a few Å, and, to a lesser extent, for Auger electron yield. For total or secondary electron yield, the saturation effect is often significant, depending on the energy-selectivity of the detector. For FY, the situation is unfavorable: for excitation above the absorption edge, the emitted photons have a constant photon energy below the investigated absorption edge with a lower absorption coefficient κ_{out} than that of the incident beam. In the limit of $\kappa_{\mathrm{in}} \gg \kappa_{\mathrm{out}}$, equation 2.12 tells us, that the FY signal is equal to the upper limit $I_0 \cdot A$, which is a constant. This is due to the fact that in this case all absorption processes (and eventually, all photons from the incident intensity I_0 will be absorbed in the sample) are detected with equal probability A, independent of the depth z in which they occur and independent of the absorption/emission channel. The FY XAS spectrum of C_{60} shown as a red dotted line in the left graph of Fig. 2.6 is clearly an example close to this limit. In such cases, the XAS spectrum is an almost featureless step. In this work, the carbon K edge shows the most severe saturation effects due to its high edge jump. This can be explained by the fact, that most samples contain no elements with edges of lower absorption energies than the carbon K energy.

Fortunately, there are solutions to this problem. For unburied systems, a geometry with normal incidence and grazing emission can be used. In this case, the effective escape depth is reduced to a factor of $\cos \beta$, if β is the emission angle with respect to the surface normal, as defined in the inset on the left side of Figure 2.6. This

will at least lead to a strongly reduced saturation effect, as the comparison of two C_{60} FY spectra in the left graph of Fig. 2.6 with grazing emission angles of 30° (red dotted line) and 70° (blue solid line, reproduced from [63]) demonstrates. In fact, the latter spectrum exhibits the weakest saturation effect of all published electron and fluorescence yield XAS data on C_{60} I had access to. It is clearly superior even to partial electron yield spectra reported in [69].

In the case of liquid solutions, it helps to dilute the solution in order to quench the saturation effect: for low concentrations, two independent effects mitigate the self absorption: 1. κ_{in} and κ_{out} become comparable, and 2. the relative variation of κ_{in} with $h\nu_{\text{in}}$ gets small. The consequences become obvious when expressing the normalized fluorescence yield $Y(h\nu_{\text{in}}) = I_{\text{out}}(h\nu_{\text{in}})/I_0$ as a function of $\frac{\kappa_{\text{in}}}{\kappa_{\text{out}}}$:

$$Y(\frac{\kappa_{\text{in}}}{\kappa_{\text{out}}}) = I_{\text{out}}(\frac{\kappa_{\text{in}}}{\kappa_{\text{out}}})/I_0 = A\frac{\frac{\kappa_{\text{in}}}{\kappa_{\text{out}}}}{1 + \frac{\kappa_{\text{in}}}{\kappa_{\text{out}}}}. \tag{2.13}$$

Since this function can be expanded in a Taylor series around $\frac{\kappa_{\text{in}}}{\kappa_{\text{out}}} = 1$, decreasing the concentration of the solution and thereby lowering the relative variation of κ_{in} leads to the following: the FY signal becomes more and more linear to $\frac{\kappa_{\text{in}}}{\kappa_{\text{out}}}$ and therefore to κ_{in} (since κ_{out} is constant). This effect can be seen in the spectra of lowly concentrated glycine solution at a pH-value of 12 in Section 4.4, which looks identical to the total electron-yield spectrum reported in [70]. Another example is given by the comparison of a liquid water XAS spectrum with that of salt (NaCl) solution on the right side of Fig. 2.6. Since in the case of the NaCl solution, the L-edge of the Cl⁻ ions absorbs below the O K edge at (200 and 270 eV), the ratio $\frac{\kappa_{\text{in}}}{\kappa_{\text{out}}}$ for the O K edge gets smaller compared to the pure water, thereby visibly reducing the saturation effect. However, since the concentration of water is high even in the NaCl solution, the resulting spectrum is still severely compressed, as confirmed by the comparison with spectra in [71].

Besides the two experimental possibilities to mitigate the saturation effects presented above, compressed spectra with a sufficiently high signal-to-noise ratio can be reconstructed afterwards, if an unsaturated spectrum is available in literature. In order to accomplish this, we need the inverse of the function $Y(\frac{\kappa_{\text{in}}}{\kappa_{\text{out}}})$ defined in Equation 2.13:

$$\frac{\kappa_{\text{in}}}{\kappa_{\text{out}}}(Y(h\nu_{\text{in}})) = \frac{1}{\frac{A}{Y(h\nu_{\text{in}})} - 1}. \tag{2.14}$$

This inverse function can be used to obtain $\frac{\kappa_{\text{in}}}{\kappa_{\text{out}}}$ from $Y(h\nu_{\text{in}})$. If the raw spectrum has a constant offset, i.e. if the baseline below the edge is non-zero, it has to be removed prior to the application of this function, since such an offset would
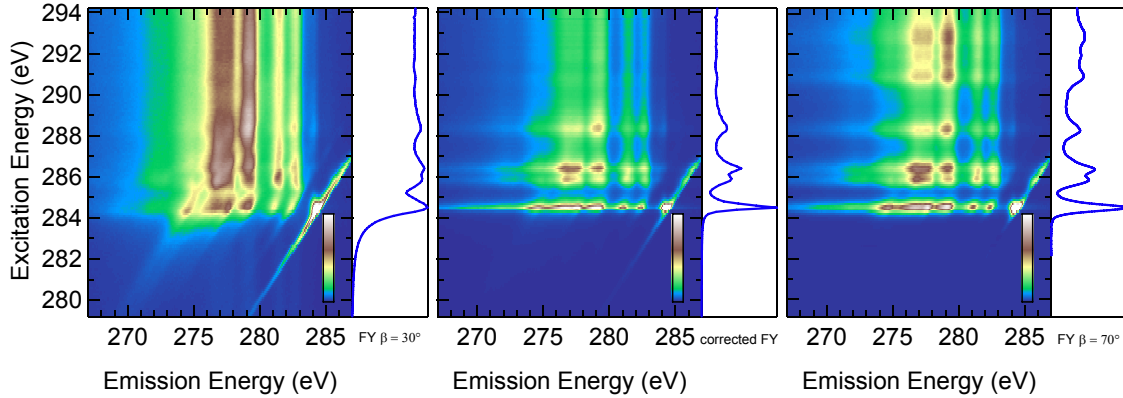
Figure 2.7: The C K RIXS map of C_{60} (left) exhibits strong saturation effects. The same map with the saturation-correction is shown in the middle, featuring a much higher contrast in vertical direction (i.e. as a function of excitation energy). On the right-hand side, the same data is normalized to match the partial fluorescence yield XAS spectrum in [63] taken at a grazing emission angle of $\beta = 70°$. The graphs attached to the right of each map ("absorption spectra") show the integrated intensities of the horizontal lines.

influence the intensity expansion. The correction parameter A contains several factors which are not known with the required precision, namely the probability of the fluorescence decay channel, a geometry factor depending on the detection setup and the relative scaling between I_0 and I_{out}. Valid values of A must be higher than the maximal value of the fluorescence yield spectrum Y_{max}. $A = Y_{max}$ would cause an infinite vertical expansion of the spectrum, while $A \to \infty$ leaves the spectral shape unchanged.

How is the appropriate value of A which leads to the right unsaturated spectral shape found in practice? For this, a quantitative property of the unsaturated spectrum which gets influenced by saturation, must be known. This can be the width of an absorption feature or the intensity ratio of two spectral features. If such a quantitative criterion is known, A can be chosen in an unambiguous way, such that the desired property is matched for the corrected spectrum. Once a good A has been determined, one should be careful when reusing it for other experiments, even if nothing has changed in the experimental setup, since the probability of the fluorescence decay may change with altering the investigated system.

For the demonstration of the correction function and its limitations in Fig. 2.6, the value for A was chosen such that the correction turns the saturated raw spectrum (red dotted line) into a saturation-corrected spectrum (red solid line) which matches an existing unsaturated (or at least weakly saturated) spectrum (shown in blue) as close as possible. While the first resonances below 290 eV are reproduced quite well, the correction is not able to inflate the severely saturated flat line of the raw spectrum (red dotted line) above 290 eV.

With this correction function, it is even possible to correct a whole 2-dimensional RIXS map, as demonstrated in Fig. 2.7. The left side shows the raw RIXS map of C_{60} taken at an emission angle β of 30°, with the intensities of the single horizontal lines (each representing an emission spectrum) normalized to the intensity of the synchrotron beam. This map will be discussed in detail in Section 4.1. Due to strong saturation effects, the vertical contrast is strongly reduced, as discussed above. Applying the correction function yields a much higher vertical contrast, as can be seen in the saturation-corrected version in the center of the same Figure. For comparison, the same data is shown on the right, this time normalized to the partial fluorescence yield XAS signal taken from [63], recorded at a grazing emission angle of $\beta = 30°$. Below an excitation energy of 290 eV, both (center and right panel) are very similar, but above 290 eV, the saturation-correction (center panel) fails. While the grazing emission map (right panel) is a much more realistic representation of the electronic structure of C_{60}, the high contrast does not allow to detect weak features. Therefore, both ways of data acquisition (normal and grazing emission) have their advantages. The optimal way to record such maps with respect to the signal-to-noise ratio is to use a geometry with maximal intensity (i.e. normal emission). The strong saturation effect in this geometry is of advantage for getting high count rates even at excitation energies with low absorption (i.e. below the edge). In order to be able to correct for the saturation effect, an additional XAS spectrum of good quality and low saturation should be recorded. The simplest way is to measure ion or electron yield in parallel with the acquisition of the RIXS map. With such an unsaturated XAS reference, the vertical intensity of the RIXS map can be corrected afterwards. In that case, not even the correction function developed above is required. It is much more straightforward and correct to normalize the integrated intensities of the horizontal lines such that they follow the unsaturated reference signal. The result is the same as taking the whole map with saturation-suppressing geometry (normal excitation, grazing emission, see Section 2.3.2), but with significantly better statistics in map regions with low absorption. In particular, the shape in the horizontal direction (i.e. as a function of emission energy) is independent and unaffected from saturation effects.

DEVELOPMENT OF NOVEL INSTRUMENTATION

Like for all scattering techniques, the success and quality of soft x-ray studies depend on three things: the source (i.e. synchrotron and beamline), the sample (e.g. a liquid contained in a cell), and the detector (in our case the x-ray spectrometer). It turned out to be important that these three components are matched to each other. For the study of light elements in radiation-sensitive samples like organic molecules, it is vital that the photon flux density is kept low even though in our case the fluorescence yield is minuscule, ranging from $2 \cdot 10^{-4}$ to $8 \cdot 10^{-3}$, as shown in Section 2.1.

Thus, the most important requirement is a high detection efficiency, meaning that the optimization process for the whole setup has to start with the x-ray spectrometer, the development of which is described in the next Section. Not only a high throughput and energy resolution are desirable, which are the benchmark numbers the spectrometer designers usually hunt for. It is of equal importance that the optical design allows for a large source spot in order to keep the flux density on the sample low. As an additional benefit, the requirements for the performance and stability of the source (especially the beamline optics) are then less demanding.

In the next step, sample and beamline have to be tailored to the spot size the spectrometer calls for. The former is usually the responsibility of the experimentalist, while the latter requires a flexible beamline design and beamline scientist. Both were found at beamline 8.0 of the Advanced Light Source (ALS). Due to the tireless commitment of the beamline scientist Jonathan Denlinger, the beamline could always be tailored to the changing requirements of the experiment. Recently, the beamline was equipped with bendable mirrors, which are described in more detail in [72]. These allow for maximal flexibility. For example, the optimal spot geometry for liquid cell experiments is 30 x 1000 microns (the vertical dimension is limited by the spectrometer requirements and the horizontal dimension by the
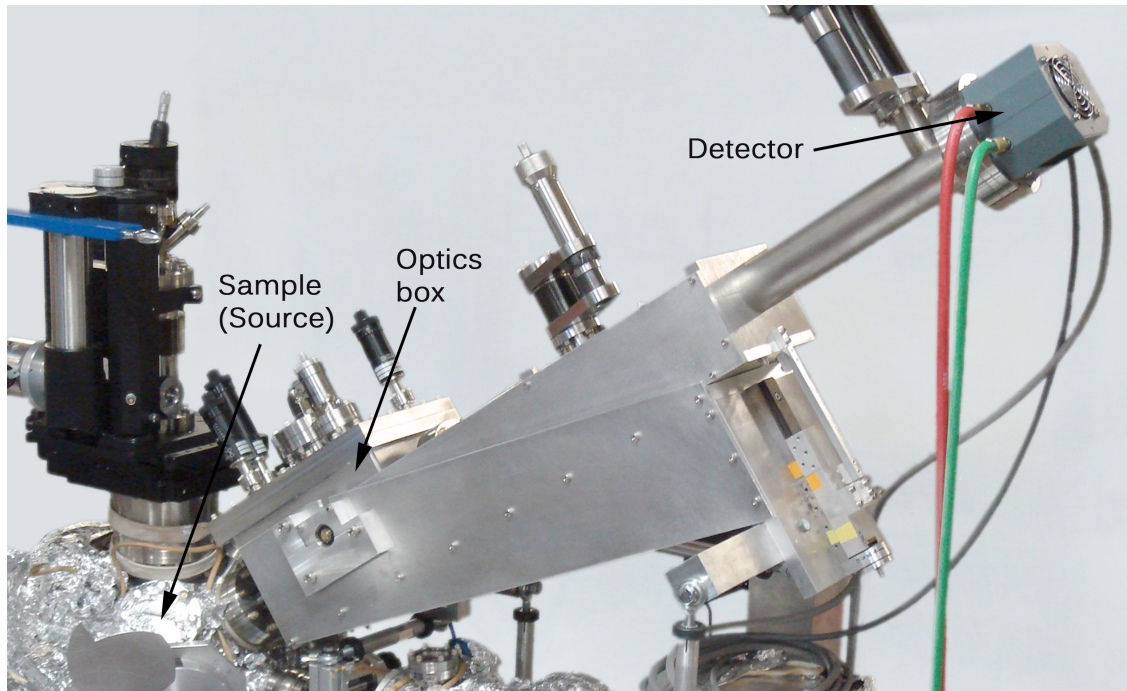
Figure 3.1: Picture of the soft x-ray spectrometer.

window membrane size of 1000 microns). Such an unusual beam geometry can now be easily achieved, since the beamline has two independently bendable mirrors for horizontal and vertical direction.

For the study of liquids presented in Chapter 4, a liquid cell was developed by going through several iterations with many intermediate prototypes. The experience gained during this process taught that the only way to achieve reliable results is a temperature-controlled flow-through cell, as will be described later in this Chapter (3.2 and 3.3).

3.1 High-transmission x-ray spectrometer

An essential step towards the ability to study the electronic structure of radiation-sensitive samples and liquids was the development of a novel XES spectrometer which exceeds the detection efficiency of conventional spectrometers by about two orders of magnitude. It is shown in Fig. 3.1. Since this instrument allows to record comprehensive 2-dimensional RIXS maps, it turned out to revolutionize x-ray emission spectroscopy even beyond the applications discussed in this work, e.g. for band structure studies [60, 61] based on the theoretical framework described
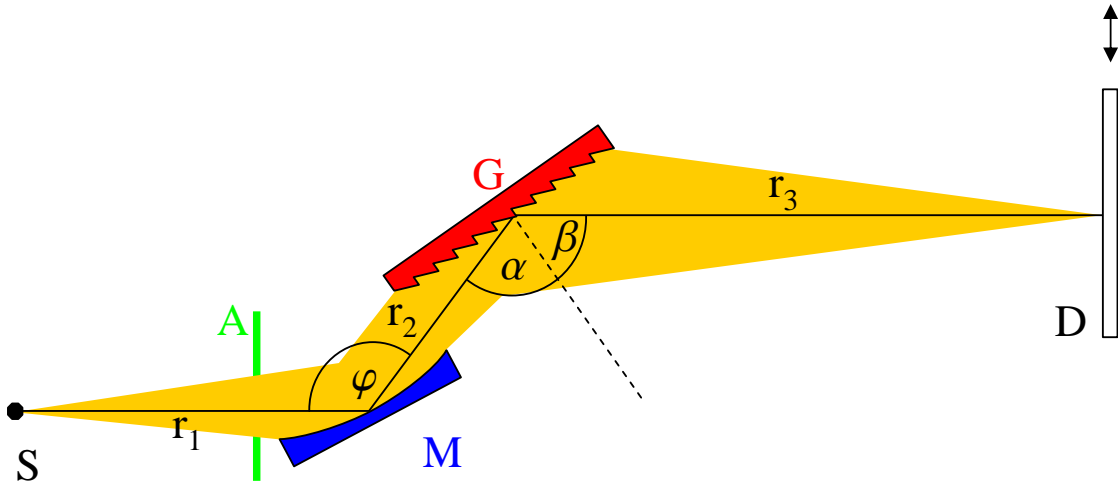
Figure 3.2: Sketch of the optical path of the soft x-ray spectrometer with source **S**. The aperture **A** can be used to mask the spherical mirror **M**. **G** denotes a blazed VLS grating, and **D** a back-illuminated CCD detector in normal incidence geometry.

in Section 2.2.4. The RIXS map concept, which is described in detail in Section 2.3.1, is invaluable for all XES studies with subtle resonant effects. In this work, examples for RIXS maps can be found in Sections 4.1 (C_{60} molecule) and 4.3 (liquid water).

The optical design of the spectrometer covers the photon energy range between 130 and 650 eV and is based on the Hettrick-Underwood principle, i.e., it combines a light-collecting mirror with a variable line space (VLS) grating. The spectrometer is able to record the entire spectral range in one shot, i.e. without any mechanical motion, at a resolving power of 1200 or better. Despite its slit-less design, such a resolving power can be achieved for a source spot as large as (30×3000) μm^2, which is important for keeping beam damage effects in radiation-sensitive samples low.

Most soft x-ray spectrometers (e.g. [74–78]) are based on a grazing incidence spherical grating Rowland circle design [79], while novel concepts often make use of VLS gratings [80–91]. In order to enable RIXS studies of organic and biological samples, a VLS spectrometer based on the work of Hettrick and Underwood [85–89] was designed. Since organic materials mostly consist of sulfur, carbon, nitrogen, and oxygen atoms, the spectrometer is optimized for the S $L_{2,3}$ (150 eV), C K (280 eV), N K (400 eV), and O K (525 eV) edges. The major design goal was to yield extremely high transmission at sufficient resolving power of $E/\Delta E \geq 1200$ to allow the collection of high-quality spectra with comparably low photon flux densities. The optics were manufactured by *InSync, Inc.* (spherical mirror) and *Carl Zeiss Optronics GmbH* (mechanically ruled plane diffraction grating). The spectrometer

Table 3.1: Optical parameters as well as calculated reflectivities and efficiencies for the selected photon energies and diffraction orders. The total detection efficiency is calculated as the product of calculated mirror reflectivity, measured grating efficiency, and detector efficiency taken from the operating manual of the detector [73].

Angles and Distances (as defined in Fig. 3.2)

$$\varphi = 172° \qquad r_1 = 400 \text{ mm}$$
$$\alpha = 87.9° \qquad r_2 = 100 \text{ mm}$$
$$\beta = 84.1° \qquad r_3 = 1{,}000 \text{ mm}$$

Mirror Specifications

Dimensions:	(20×80) mm
Radius of Curvature:	R=8,410 mm

Grating Specifications

Dimensions:	(20×110) mm
Blaze angle:	1.8° for inner (positive) orders
Central groove density:	$a_0 = 600$ lines/mm
VLS parameters:	$a_1 = 1.19634$ lines/mm^2
	$a_2 = 1.27512 \cdot 10^{-3}$ lines/mm^3
	$a_3 = 1.11401 \cdot 10^{-6}$ lines/mm^4
Rule density [lines/mm]:	$n(x) = (a_0 + a_1 x + a_2 x^2 + a_3 x^3), x$ in mm

Detector Specifications

Dimensions:	(27.6×27.6) mm
Pixel dimensions:	(13.5×13.5) μm

Throughput

Acceptance angle: (11.2×18.0) mrad^2

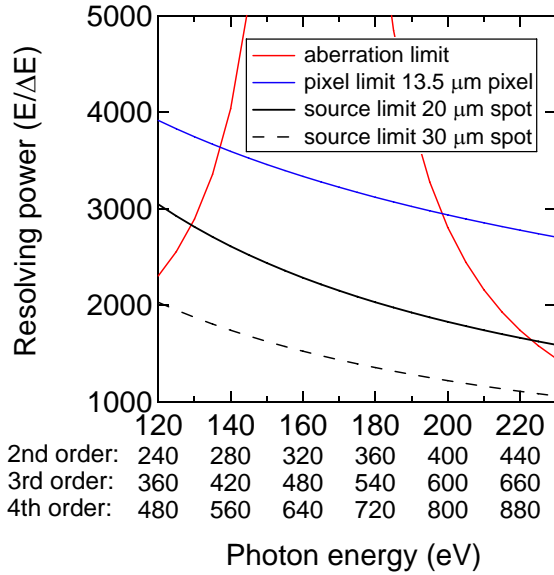| Emission line	S L$_{2,3}$	C K	N K	O K
Emission energy (eV)	150	280	400	525
Diffraction order	+1	+2	+3	+3
Calc. mirror reflectivity	68%	67%	65%	60%
Calc. grating efficiency	25%	22%	19%	19%
Measured grating efficiency	26%	23%	17%	13%
Detector efficiency [73]	30%	40%	50%	60%
Total detection efficiency	5.3%	6.2%	5.2%	4.7%

Figure 3.3: The different limitations of the resolving power as a function of photon energy and diffraction order. For calculating the aberration limit, a fully illuminated mirror (i.e. with open aperture **A**) was assumed.

mechanics was built by the Center for X-ray Optics (CXRO), Lawrence Berkeley National Laboratory. The optics were tested at beamline 6.3.2 and the assembled instrument at beamline 8.0.2 of the Advanced Light Source (ALS).

The optical design

The basic configuration of the spectrometer is shown in Fig. 3.2. It features a spherical mirror **M** and a VLS grating **G** in inner (positive) diffraction order geometry. This combination, albeit for outer order geometry, was originally proposed by Hettrick and Underwood [85–89] and allows the use of the detector **D** in normal incidence geometry, thereby yielding optimal quantum efficiency of the CCD detector. A variable aperture **A** can be used to mask the mirror, which reduces imaging aberrations at the cost of vertical acceptance angle. In practice, this aperture is used solely for alignment purposes, since the imaging aberrations are sufficiently small even with open aperture and do not compromise the overall resolving power, as can also be seen in Figure 3.3. In this figure, the three resolution limits (spot size, aberrations, and detector pixel size) are plotted as a function of photon energy and diffraction order. Only for resolving powers larger than 1200 (for the lower part of the energy window) and 2000 (for the high part), respectively, i.e. for spot sizes smaller than 20 microns, the aberration limit starts to play a role at the edges of the detected energy window. The careful balancing of the three resolution limits lead to the optical design parameters summarized in Table 3.1. A detailed description of how these parameters were optimized is offered in Appendix A and in [92].

As described above, one major goal was to keep the photon flux density low to

minimize or avoid beam-induced effects on radiation-sensitive samples. This can be achieved by maximizing the spot size on the sample and minimizing the excitation flux. To be able to use large spot sizes while still maintaining a high energy resolution even without an entrance slit, a low magnification of the source spot in the energy-dispersive direction on the detector is necessary. By using the inner orders of the diffraction grating and by optimizing the design parameters of the spectrometer, a magnification of one has been achieved. This is equal to the case of the conventional Rowland geometry, but the present VLS design offers a significantly improved throughput for the following reasons: The VLS approach cancels the imaging aberrations sufficiently even for the large solid angle collected by the spherical mirror. Further, the detector can be used in normal incidence geometry, which maximizes its detection efficiency. Finally, the use of optimal diffraction orders (see below) for the different photon energies always keeps the blaze angle of the grating close to ideal, leading to maximal throughput for the whole energy range.

The VLS parameters of the grating were selected such that the spherical aberrations introduced by the light-collecting mirror are largely compensated in the desired photon energy range. For only one specific energy and diffraction order it would be possible to modulate the line density such that the imaging aberrations vanish entirely, leading to a stigmatic image in the dispersive direction. Instead of optimizing the VLS parameters in this way for each energy and order separately, which would require the use of several exchangeable gratings and the translation of the detector, only one grating is employed with a fixed detector. This setup allows for the simultaneous detection of all four core levels and hence photon energy ranges of interest, extending from 150 to 525 eV, in appropriate diffraction orders: the lower energies in 1st order (S $L_{2,3}$ emission), the intermediate energies in 2nd order (C K emission), and the higher energies in 3rd order (N and O K emission). For higher energy resolution at slightly decreased intensity, even the 4th order can be used for O K emission. The simultaneous optimization for different orders allows keeping the imaging aberrations low for the entire energy range with only one grating, yielding an aberration-limited resolving power of well above 2000 for all four energy ranges simultaneously (shown in Fig. 3.3 as discussed above). It also moves the emission lines closer together, which allows studying them simultaneously in one detector image, while still avoiding overlapping spectra.

In order to find the optimum VLS parameters which are the best compromise for all four energies in their respective orders, extensive ray tracing calculations were performed. For this purpose, the imaging aberrations for the relevant energies and orders were expressed in analytical form. This analytical approach is of advantage, since the minimization of the imaging aberrations at all four energies simultaneously can then be done by an optimization algorithm based on Newton's method, which makes use of the analytically determined Jacobian matrix resulting in a very robust

and quickly converging minimization process even in a high-dimensional parameter space. A more detailed discussion of these special ray tracing calculations can be found in Section A.6.

The optimized parameter set included up to four VLS parameters (line density variation up to the quartic term), the detector tilt angle, and the distance between grating and detector. In the process it became apparent that tilting and shifting the detector out of the zero order focal plane as well as including higher VLS orders than the cubic term does not lead to significantly smaller imaging aberrations. Therefore, in the final design three VLS-parameters were optimized (i.e., up to the cubic term) with the detector plane in the zero order focus and normal incidence geometry. The derived parameters are listed in Table 3.1.

The VLS grating has been ruled with the ruling engine GTM6. This engine has an interferometric control, which is used to govern the line density variation of the grating. In contrast to the commonly used mechanical ruling under lubricant protection, a 'dry' ruling technique without any lubrication during the ruling process was applied. In this way, any molecular contamination is avoided, which is of importance for the ruling of gratings for synchrotron radiation.

A diamond tool was used to rule the blaze profiles by plastic deformation in a film of gold which was thermally vapor deposited and optimized for small micro roughness. After the ruling, a final ion beam etching process was applied to transfer the blaze profile completely into the blank material. This ion beam etching step makes use of the difference in the etching rates between gold and silicon, which differ typically by a factor of 3. So, the master ruling is starting with a larger blaze angle and ends with the specified profile form. The micro roughness is reduced by nearly the same factor. Micro roughness values below 0.6 nm r.m.s. have been achieved with this technique. Consequently, gratings produced by the ion beam etching technique have an improved stray light compared to those manufactured by the classical technique.

Performance

Efficiency

Due to the entrance slit-less design, all photons within a solid angle of (11.2×18.0) mrad^2 emanating from the source enter the spectrometer. While the acceptance angle in dispersive direction (11.2 mrad) is limited by the size of the focusing optics, the non-dispersive direction (18.0 mrad) is merely limited by the size of the detector, since the focusing properties of mirror and grating are negligible in this direction. The included angles of mirror (φ) and grating ($\alpha + \beta$) were chosen to be 172°. With
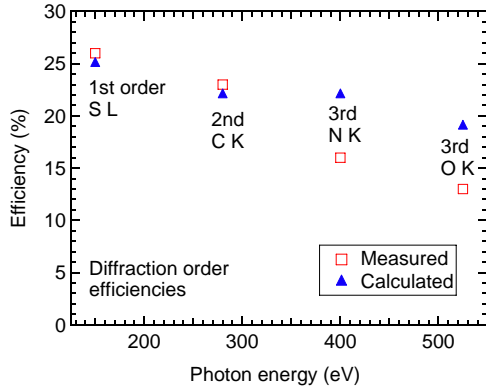
Figure 3.4: Comparison of the measured (red squares) and calculated (blue triangles) grating efficiencies for the four photon energies of interest in their respective diffraction orders. The efficiencies were measured at beamline 6.3.2. For the calculations a micro roughness of 10 Å was assumed.

these angles and a nickel coating the reflectivity is above 50% even at the oxygen K edge for each optical element. In order to maximize the grating efficiency, a blaze angle of 1.8° was chosen. Due to the special selection of diffraction orders described in Section 3.1, the blazing concentrates the reflected intensity for all four interesting energies simultaneously, leading to theoretical grating efficiencies of 18–25% in the whole energy range at an assumed micro-roughness of 10 Å (see Table 3.1). It is worth noting that the used diffraction orders are the most intense for the selected energies, not only in theory, but also confirmed by measurements of the grating efficiency.

For example, at the nitrogen K edge, the 3rd order is more intense than the 0th, 1st, 2nd or 4th (and so on) order. Figure 3.4 compares the theoretical efficiencies of the selected orders with efficiency measurements taken at beamline 6.3.2 of the ALS. The numbers are also given in Table 3.1. The grating performs slightly better than the theoretical values at the sulfur L and carbon K edge (Fig. 3.4). This is due to the fact that the actual blaze angle of the grating is slightly larger (steeper) than the design value of 1.8°. This slight mismatch, together with other unavoidable imperfections of the grating (e.g., roughness and surface oxidation of the coating), consequently lead to a reduced measured efficiency (70%) compared to the theoretical value at the nitrogen and oxygen K edge in 3rd order.

The detector is another crucial component for high spectrometer efficiency. While many earlier spectrometer designs rely on CsI-coated multi channel plate detectors (e.g. [74–78]), a back-illuminated charge coupled device (CCD) detector from Andor Technology PLC was used. Comparable detectors are mounted in the instruments described in [81, 83, 84, 90, 91, 93]. This choice together with the optimized detector geometry (normal incidence compared to grazing incidence for Rowland circle spectrometers) increases the overall spectrometer efficiency further. A drawback is the high detector sensitivity to visible light, which requires keeping the experiment dark during data acquisition. A set of baffles between grating and detector traps the visible light emitted from fluorescing samples.
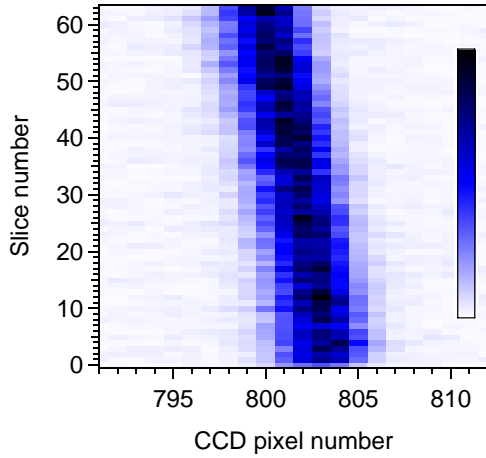
Figure 3.5: The narrow Rayleigh line as it appears on the rotated CCD detector, allowing the use of the super-resolution technique. The image was read out with a resolution of 64 slices in the vertical direction and expanded by a factor of 100 in the horizontal direction.

The overall efficiency of the VLS spectrometer was compared with the one permanently installed at beamline 8.0.1 of the ALS [76]. After adjusting its entrance slit to a comparable resolving power, the comparison revealed an approximate gain of two orders of magnitude for all four edges. As discussed in Section 2.3.1, this significant improvement allows the collection of more than 100 individual spectra within 10 to 40 minutes. This multitude of RIXS spectra can then be compiled in a 2-dimensional RIXS map.

Resolving power

The selection of different diffraction orders for the different energies keeps the resolving power above 1000 over the whole spectral range despite the use of only one grating. Fig. 3.3 demonstrates how the resolving power is limited (by source size, aberration, or pixel size) as a function of photon energy and selected order. For the energies of interest for our application, we find a resolving power of 1200 or higher at a source spot size as large as (30×3000) μm^2. In this case (and as shown in Fig. 3.3), the resolving power is exclusively limited by the source size.

Since the pixel size of 13.5 μm is one third of the full width at half maximum (FWHM) of the narrowest features (i.e. features in the source size limit), the sharpest resolvable peaks consist of only 6 pixels in dispersive direction, which leads to artifacts typical for undersampled data. In order to get rid of such effects, a software algorithm was developed, which increases the number of effective pixels by using a 'super-resolution' reconstruction technique, the basic idea of which is published in [93].

It will be described in the following by applying it step-by-step to an extremely narrow Rayleigh line. During read out of the CCD, in non-dispersive direction, 32 CCD pixels are merged in the read out register, thereby reducing the native CCD
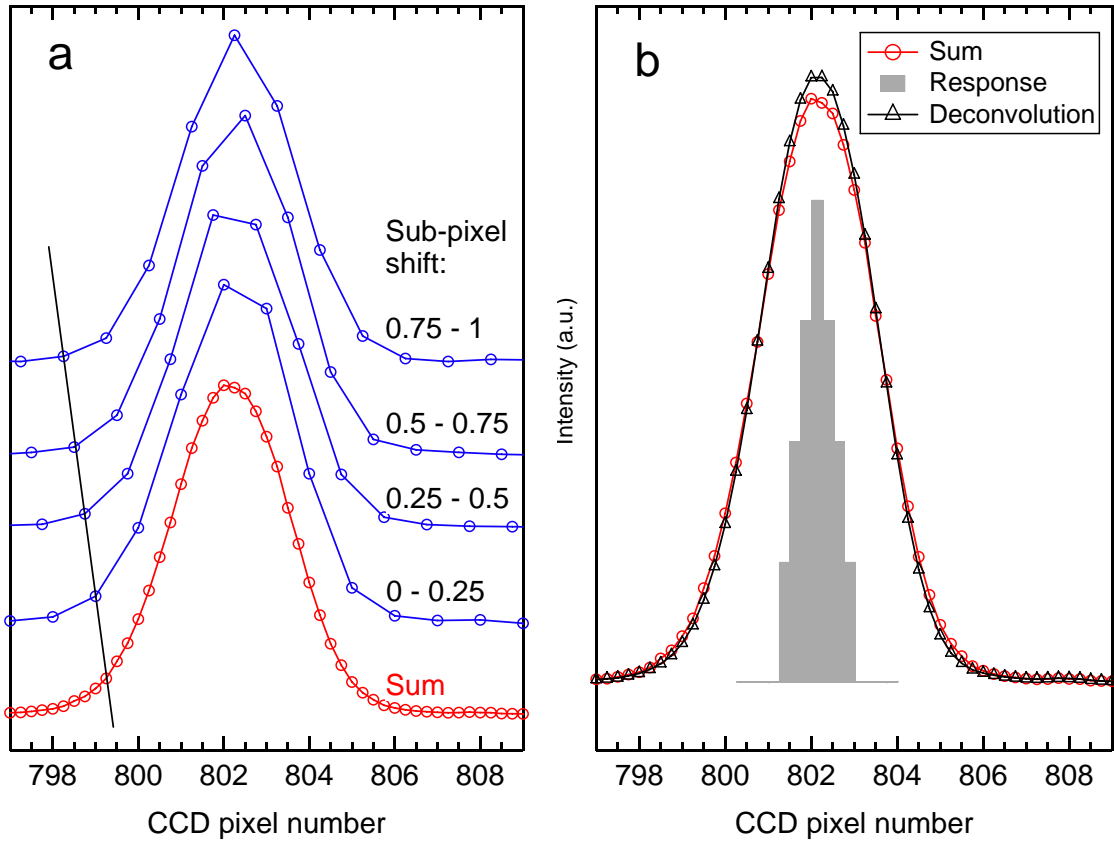
Figure 3.6: a) The four top spectra (blue) show the sums of four groups of slices selected and shifted by their sub-pixel shifts. The bottom spectrum (red) is the sum of the four spectra above. b) The red line with circles is a copy of the lowest spectrum in a), the gray bars represent the response function of the super-resolution technique to a δ-function, and the black line with triangles shows the spectrum deconvolved by the response function using 3 van Cittert iterations.

resolution of 2048 to 64 slices. This accelerates the read out process and decreases the read out noise considerably. For the 'super-resolution' approach, the CCD is intentionally rotated by approx. 0.1° relative to the emission lines. The resulting image of an elastic peak (Rayleigh line) is shown in Fig. 3.5, expanded in the horizontal direction by a factor of 100. Each slice contains the same spectrum, but with a sub-pixel shift relative to its adjacent slices. This additional spatial information can be used to reconstruct a super-resolution spectrum. In this example, the number of effective pixels will be multiplied by 4. In order to achieve this, we first separate the total shift of each slice with respect to the center slice as calculated from the CCD rotation angle into a whole and a fractional pixel shift. The whole pixel shift is eliminated in each single-slice spectrum by appropriate counter-shifts (e.g. for a single-slice spectrum with a calculated pixel shift of 2.3 pixels, the intensity stored in pixel number i is shifted to pixel number $i - 2$, leaving a residual sub-pixel shift of 0.3). In the next step, the resulting 64 sub-spectra are sorted by their sub-pixel shift into 4 bins. Bin 1 contains all spectra having a shift between 0 and 0.25 pixels, bin 2 from 0.25 to 0.5 pixels, and so forth. The sub-spectra in each bin are added up and divided by the number of contributing spectra, resulting in the 4 topmost spectra in Fig. 3.6a, which have been shifted taking the sub-pixel shifts into account, as indicated by the black line at the left. These spectra are added up to the super-resolution spectrum (bottom spectrum in Fig. 3.6a).

Applying this super-resolution procedure to a fictional δ-peak leads to the triangular response function shown as gray bars in Fig. 3.6b. The FWHM of this narrowest possible peak is one CCD pixel (or four super-resolution pixels). This means that in order to resolve features which are narrower than one detector pixel, we would have to deconvolve the super-resolution spectrum by this response function. A true deconvolution is impossible (and not necessary: the source size does not allow such extremely narrow features), since the Fourier transform of the response function contains zeros. Nevertheless, the spectra can be narrowed to some extent by applying the iterative van Cittert deconvolution method [94, 95]. Fig. 3.6b shows the result of 3 van Cittert iterations (black line and triangles) together with the original super-resolution spectrum (red line and circles). Note that while the described super-resolution technique is very useful in order to avoid undersampling artifacts, deconvolution is not obligatory in our case, since the resolution is always limited by the source size (see Fig. 3.3) and not by the pixel size, as discussed above. In consequence, all spectra and RIXS maps shown in Chapter 4 were treated with the described super-resolution algorithm, multiplying the effective number of detector pixels by 4, but no deconvolution was applied.

Summary

A novel soft x-ray emission spectrometer was developed, consisting of a spherical mirror, a blazed plane VLS grating, and a back-illuminated CCD detector in normal incidence geometry. It covers the photon energy range from 130 to 650 eV at a resolving power of 1200 with only one grating by making use of suitable diffraction orders. This approach also optimizes the detection efficiency. The optical design (including the variable line spacing parameters) was optimized by a novel analytic ray tracing algorithm (see also Section A.6). In order to increase the spatial detector resolution, a super-resolution reconstruction technique was developed. Due to the two orders of magnitude higher detection efficiency compared to existing spectrometers, it is possible to record a complete 2-dimensional RIXS map in less than one hour. Examples of RIXS maps are given in Sections 4.1 and 4.3. For an even more detailed discussion of the methods used to develop the optical design of this spectrometer, refer to [92]. Appendix B contains a detailed instruction describing the alignment and calibration of the instrument.

3.2 Flow-through liquid cell

This Section describes the design of a temperature-controlled flow-through liquid cell dedicated to the study of liquids with soft x-rays. It was published in a similar form in [96].

While the investigation of the electronic structure of gaseous and solid samples with soft x-ray techniques using synchrotron radiation is well established, their application to the vacuum-incompatible liquid phase poses many technical challenges. This is one of the reasons why even for liquids of fundamental importance (e.g. water), the electronic structure is still not completely understood. Therefore, liquids currently constitute a very popular and controversial field of research, especially in the case of water [97–103], as also discussed in Section 4.3.

An established technique for investigating the unoccupied electronic states of liquids is x-ray Raman spectroscopy (XRS) [104], which is a hard x-ray photon-in photon-out technique with significantly higher penetration depth than soft x-ray techniques (150 μm as compared to 300 nm [71]), making it easily possible to investigate liquids under ambient conditions. A comparison of all XAS and XRS techniques previously applied to water can be found in [71]. The obvious disadvantage of the XRS technique is its low energy resolution of about 1 eV [71, 104], but, in contrast to fluorescence yield XAS, it does not suffer from self-absorption saturation effects [71], which were discussed in Section 2.3.2.

Another way to obtain information on the electronic structure of liquids is to use electron- or ion-yield x-ray absorption (XAS) or photoelectron spectroscopy (PES) on a liquid micro jet injected directly into the vacuum [99–101, 105–115]. Besides the technical difficulties to maintain the analysis chamber and the beamline at a low enough pressure, the liquid in such a jet is far from thermodynamic equilibrium, which complicates the interpretation of the data, especially in the case of solutions. In addition, a considerable contribution of signal from vapor surrounding the jet compromises the results.

A different approach is followed in this work — the liquid is kept at close-to-ambient conditions and separated from the ultra-high vacuum (UHV) of the analysis chamber by a thin membrane, which allows the application of soft x-ray photon-in photon-out techniques for the characterization of the liquid. While with this method, XAS experiments on liquids [116–118] are comparably simple, the application of XES [119–123] is much more difficult, since the higher excitation intensity needed for this technique causes several problems discussed in Sections 4.2, 4.4, and 4.3. The reason is the extremely small fluorescence yield for elements with low atomic numbers (compare Section 2.1) forming most of the liquids, combined with the extremely low efficiency of conventional XES spectrometers (see Section 3.1).

The simplest conceivable liquid cell is a static cell, in which a definite amount of liquid is encapsulated by a membrane. All currently available publications of XES on liquids used such static cells [119–122], except for those reporting results obtained with the liquid cell described below [62, 96, 124] and one recent publication [123]. For static cells, every change of liquid requires the transfer of the cell out of the vacuum chamber including venting. In addition, static cells are only applicable when temperature control is not important, and when dealing with small molecules, e.g., water. The reason is that the high x-ray intensity needed for XES deposits a power of up to 0.1 Watts in an extremely small volume of approx. 100 picoliters. This leads to a strong local temperature rise close to the membrane and often to decomposition of the liquid. The latter is not so much of a problem for small molecules since the dissociation products are gaseous, causing gas bubbles. These do not significantly contribute to the spectra, but of course lead to technical problems like pressure rise and displacement of liquid. For larger molecules (i.e. organic solutions), the soluble dissociation products accumulate in the liquid itself, while the insoluble parts form a film on the backside of the membrane. Even thin layers (< 50 nm) of the latter easily dominate the resulting spectra.

Based on the experience with static cells, a flow cell was planned [125] and constructed. The important difference of this design is that the probing volume is connected to inlet and outlet tubes via which the liquid can be pumped through the cell during the measurement. Therefore, the exposed liquid is steadily replaced with fresh tempered liquid, offering a reliable temperature control, much lower
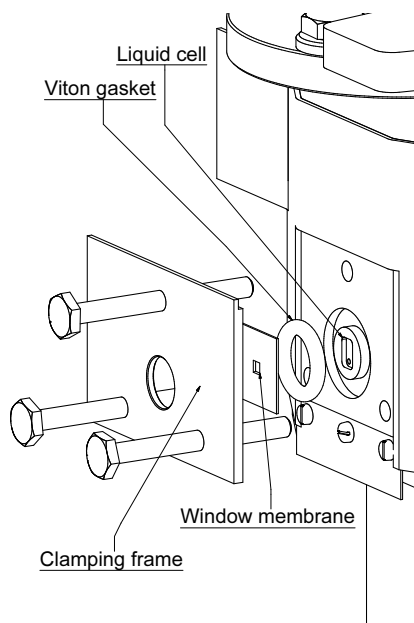
Liquid cell

Viton gasket

Window membrane

Clamping frame

Figure 3.7: Close view of the liquid cell sealed with a Viton o-ring gasket. The quick access from the front allows an easy membrane exchange and cell maintenance.

beam damage effects and quick and easy exchange of liquids. It also reliably avoids gas bubble formation up to the boiling temperature of the liquid. Furthermore, the flow concept allows to *in-situ* monitor chemical reactions taking place in the liquid. This could be for example the growth of wet-chemically produced nanoparticles or the electrochemical reactions taking place at the interface of the electrolyte and the electrodes of a fuel cell, just to name a few modern applications.

Mechanical layout

The liquid cell assembly is mounted on a standard sample manipulator (*Omniax, VG-Scienta*) with XYZ-translation and one rotational axis, which can be easily attached to existing vacuum systems. A small load-lock between vacuum system and manipulator allows the replacement of the window membrane, and cleaning and maintenance of the cell without venting the measurement chamber. In order to provide quick access to the cell for such routine procedures, we use an O-ring-sealed fixture for the window membrane, consisting of a clamping frame and three screws (Fig. 3.7). The gasket works very reliably, maintaining a pressure of typically $1 \cdot 10^{-8}$ mbar in the experimental chamber without prior baking.

A sketch of the liquid cell is shown in Fig. 3.8. The actual cell is 3 mm high, 2 mm wide, and 0.5 mm thick, resulting in a volume of 3 microliters (μl). In order to ensure that in case of a membrane leak, only a small volume of the liquid is released into the vacuum, it is equipped with interlocked fast liquid valves. The channels to the fast closing liquid valves (Fig. 3.9) contain another 12 μl, i.e., in case of
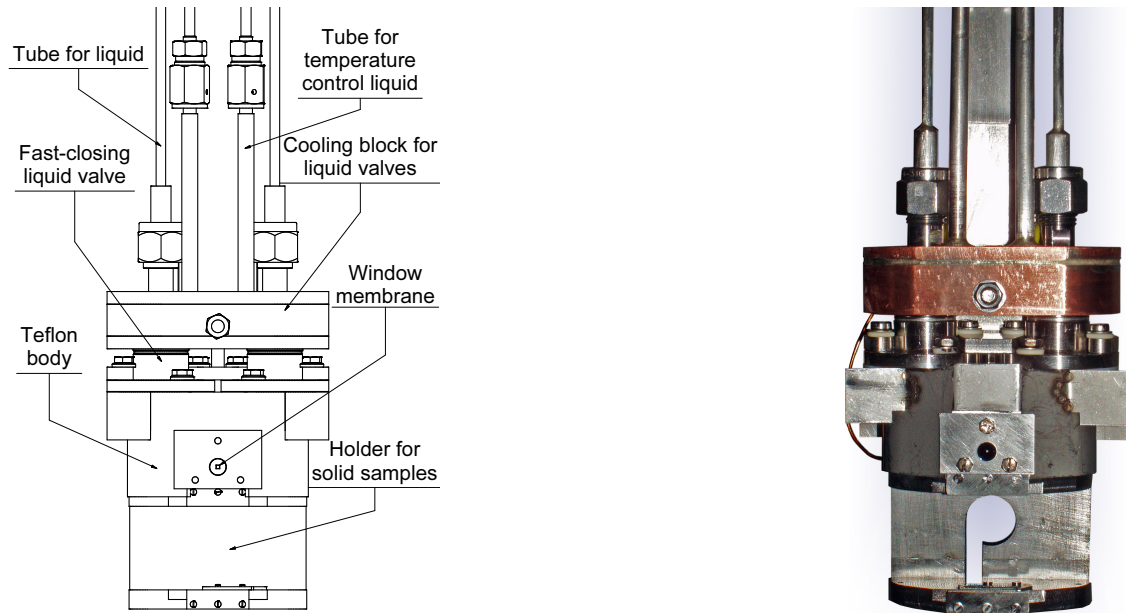
40

Figure 3.8: Sketch (left) and photograph (right) of the liquid cell identifying the important components. The solenoids of the valves require cooling and are hence surrounded by a cooling block. Above the visible region, the two pairs of tubes merge to two double-walled tubes with the liquid under study in the inner and the temperature controlled liquid in the outer tubes in order to get the liquid to the desired temperature.

a membrane burst, at most 15 μl of the liquid under study are released into the vacuum. Since the valves, which are triggered by a fast pressure sensor, close within 1.5 ms after membrane failure, the amount of liquid passing the valves during this time is negligible. The short closing time is made possible by custom-designed trigger electronics, which dissipate the magnetic field of the solenoids quickly by allowing induced voltage spikes of up to 1000 V.

In the case of a window rupture, typically only a small fraction of the 15 μl is released instantaneously into the vacuum, although the membranes always break abruptly. The reason is that most of the liquid freezes upon exposure to UHV; the ice then blocks the channels to the valves and sublimates only slowly. The risk of releasing liquid into the vacuum has to be considered for the design of the vacuum system: differential pumping and a fast interlock system of the measurement chamber and the beamline are essential.

The total volume of the liquid cell system, including the tubes above the valves, is approx. 1.6 ml. This means that for changing the liquid under study, the cell should be purged with 2 ml or more, so the required minimum amount of liquid is about 5 ml. A peristaltic pump with adjustable pumping speed is used to suck the liquid under study from the reservoir through the system, thereby always keeping
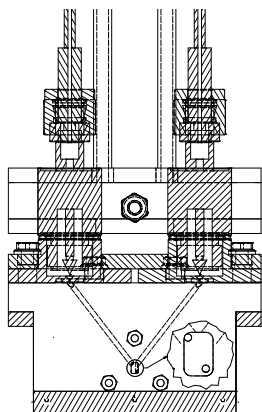
Figure 3.9: This cut through the cell reveals the interior channels in the Teflon body. A magnified image of the liquid cell section is shown in the lower right corner. The position of the in- and outlet holes are located in opposite corners to give maximum flow velocity at the probed volume in the center of the cell.

the cell slightly below ambient pressure. For water, for example, we used a flow rate of approx. 45 μl per second, thus replacing the volume of the cell 15 times per second. Depending on the availability of the liquid under study and the expected beam damage, the liquid sucked through the cell can either be reused by feeding it back into the reservoir or be disposed. Since the only parts wetted by the liquid under study are the Tygon tubing of the peristaltic pump, the stainless steel tubes in the manipulator, the stainless steel fast valves, and the Teflon body of the liquid cell itself, contaminations of the liquid can be avoided, as long as this does not corrode stainless steel.

The membrane

The membrane is the crucial part of the cell. It has to be extremely thin, free of impurities, and at the same time rigid enough to endure atmospheric pressure even under synchrotron irradiation with 10^{16} photons/sec/mm^2. The thickness of the membrane is limited by the attenuation length of soft x-rays, which lies between 40 and 300 nm in suitable materials depending on the photon energy and the composition of the membrane. Silicon nitride (Si$_3$N$_4$) membranes (*Silson Ltd.*) with a thickness of 100 nm and silicon carbide (SiC) membranes (*NTT Advanced Technologies*) with a thickness of 150 nm were found to be suitable. The lateral dimensions of both membranes are 1x1 mm^2. When used complementarily, these two membrane materials allow the application of photon energies in the whole soft x-ray range between 10 and 1100 eV except for the range at and slightly above the silicon L edge (100–200 eV). They suffer from aging under irradiation as discussed in Section 4.3, so depending on the photon flux and the properties of the liquid, they need to be replaced after a few hours to a few days of measurements.

Temperature control

For constant experimental conditions and the possibility of temperature dependent measurements, a well-defined temperature inside the probed volume of the liquid is desired. A thermocouple right at the back plate of the cell volume only 0.5 mm away from the window membrane gives a reliable temperature reading during the measurement. To minimize local heating by the synchrotron beam within the probed spot right behind the membrane, a high flow rate is necessary. The in- and outlet bore holes (inset in Fig. 3.9) are located in opposite corners of the cell to ensure a high flow velocity through the probed volume in the center of the cell.

The temperature control liquid is a 1:1 ethylene glycol-water mixture. This mixture can be kept at a certain temperature in a range from -15 °C to 200 °C using a thermostat equipped with an internal pump. The liquid under study is brought to the desired temperature while it descends through the tubing above the fast valves. It is double-walled in that section (not shown in the figures), with the liquid under study inside the inner tube and the temperature control liquid in the outer tube. Since the solenoid of each fast valve produces 0.3 W of heat in the open position, the temperature control liquid is also pumped through a cooling block surrounding the solenoids. The Teflon block containing the liquid cell is temperature-controlled only by the continuous flow of the liquid under study, making the temperature response inside the cell slow and limiting the usable temperature range.

3.3 The next generation liquid cell

The main disadvantages of the present design are a) the slow temperature response, b) the limited temperature range due to the indirect temperature control of the Teflon block of the cell solely by the flow of the liquid under study, and c) the large amount of liquid necessary due to the relatively long tubing. Recently, these drawbacks were overcome by abandoning the versatile bolt-on approach in a new liquid cell design. The total internal volume of this novel cell is significantly lower: only 10 μl of liquid are released into the vacuum in the case of a membrane break, and the total liquid volume in the flow circuit (excluding the reservoir) can be as low as 200 μl, requiring total amounts of liquid of about 1 ml (including the reservoir). First measurements with this new cell have demonstrated the superior control of both flow and temperature. It is also more reliable, since many crucial components like the fast closing valves and the tubing, which were exposed to UHV in the above-described design, are now located outside, requiring a custom-designed vacuum chamber with the liquid cell incorporated in its backside, as illustrated on the right side of Fig. 3.10. The cell is shut off within less than one second by
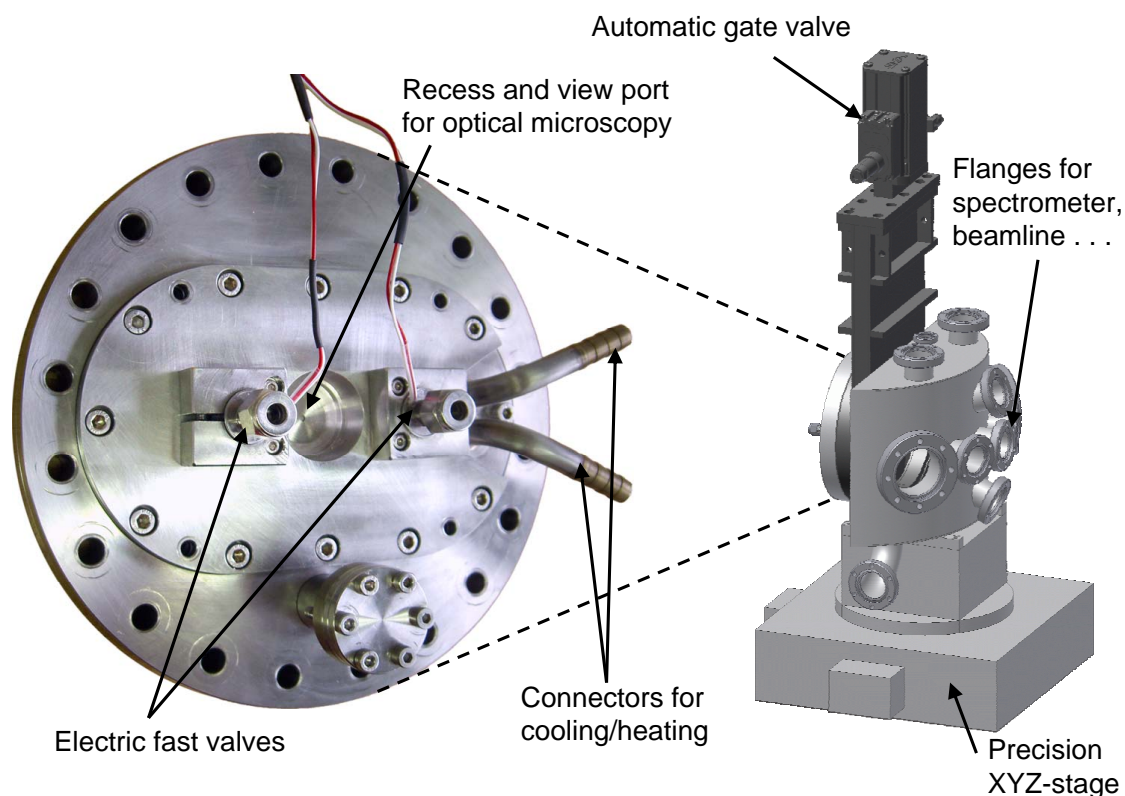
Figure 3.10: The next-generation liquid cell is incorporated in the back flange (left side) of a micro-positioned analysis chamber (right side). The recess in the back of the flange fits a microscope objective and allows viewing the cell interior through the backside made of glass. The cell can be isolated from the chamber in a split-second by an automatic gate valve.

an automatic gate valve in the case of a membrane failure or for maintenance and membrane change. Another advantage of this design is the possibility to monitor the cell content even during x-ray spectroscopic measurements by optical microscopy through the backside of the cell, which is made of glass. Due to the absence of a sample manipulator, the whole vacuum chamber needs to be adjustable with micron precision, which was achieved by an external XYZ-stage. The left of Fig. 3.10 gives a close-up view of the liquid cell back flange.

It is of great advantage to have both liquid cells available. While the new one is part of a dedicated endstation which requires a beamline for 'roll-up' experiments, the above-described cell based on a standard sample manipulator is a 'bolt-on' solution compatible with most standard analysis chambers.

RIXS OF ORGANIC MOLECULES AND LIQUIDS

In this Chapter, the introduced spectroscopic methods are applied to study organic and biologically relevant molecules, the latter in their natural environment — liquid water. In all of these studies, the unique properties of the novel equipment described in the previous Chapter and the RIXS technique are exploited.

In the first Section, the high transmission of the spectrometer is used to apply the novel RIXS map approach to C_{60} fullerenes. Afterwards, the symmetry- and site-specificity of the RIXS method is demonstrated for an ordered multilayer of PTCDA molecules. Third, the novel spectrometer was used in combination with the liquid cell to study the electronic structure of water with the RIXS map approach. In order to draw meaningful conclusions on the properties of liquid water, the experiments were extended to deuterium oxide (heavy water) and aqueous solutions of sodium hydroxide and sodium deuteroxide. The last Section of this Chapter demonstrates the accessibility of the nitrogen K edge of amino acids in aqueous solutions at different pH-values by using silicon carbide membranes instead of the standard material silicon nitride.

4.1 RIXS map of C_{60}

C_{60} molecules are used in organic electronics as strong electron acceptors [126] and have some potential medical applications [127]. They are the only organic molecules studied in this work which are not subject to beam damage, due to their strong internal C–C bonds. Moreover, in the condensed state, the electronic structure is still dominated by that of the single molecule, since intermolecular interactions are rather weak, leading to very shallow bands with small dispersion. These properties together with its high symmetry make the 'Buckminsterfullerene'
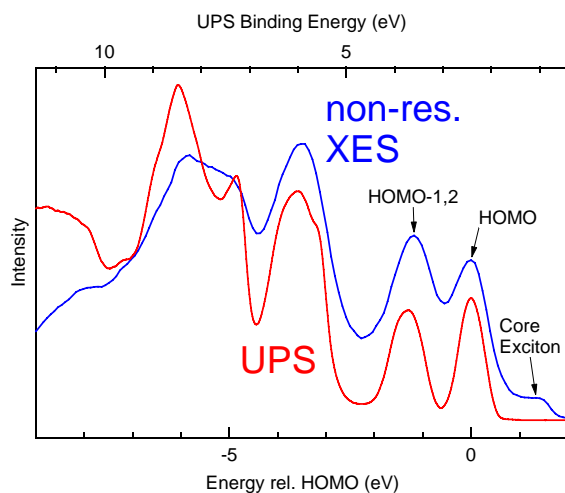
Figure 4.1: Comparison of a non-resonant XES spectrum with UPS data reproduced from [131]. Spectral XES features are labeled according to the discussion in the text.

an ideal candidate for demonstrating the properties of the RIXS technique and for introducing the application of the RIXS map approach to molecules. This novel technique described in Section 2.3.1 is made possible by the unprecedentedly high detection efficiency of the x-ray spectrometer introduced in Section 3.1.

Since its discovery [128], the electronic structure of C_{60} has been investigated in great detail by XAS and PES studies (e.g. [63, 69, 129–133]). There are two published RIXS studies of C_{60} [63, 134]. In the former, strong variations of the relative emission intensities as a function of excitation energy have been found and explained by symmetry selection rules: Depending on the symmetry of the excited unoccupied state, the individual emission features are suppressed or enhanced.

In the present study, commercially available C_{60} in powder form pressed in indium foil was investigated. In order to gain an overview over the occupied electronic structure, we first compare a non-resonant XES spectrum with ultraviolet photoemission spectroscopy (UPS) data reproduced from [131] in Fig. 4.1. Since both techniques have the same final state, the energy positions of the spectral features of XES and UPS coincide well, according to the final state rule [28–30] (except for the constant offset of the core hole binding energy). By plotting the energy positions of the occupied states relative to the position of the highest occupied molecular orbital (HOMO), an unambiguous assignment of the HOMO and the peak formed by the HOMO-1 and HOMO-2 is possible. The other XES emission features below the HOMO-1,2 energy are groups of many contributing molecular orbitals. The major difference of XES and UPS are the transition matrix elements (XES: transition to a core hole, UPS: transition to an unbound state), leading to different relative intensities. A qualitative difference is the existence of an additional state in x-ray emission at a binding energy of about 1 eV. Its absence in photoemission indicates, that this feature is connected to the core hole only present in XES. This
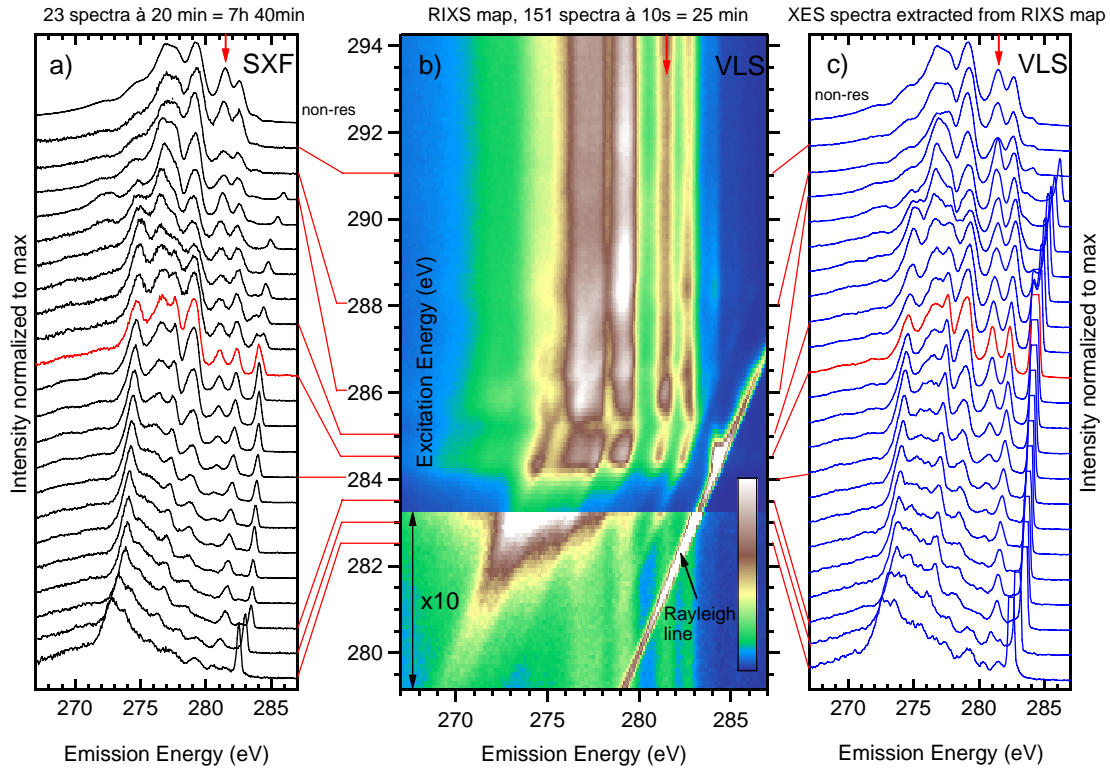
Figure 4.2: a) RIXS series (23 spectra) of C_{60} powder with a data acquisition time of 20 minutes per spectrum. The HOMO-1 is indicated by a red arrow on the top. The red spectrum was excited at the first resonance (core exciton at the LUMO). Red lines indicate the excitation energy at the y-axis of b). b) a RIXS map (151 spectra) taken with 10 s per spectrum. The section excited below 283.25 eV is multiplied ×10 for enhanced visibility c) 23 spectra extracted from b) at the excitation energies of a). Red lines indicate the excitation energy at the y-axis of b).

interpretation is corroborated by the fact, that Brühwiler *et al.* [130] have found strong core hole excitonic effects in their resonant photoemission study of C_{60}.

A RIXS study similar to that in [63] is shown in Fig. 4.2a for C_{60} in powder form. It was taken with the Rowland circle spectrometer of the SXF endstation (ALS beamline 8.0.1), in the following simply called SXF. Each spectrum was acquired for 20 minutes, resulting in a total acquisition time of 7 hours and 40 minutes for the 23 spectra shown. By comparing this RIXS series with the data published in [63], it becomes obvious, that the data taken by the SXF endstation is clearly superior to the previously published RIXS data [63] in terms of both resolution and signal-to-noise ratio. In Fig. 4.2b, the same sample was studied with the variable line space (VLS) spectrometer described in 3.1. Since its superior detection efficiency requires only 10 s per spectrum, it was possible to record 151 spectra within a total

acquisition time of 25 minutes. With such a dense multitude of RIXS spectra, the emission intensity can be plotted in a color-coded 2-dimensional map as a function of the emission energy (x) and excitation energy (y) instead of individual spectra. A color scale is given in the lower right corner of the map. The intensities of the spectral series (a and c) were normalized to the maximum, while those in the RIXS map (b) were normalized to the excitation intensity and multiplied by 10 below an excitation energy of 283.25 eV for enhanced visibility. In order to demonstrate that the quality of the VLS RIXS spectra is comparable to that of the spectra from the SXF spectrometer despite a 120 times shorter acquisition time, 23 RIXS spectra with the same excitation energies as in the SXF study were extracted from this map and displayed in Fig. 4.2c. The only significant difference between the SXF and VLS spectra is the relative intensity of the Rayleigh line. This is solely due to the detection geometry: the optical axis of the SXF spectrometer was mounted parallel to the electric field vector of the linearly polarized synchrotron radiation, which strongly suppresses the Rayleigh line, while the VLS spectrometer was aligned perpendicular to the polarization, yielding a very intense Rayleigh line, which is truncated in Fig. 4.2c. The excitation energies of some RIXS spectra are indicated by red lines drawn to the respective positions at the y-axis of the RIXS map for both spectral series.

The strong variations of the RIXS spectra with the excitation energy reported in [63] are also present in Figures 4.2a, b, and c. While some resonant effects are hard to see in the spectral series due to the confusing manifold of sharp features, the underlying dependencies become obvious in the RIXS map. An example is the region excited below 284 eV, which is partly enhanced by a factor of 10 in the RIXS map for improved visibility. With decreasing excitation energy, the spectra in Fig. 4.2a and c become flatter and featureless, eventually leaving only a wedge-shaped structure. However, in the 2D-map, the reason becomes obvious: all remaining spectral features except for the HOMO-1,2 peak marked by a red arrow (top of Figs. 4.2a, b, and c), get split into two components: one shows a Raman shift parallel to the elastic Rayleigh line, while the other stays at the emission energies observed for non-resonant excitation (topmost spectra). The latter component is an experimental artifact caused by higher undulator harmonics passing the beamline monochromator in higher diffraction orders, and leading to a very weak intensity of non-resonant excitation.

The fact that the HOMO-1,2 peak (red arrows) is suppressed in the Raman-shifting component is explained in [63] by the parity selection rule: as discussed below, the absorption feature at an excitation energy of 284.5 eV stems from excitation into the core-excitonic state of the lowest unoccupied orbital (LUMO), which is a state with *ungerade* parity. In that case, according to the parity selection rule (Section 2.2) for centro-symmetric molecules, emission is only allowed from *ungerade* states. However, the HOMO-1 and -2 are *gerade* states as identified by *ab initio* calculations
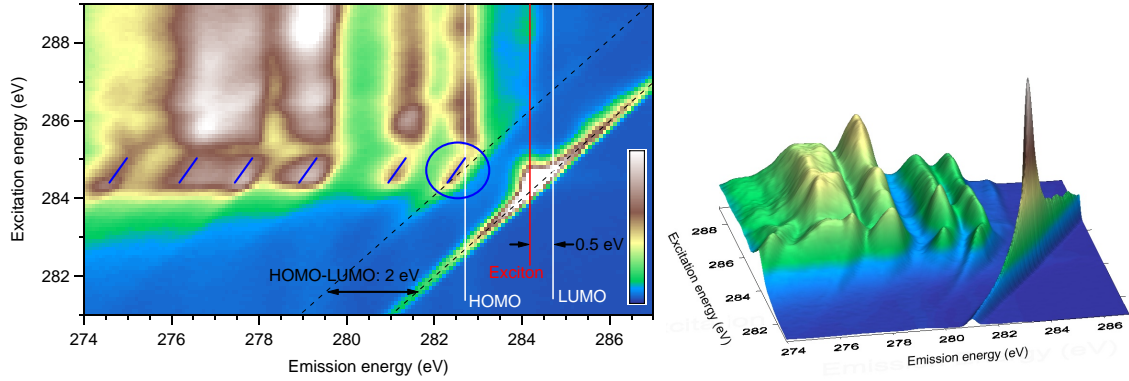
Figure 4.3: 2- and 3-dimensional detail view of the RIXS map close to the core exciton resonance. Left graph: at the HOMO (blue circle), the black dashed line marks the Raman loss features, the white lines indicate the positions of the non-resonant HOMO and LUMO emission energies, and the blue lines represent the behavior of the emission features at the exciton resonance. The red line marks the core exciton emission energy.

in [63]. Therefore, it is surprising, why this feature is *only* suppressed in the Raman regime below the edge, while it shows a strong intensity at the LUMO excitation energy of 284.5 eV (the corresponding emission spectrum is shown in red in both spectral series). This is due to the fact that the electronic excitation also stimulates molecular vibrations which cause the molecule to become asymmetric during the core hole lifetime, thereby breaking the inversion symmetry. For detuned excitation below 284.0 eV, the core hole lifetime is shortened as discussed in Section 2.2.5, leading to a more symmetric final state and to the parity conservation demanded by the parity selection rule.

Figure 4.3 offers a 2- and 3-dimensional view of the closer region around the sharp resonance of the Rayleigh peak, which occurs when the excitation energy is passing the emission feature denoted as core exciton in Fig. 4.1. The strong resonant enhancement of the Rayleigh line is characteristic of an exciton, since its participator decay is very likely. This resonance starts at an excitation energy of 284.2 eV, at which a resonant enhancement of all emission features is observed as a consequence of the possibility to excite into real accessible states. At that energy, the Raman regime with constant energy loss ends, and all emission features leave the slope of the Rayleigh peak indicated in the left graph by the two parallel dashed lines at the position of the Rayleigh line and the HOMO. The emission energy difference of these dashed lines is 2.0 ± 0.1 eV, which is the energy a photon loses when exciting an electron from the HOMO to the LUMO. This energy loss is equal to the (ground state) HOMO–LUMO distance reduced by the binding energy of the valence exciton in C_{60}. Two white lines represent the positions of the non-resonant emission energy of the HOMO (left line) and the position of the LUMO valence exciton as determined by the Raman loss given above. The position of the core exciton res-
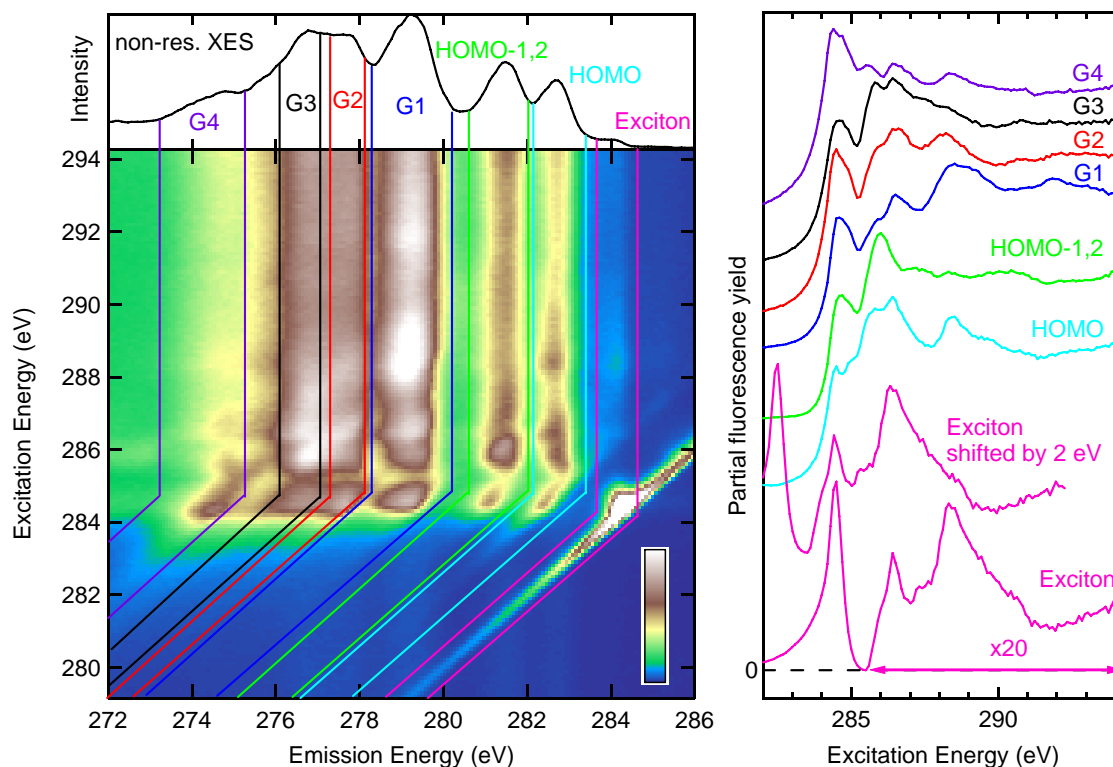
Figure 4.4: The map intensities (left) of selected features (defined in the left top non-resonant XES spectrum) were integrated in the areas defined by colored lines and plotted as decay channel-selective partial fluorescence yield XAS spectra (right). The lowest spectrum representing the occupancy of the core-excitonic state below the LUMO was amplified by a factor of 20 above 285.6 eV for enhanced visibility.

onance is indicated by a red vertical line and the distance of 0.5 eV between this line and the white LUMO line is the difference of the binding energy of the core exciton and the valence exciton.

Instead of occurring at a constant emission energy above 284.2 eV, the emission features still shift with increasing excitation energy, but with a reduced slope, as indicated by the blue lines. This can be seen best at the HOMO (interesting region surrounded by a blue circle), since it is the sharpest emission feature. This behavior can be explained by the fact, that for a core-excitonic intermediate state and a valence-excitonic final state, the emitted photon has to make up for the energy difference ΔE between the core exciton and valence exciton binding energies. This energy difference is lost compared to the non-resonant HOMO emission energy (indicated by the white line), leading to the observed deviation of the blue line from the white line in the blue circle. The highest observed ΔE of about 0.4 eV occurs at an excitation energy of 284.4 eV. This is close to the previously determined energy difference of 0.5 eV between the core-excitonic state and the valence exciton.

It is interesting, that the core exciton below the LUMO is observed as an emission feature even high above the resonance, meaning that it is partly populated even by non-resonant excitation. Since the RIXS map allows the extraction of partial fluorescence yield (PFY) XAS spectra of individual emission features, the occupancy of the core-excitonic state can be displayed as a function of the excitation energy. This is plotted as the bottom curve of the right panel in Figure 4.4 together with the PFY signal of other selected emission features, namely HOMO, HOMO-1,2 peak, and features G1 to G4. These are defined in the non-resonant XES spectrum on the top of the map in the left of Figure 4.4, which shows the detection windows of the individual PFY features. While all detection windows have fixed emission energies for excitation above the edge, they shift in a Raman-like manner together with the emission features below an excitation energy of 284.6 eV with the exception of the exciton window, which shifts below 284.1 eV in order to keep the elastic peak in the detection window.

On the right side, the resulting decay channel-selective PFY spectra are shown. In order to make the low occupancy of the core exciton above the resonance visible, the respective (lowest pink) spectrum was boosted by a factor of 20 above 285.6 eV. After the first resonance at 284.4 eV, the occupancy of the core exciton drops down to zero at 285.5 eV, as visualized by the horizontal black dotted zero line. The second maximum is reached at an excitation energy of 286.4 eV, 2 eV above the first peak, revealing the mechanism of populating the core-excitonic state: It requires an additional energy of 2 eV to excite a second electron from the HOMO to the LUMO ("second threshold"). This is why the second plot from below (showing the same exciton population, but shifted by 2 eV to lower excitation energies) bears a basic resemblance with the other absorption spectra: The exciton is populated by the electron stemming from the HOMO (requiring 2 eV), while the core electron takes the 'normal' way of excitation to unoccupied states (of course, the two electrons are indistinguishable, but imagining it this way makes the energy balance easier to understand).

The significant differences between the PFY XAS spectra of the other decay channels (HOMO, HOMO-1,2 and G1–G4) are partly explained by the parity selection rule, although it is weakened by the above-described symmetry-breaking molecular vibrations. An additional effect is produced by the presence of the excited electron in an unoccupied state selected by the excitation energy, distorting the individual occupied molecular orbitals in different ways by its repelling force. For example, the HOMO-1,2 decay channel shows a pronounced maximum at 286.0 eV. These two states with *gerade* parity seem to be pushed towards the carbon atom with the core vacancy at this excitation energy by the excited electron. The increased spatial overlap with the core vacancy enhances this decay channel for that excitation energy, while all others are suppressed, as can be seen by the dips in the respective

PFY spectra at 286.0 eV. This is often seen in RIXS maps: Resonantly enhanced features 'steal' the fluorescence yield from the other decay channels.

4.2 Symmetry-resolved RIXS study of PTCDA

In this Section, the content of which is partly published in [135], the complex electronic structure of ordered multilayers of 3,4,9,10-perylene tetracarboxylic acid dianhydride (PTCDA) on Ag(111) is investigated by means of angle-dependent x-ray absorption spectroscopy (XAS) and angle-dependent resonant x-ray emission spectroscopy (XES) at the carbon K edge. Total fluorescence yield (TFY) XAS is compared with partial electron yield (PEY) data. Beam damage effects, which occur rapidly during XES, were characterized and special care was taken to avoid their influence on the XES spectra. Appropriate selection of excitation energies and detection geometries allows recording element-, atom-, and symmetry-specific XES spectra by making use of dipole selection rules. This specificity, especially the ability to distinguish between occupied σ and π orbitals, gives unprecedented experimental insights into the electronic structure of a large organic molecule. The experimental results are compared with recently published density functional theory calculations of the isolated molecule.

PTCDA is a well-characterized large planar organic molecule serving as a model system for an in-depth understanding of organic semiconductors [17]. The planar molecular structure of PTCDA with labeled non-equivalent carbon atoms is given in Fig. 4.5. The molecule belongs to the point group D_{2h}.

The interaction of PTCDA with many different substrates has been investigated by a large variety of techniques (see [17] and references therein). Depending on the choice of substrate and its crystallographic orientation, the interaction strength between molecule and substrate can be tuned, giving insight into substrate-molecule interactions for a wide variety of systems. This interaction affects many properties of the organic thin film, including the morphology and the growth behavior as a function of temperature.

Previous studies of the electronic structure of PTCDA multilayers were mostly carried out by XAS [5, 6, 8, 14, 16, 136–138] for probing the unoccupied states, and photoelectron spectroscopy (PES) [5, 13, 15, 16, 138–145] for the occupied states. Other techniques include inverse photoemission spectroscopy [146, 147], high-resolution electron energy loss spectroscopy [9, 10, 148, 149], scanning tunneling spectroscopy [144, 150, 151], and photoluminescence [8, 152–156]. For an ordered film, it is convenient to detect the *unoccupied* states in a symmetry-specific way (i.e., by separating contributions from σ^* and π^* orbitals) using dipole selection
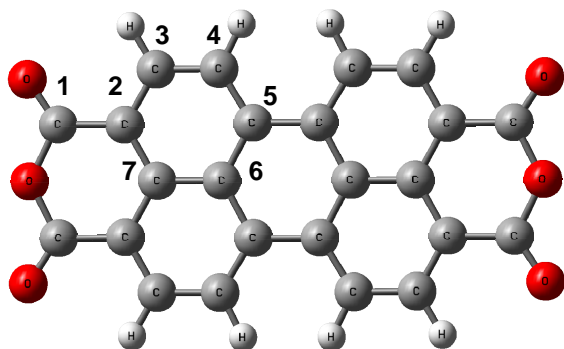
Figure 4.5: Molecular structure of the planar molecule PTCDA (point group D_{2h}). The numbers in the left upper quadrant indicate non-equivalent carbon atoms.

rules in XAS [5, 6, 8, 14, 16, 31, 136–138]. In contrast, for the *occupied* states, the established techniques do not allow a similar symmetry-specific separation. The comparison of density functional theory (DFT) with ultra-violet PES (UPS) measurements [15] shows, that almost all UPS features are a superposition of several occupied electronic states of very similar energies, but possibly of different symmetry. These states cannot be separated even with high experimental resolution due to the intrinsic lifetime broadening of the solid-state photoemission process as well as due to other final state effects (e.g., vibrational broadening). The intermolecular interaction within the multilayer results in the formation of a shallow band structure, leading to further broadening of the spectral features. For a detailed comparison of experiment and theory, it is therefore absolutely necessary to have a symmetry-specific probe for the occupied states. Angle-resolved UPS (ARUPS) with polarized excitation has very similar symmetry selection rules compared to XES [157], which in principle allow symmetry-selective studies, but due to strong variations in the differential cross section, the spectra can not be analyzed quantitatively, making it impossible to separate contributions of different symmetry unambiguously without any additional knowledge. ARUPS studies of PTCDA on various surfaces can be found in [5, 144, 158, 159]. However, none of these publications can distinguish between σ and π orbitals without relying on theoretical calculations. In contrast, angle-resolved resonant XES is able to investigate the occupied states of PTCDA in such a symmetry-resolved fashion. These purely experimental results can be directly compared with theoretical calculations.

Compared to UPS, XES is more specific in a variety of ways, in particular due to the involvement of (resonant) core excitation and by making use of the symmetry selection rules that apply to XES. Resonant XES is always a one-step process [160], requiring a detailed description by the Kramers-Heisenberg formalism. For the interpretation of symmetry-resolved data, however, it is easiest to approximate the photon-in photon-out XES process by two separate dipole transitions as discussed in Section 2.1: The absorption process exciting a carbon *1s* electron into an unoccupied orbital, and the emission of a photon by relaxation of an electron from an occupied molecular orbital into the carbon *1s* vacancy. In the two-step picture, the transition

probabilities of both processes are governed by the dipole matrix elements of Fermi's Golden Rule, which leads to several useful properties of the XES technique. XES is element-specific, because it involves excitation of a certain core level, in our case carbon *1s*, which gives rise to emission at a characteristic photon energy. Further, XES is atom-specific if the molecule contains non-equivalent atoms with different core level binding energies which can be resonantly excited. This is the case for the non-equivalent carbon atoms in PTCDA, as XAS [5, 6, 8, 14, 16, 136–138] and x-ray PES studies [5, 13, 16, 138] show. Finally, XES can also make use of dipole selection rules for both excitation and emission, provided that the exciting beam is polarized and the emission geometry can be varied. These rules can reduce the complexity of spectra for oriented systems if the excitation and emission geometries are chosen such that only transitions for molecular orbitals of a certain symmetry are allowed [31, 37–39, 161, 162]. To date, mainly small molecules like CO, CO_2, NH_3, N_2 or O_2, and some medium-sized molecules like octane, benzene, and glycine adsorbed on various surfaces have been investigated by angle-resolved XES [37–39, 161–172]. Only few publications of resonant XES on large organic molecules can be found [173–178], and to our knowledge no symmetry-resolved studies are among them.

Further advantages of XES are its insensitivity to charging and its large information depth, yielding reliable bulk information about the occupied states of ordered molecular layers. One significant drawback, however, is the ever-present possibility of beam damage by the high-brilliance synchrotron radiation necessary for exciting a sufficient number of XES processes. Such beam damage effects need to be carefully avoided. According to [175], some of the early resonant XES spectra of large molecules [173, 174] are indeed obscured by beam damage effects. A detailed investigation of beam damage mechanisms in organic molecules caused by electronic excitations can, e.g., be found in [179–204]. In our case, as it will be shown shortly, PTCDA multilayers suffer from beam damage effects already after less than one second of irradiation, making it necessary to rapidly scan the synchrotron beam across the sample during data acquisition.

Experimental details

PTCDA multilayers were grown on a Ag(111) single crystal substrate. For preparation, the substrate was first heated to 850K in order to desorb adsorbates from the surface. Then, the crystal was sputter-cleaned at room temperature with Ar^+-ions (1 keV kinetic energy) and subsequently annealed by heating to 850 K. The quality of the Ag(111) crystal surface was checked by low energy electron diffraction (LEED). Then, doubly sublimation-purified PTCDA was evaporated onto the crystal from a Knudsen cell at 540 K (the substrate was kept at room temperature). The evaporation was stopped when the crystal started to show the typical red color
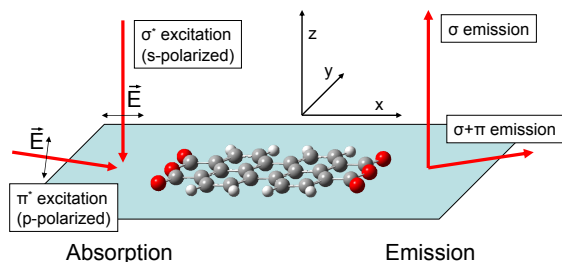
Figure 4.6: Illustration of the normal and grazing geometries for absorption (left) and emission (right). For flat-lying PTCDA molecules, angle-dependent measurements allow the separation of contributions with σ and π symmetry for both, unoccupied and occupied orbitals.

of PTCDA. The layer thickness was determined to approx. 800 nm with an atomic force microscope. Preparation under these conditions is known to yield well-ordered crystalline layers with flat-lying PTCDA molecules [7, 11, 12, 14, 17, 205]. With the substrate at room temperature, it is known that PTCDA forms crystallites of the α as well as the β structure [12, 205].

Angle-dependent XES data was collected at the U41-PGM beamline of BESSY II, Berlin, using the rotatable spectroscopy apparatus ROSA equipped with a computer-controlled motorized sample manipulator and a compact soft x-ray spectrometer (*Scienta Gammadata* XES300) [77]. The combined energy resolution of beamline and spectrometer for the angle-dependent XES spectra was 1.0 eV (full width at half maximum of the Rayleigh line) at the C K edge. The energy axis of all XES spectra was calibrated using 10 Rayleigh lines and polynomial fits of third order in the energy range 264–300 eV. The calibration was performed for each geometry independently to account for small mechanical shifts of the XES spectrometer during rotation of the ROSA analysis chamber.

The measurement geometries are described in Fig. 4.6. On the left hand side, the relevant geometries for absorption (excitation) are shown as a function of polarization of the exciting synchrotron beam (σ^* excitation for s-polarization and π^* excitation for p-polarization). Likewise, Fig. 4.6, right, shows the relevant emission geometries: σ emission for detection along the sample normal, and $\sigma + \pi$ emission for detection in grazing emission.

For beam damage characterization, XES spectra of PTCDA powder pressed in clean Indium foil were recorded at the Advanced Light Source (ALS), Beamline 8.0.2, with the novel x-ray spectrometer described in Section 3.1. With this experimental setup, spectra with a combined energy resolution of 0.4 eV could be collected with high signal-to-noise ratio in a very short time. Each angle-resolved spectrum presented here was accumulated for 30 to 70 minutes, while for each powder spectrum 20 seconds were sufficient. Note that, for all measurements, the samples were continuously scanned. Thus, the given acquisition times are the accumulated total irradiation times taken from many different pristine spots on the sample.

XAS spectra of a PTCDA multilayer on Ag(111) were recorded at BESSY in total

electron yield mode and at the ALS in total fluorescence yield mode. The latter are shown here. A linear correction was applied to the excitation energy such that all spectral features coincide with data carefully calibrated with an electron analyzer [206, 207].

Results and discussion

Fluorescence yield XAS spectra of a PTCDA multilayer on Ag(111) are shown at the top of Fig. 4.7. They were recorded in two different (excitation) geometries, namely s- and p-polarization, as illustrated in Fig. 4.6, left. The spectra in Fig. 4.7 were (arbitrarily) normalized to give overlap below the absorption edge (i.e., below 283 eV) and above 292 eV. The excitation energies used for the resonant XES spectra (discussed below) are indicated by arrows, labels (A–D), and excitation energies. A strong linear dichroism, i.e., a significant difference between the s- and p-polarization spectra in both intensity and shape is evident, which confirms that the PTCDA multilayer is highly oriented and lies flat on the substrate. Due to the dipole selection rules introduced in Section 2.1, this orientation in combination with p-polarization geometry allows only excitation into π^* orbitals. These unoccupied orbitals are anti-symmetric with respect to the molecular plane (xy-plane in Fig. 4.6). In contrast, for s-polarization only σ^* orbitals (which are symmetric to the xy-plane) can be populated.

The p-polarized TFY XAS spectrum in Fig. 4.7 (black solid line) exhibits the same spectral features as the corresponding partial electron yield (PEY) spectrum (blue solid line) [207], a detailed discussion of which is given in [6, 14]. Nevertheless, the intensity ratios do not match due to the self-absorption effects in TFY [64–66]. These effects enhance weak features compared to strong ones, thereby reducing the contrast (compare Section 2.3.2). In the s-polarized spectra, however, a real qualitative difference between TFY and PEY can be found: While the s-polarized PEY spectrum looks similar to the p-polarized one with strongly suppressed π^* peaks, the s-polarized TFY spectrum exhibits comparably strong features at 284.9, 287.4, and 288.4 eV. The latter two features look similar to the spectral signature of the p-polarization spectrum, but the feature at 284.9 eV (red vertical line) has no counterpart in any other multilayer XAS spectrum and can therefore hardly be explained by misaligned molecules in the multilayer. The reason why this peak is seen in TFY and not in PEY must rather be related to the different probing depths of these spectroscopic techniques. While PEY XAS only probes a few monolayers, TFY in s-polarization geometry, i.e., in normal incidence, has a probing depth of hundreds of nanometers. In our special case, at 284.9 eV in s-polarization, we are well below the σ^* absorption edge and therefore in a low-absorption regime with even higher penetration depth comparable to the multilayer thickness of 800 nm.
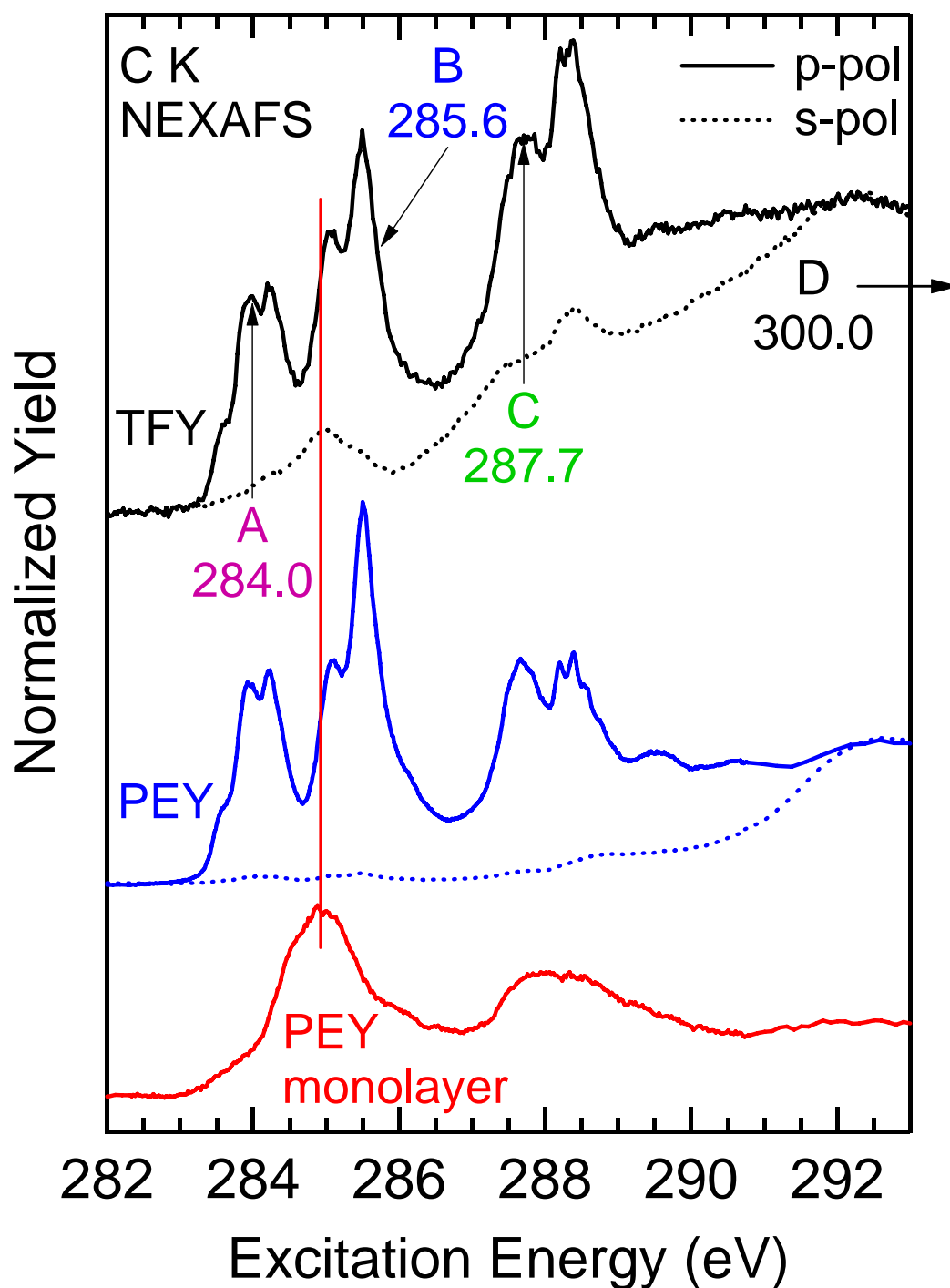
Figure 4.7: The π^* region of total fluorescence-yield (TFY, black) XAS spectra in p- and s-polarization compared to partial electron-yield (PEY) spectra of the multilayer (blue) and the monolayer (red). The PEY data was taken from [207]. The excitation energies used for the resonant XES spectra are labeled A–D and are given in eV.

Thus, a possible explanation for the feature at 284.9 eV is the spectral contribution from the first PTCDA monolayer to the TFY spectrum. Since its mirror symmetry is broken by the presence of the metal surface, the selection rule no longer applies, making the π^* orbitals visible even in s-polarization geometry. This interpretation is corroborated by the fact, that the PEY absorption spectrum of a PTCDA monolayer on Ag(111) (red curve) features a similar peak at 284.9 eV (red vertical line). This peak is known to arise from covalent bonding of the perylene ring to the Ag(111) surface [6] and is therefore only detected for the first monolayer.

While beam damage effects are of lesser importance for the XAS spectra due to their lower excitation intensity, the beam-induced influence on XES spectra has to be carefully checked. For this purpose, Fig. 4.8 contains a series of non-resonant carbon (Fig. 4.8a) and oxygen (4.8b) XES spectra, subsequently taken on the same spot of a PTCDA powder sample. Each spectrum was recorded for 1 s and excited with a photon energy of 300 eV. Note that the O K XES spectra, which were simultaneously measured during the collection of the C K XES series, are only excited by higher harmonics from the beamline undulator and higher orders from the beamline grating, and are thus relatively weak. For better statistics, the experiment was repeated 20 times on pristine sample spots, and the 20 spectra with the same irradiation history were summed up, resulting in a total acquisition time of 20 s per spectrum. The labels show the elapsed irradiation time before the spectra were taken (i.e. the topmost sum of spectra was taken within the 1st second of irradiation, the one below within the 2nd second, etc.). All spectra were normalized to the synchrotron beam intensity. For the C XES spectra (Fig. 4.8a), the prominent effect of irradiation is an intensity variation of the various peaks in the valence structure, overall leading to a line shape with less pronounced features, while the overall carbon intensity remains constant. This indicates the presence of carbon in an increased number of chemical environments. Since the oxygen content decreases upon irradiation (as discussed below), a likely irradiation product is amorphous carbon. Indeed, the XES spectrum with an irradiation time of 20 s looks very similar to C XES spectra of amorphous carbon (compare Fig. 1 in [208]).

Clearly, significant changes are already evident after only 1 s of irradiation. Consequently, all XES spectra discussed in conjunction with Fig. 4.9 have been collected with a dwell time of only 0.1 s on each pristine sample spot. Note that this very short dwell time was chosen to also account for accelerated beam damage during resonant excitation.

Additional information about the beam damage mechanism can be gained from a detailed analysis of the O K XES spectra (Fig. 4.8b). While the line shape does not appear to change significantly as a function of irradiation, we find a significant decrease of the O K XES intensity by 22%, which is corroborated by other XES experiments with resonant excitation at the O K edge. It is important to
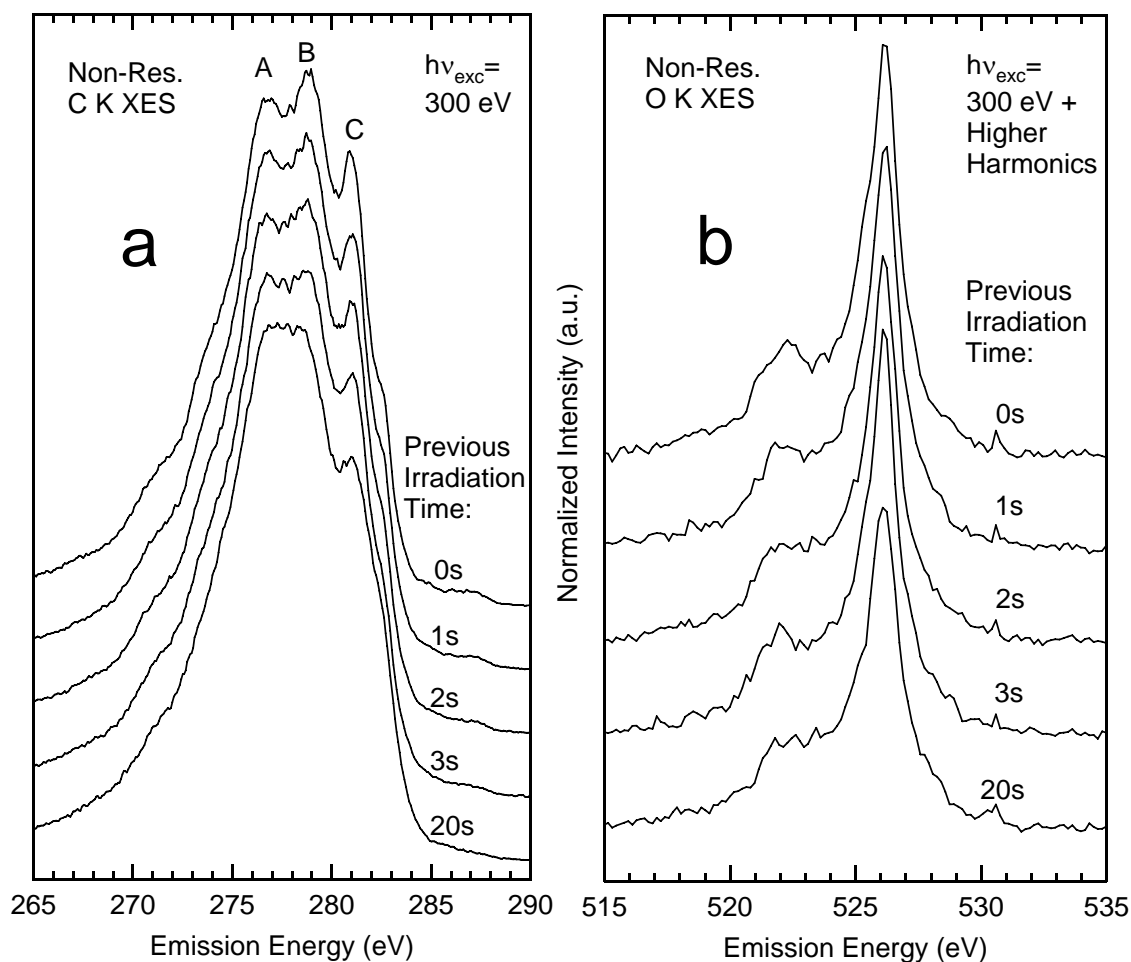
Figure 4.8: High-resolution non-resonant C (left) and O (right) XES spectra of PTCDA powder pressed in In foil (excitation energy: 300 eV), demonstrating beam damage effects. The topmost spectra were taken within the first second of irradiation; further spectra were taken successively thereafter (the collection of a single spectrum took 1 s). In the C spectra (left), first evidence of beam damage can already be observed after 1 s of irradiation, and after 3 s, significant changes have occurred. The spectral shape of the O spectra (right) shows only minor changes upon irradiation, while the spectral intensity drops by 22% after 20 s.

note, that in the shown experiment, the beam damage effect is mainly caused by photons with an energy of 300 eV, while the much weaker higher harmonics of the undulator beamline are used to probe the oxygen atoms. As a side effect of this approach, the beam damage is governed by the penetration depth of the 300 eV beam, while the probing depth of the oxygen XES in combination with the higher harmonics is much higher, considering that the most intense higher harmonic is the 3rd harmonic at 900 eV. Under these experimental conditions, most of the signal contributing to the O XES spectra stems from a depth which is only weakly affected by the beam damage of the 300 eV radiation with its low penetration depth. In consequence, the fraction of O atoms removed within the penetration depth of the 300 eV photons is significantly higher than 22%. The spectra therefore indicate that one of the decomposition mechanisms is associated with a removal of oxygen atoms from the terminal dianhydride groups, such that the overall O K XES intensity decreases while the residual (probed) oxygen atoms still exist in a (relatively) pristine environment.

After the detailed discussion of beam damage effects, we now turn to C XES spectra recorded with an irradiation time of only 0.1 s and correspondingly negligible beam damage. From bottom to top, Fig. 4.9 shows experimental XES spectra with increasing excitation energies A–D as defined in Fig. 4.7. All spectra shown here were excited in p-polarization geometry (no XES line shape changes were observed when comparing spectra with p-polarized and s-polarized excitation geometry at identical excitation energy and identical emission geometry). The emission geometries are illustrated in Fig. 4.6, right. For grazing emission, both σ and π emission are detected (solid lines in Fig. 4.9), while for flat-lying molecules in normal emission, only σ states are observed (dashed lines). Subtracting the dashed lines from the solid lines, we obtain the signature from the π orbitals alone. This difference is given as dotted lines. The lines at 284 eV (for spectrum A), 285.6 eV (spectrum B), and 287.7 eV (spectrum C) represent the elastically scattered lines (Rayleigh lines). Note that the above-described energy calibration for each geometry leads to a small discrepancy between the energy scales of the two geometries, as can be seen in the small shift (0.15 eV) of the Rayleigh lines at excitation energies of 284.0 eV (A) and 285.6 eV (B).

The XES spectra show significant differences between the σ and π emission, as well as strong variations with excitation energy (for the total spectra as well as the σ and π contributions). The former give direct insight into the contributions of the various symmetry states to the overall DOS. The latter can be explained by resonant excitation of selected carbon species within the molecule. The transition matrix elements for the emission process depend on the site of the core vacancy and its overlap with the valence orbitals, resulting in the observed variations in relative intensity of the respective spectral features. *Ab initio* calculations performed with Kosugi's GSCF3 package [209, 210] for 1,4,5,8-naphthalenetetracarboxylic acid
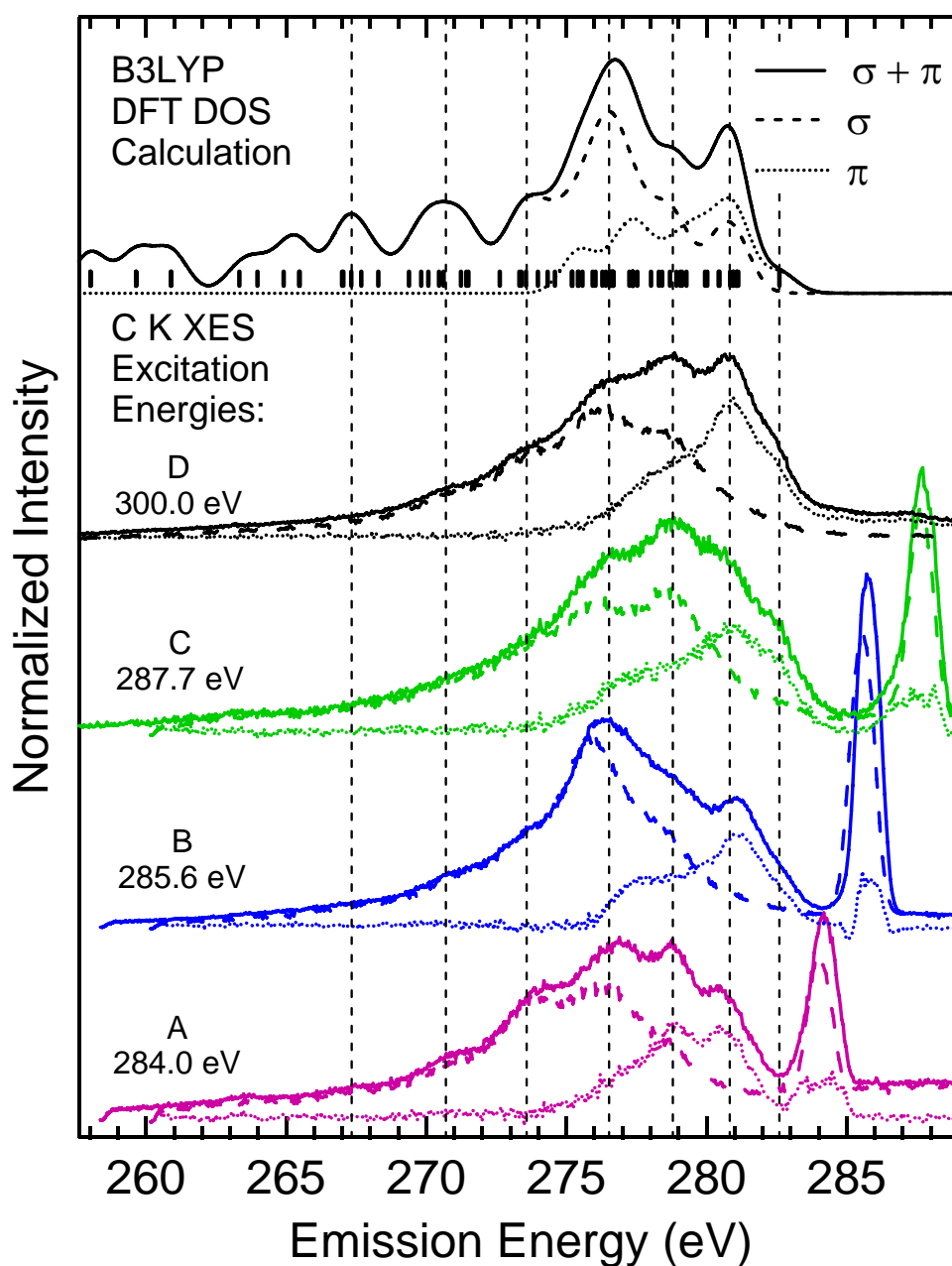
Figure 4.9: Experimental XES spectra, taken at the four excitation energies A–D (see left panel for definition). The solid lines were taken in grazing emission geometry (mixed σ and π emission) and the dashed lines in normal emission (σ emission). In each case, the dotted lines represent the difference between the two spectra (i.e., the π emission). Top: DFT-calculated density of states, broadened by a Gaussion (FWHM 0.5 eV): Total density (solid line), density of σ states (dashed), and density of π states (dots). The short vertical lines designate the energy positions of the occupied orbitals in the DFT calculations in [15].

dianhydride (NTCDA, i.e., a very similar molecule in which the perylene core is replaced by a naphthalene core) [14] and comparison with perylene [6] and unpublished results for PTCDA [207] gives insight into the detailed nature of the various resonances: Excitation at energy A (Fig. 4.7) thus leads to core hole formation at carbon atoms 2–5 (Fig. 4.5), energy B allows excitation of carbon atoms 6 and 7, while energy C creates core holes mainly at carbon atom 1 of the anhydride group. In contrast, non-resonant excitation at 300 eV allows unspecific core hole creation at all carbon sites.

This association allows a tentative discussion of the σ and π contributions in the experimental spectra. For example, the overall spectrum (and, in particular, the σ contribution) appears particularly different at an excitation energy of 285.6 eV (B in Fig. 4.9). Of the four investigated excitation energies A–D, this is the only energy allowing to resonantly excite the carbon atoms 6 and 7. These two are the only carbon atoms positioned on the central high-symmetry axis of the molecule, which apparently greatly enhances the transition rate in the σ channel. Likewise, excitation of atoms 2–5 at excitation energy A appears to enhance the low-energy shoulder of the π emission at 279 eV, indicating a different π-electronic structure (and corresponding XES matrix elements) in that region.

At the top of Fig. 4.9, the B3LYP DFT calculation of a single PTCDA molecule taken from [15] is shown. Therein, the B3LYP basis set was shown to give the best agreement with UPS data. In order to be able to display the calculation on a common energy scale with the experiment, a constant offset was added to the energy positions of the calculated orbitals, such that the highest occupied molecular orbital corresponds to an emission energy of 282.6 eV. The short vertical lines mark the whole set of calculated occupied orbitals. The solid curve above is a representation of the occupied density of states, assembled as a sum of Gauss-peaks with a full width at half maximum of 0.5 eV, one for each molecular orbital. The topmost dashed line is a similarly obtained density of occupied σ orbitals, and the dotted line for π orbitals. In these calculations, the approximated dipole-transition rules by setting the transition rates to 1 for all dipole-allowed transitions and to 0 for all dipole-forbidden transitions.

If we compare the topmost calculated densities of states with the non-resonantly excited XES spectra (300 eV, D), we observe a good agreement of the energy positions of the most prominent features, which are also marked by dashed vertical lines. In addition, like the experimental data, the calculations show dominant σ orbitals (dashed) at lower emission energy and dominant π orbitals (dotted) at higher emission energy. Note that the relative intensities of the main features, as expected, differ between theory and experiment, since the dipole matrix elements for the emission process are not taken into account correctly.
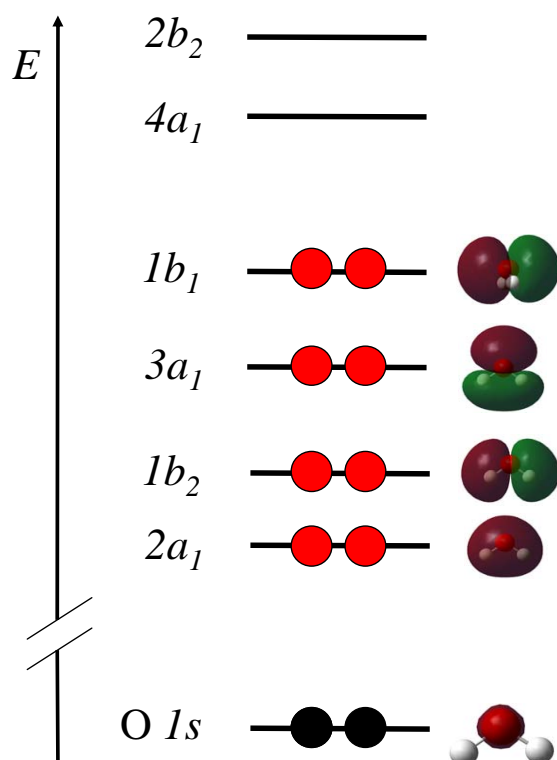
Figure 4.10: The electronic states of H_2O (O *1s* core state and valence states).

4.3 RIXS study of water

Water as the most abundant liquid is the medium of most chemical and biochemical reactions. Before trying to gain a deeper understanding of the latter, for example by investigating aqueous solutions of biologically relevant molecules like in Section 4.4, it is of great importance to thoroughly investigate the properties of water. This liquid is a surprisingly complex substance despite the simplicity of its building blocks, the commonly known H_2O molecules, as ongoing vivid discussions on the local structure of liquid water show [97–99, 101–103, 123, 124, 211–213]. Publications related to the liquid water study shown in this Section are [62, 96, 122, 124, 211, 212].

From neutron and x-ray scattering as well as infrared spectroscopy (see, e.g., [98, 214]) yielding time-averaged geometry information, it is known that a water molecule can have up to four hydrogen bonds (HBs) to neighboring molecules, preferably arranged in a tetrahedral configuration. This ideal 4-fold coordination is realized in all of the known modifications of ice. Upon melting, the rigid HB network becomes dynamic, and some of the bonds break, but the exact nature of this process and the local structure of liquid water are still under discussion despite tremendous experimental and theoretical efforts [71, 98, 99, 102, 103, 116, 215–219].

Recently, it became possible to study the electronic structure of liquids by synchrotron-based methods, viz. x-ray absorption (XAS), photoemission (PES), and resonant x-ray emission spectroscopy (XES) at the O K edge. As illustrated in Fig. 4.10, the valence states of water are the occupied *2a₁*, *1b₂*, *3a₁*, and *1b₁* orbitals, and the unoccupied *4a₁* and *2b₂* orbitals. For liquid water, the former were accessed by PES [105–114] and XES [119, 122, 220], while the latter were studied by XAS [98–101, 116, 215, 218]. For ice, related XES [221], PES [222], and XAS [116] studies are reported, as is the case for gas phase water XES [223], PES [114], and XAS [116]. On the basis of this already existing knowledge about the electronic structure of liquid, gaseous, and solid water, the spectra taken with the equipment introduced in Chapter 3, which were partly published in [62, 96, 124, 211], will be discussed in the following. Special attention will be given to proton dynamics, which is an especially important aspect of liquid water (as outlined below). In order to detect contributions from proton dynamics, it is very helpful to look for isotope effects, i.e., to compare the properties of 'normal' water (H_2O) with that of 'heavy' water (deuterium oxide: D_2O). The deuterium atoms in the latter are chemically identical to the hydrogen atoms of normal water, but they are twice as heavy due to their additional neutron. Therefore, deuterium dynamics are much slower compared to proton dynamics.

For an overview over the unoccupied states of water, the solid lines in Fig. 4.11 show total fluorescence yield XAS spectra of H_2O (blue) and D_2O (red), exhibiting the onsets of the unoccupied *4a₁* and *2b₂* orbitals at excitation energies of 534.5 and 536.5 eV, respectively. Due to saturation effects described in Section 2.3.2 and in [64–67, 71], the intensity of the *4a₁* feature in the H_2O and D_2O spectra appears enhanced as compared to published data [71, 98–101, 116, 215, 218]. D_2O has the same electronic structure as H_2O, except for a slightly less dynamic HB network compared to H_2O at the same temperature [214, 224, 225]. This allows for a stronger HB interaction of the probed molecule with its neighbors and an energetically more favorable arrangement in the initial state of the absorption process, consequently lowering its energy [226, 227]. This effect could explain, why the onset of the D_2O absorption is found at a slightly higher excitation energy compared to H_2O (by approx. 160 meV). A comparable shift is observed for the spectrum of NaOD compared to NaOH solution (red and blue dashed lines). Both spectra exhibit a shoulder at lower excitation energies in addition to the already described features stemming from water, allowing for a resonant excitation of the OH^- and OD^- ions at 533.5 eV as indicated by the vertical line. This possibility will be exploited later.

In order to gain a first overview over the occupied electronic states of liquid water, we compare a non-resonant XES spectrum with PES data reproduced from [114]. Since both techniques have the same final state, the energy positions of the spectral features of XES and UPS should coincide well (except for the constant offset of the
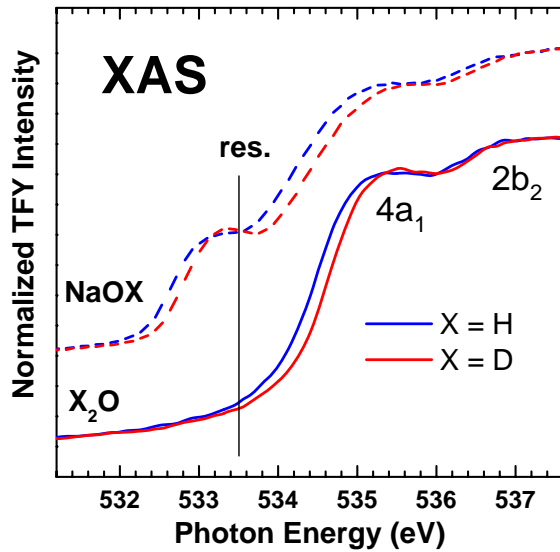
Figure 4.11: XAS spectra of liquid H_2O (solid blue line), D_2O (red line), and of concentrated (25 wt.%) solutions of NaOH in H_2O (dashed blue line) and NaOD in D_2O (dashed red line). All spectra were taken at a temperature of 277 K.

core hole binding energy), according to the final state rule [28–30]. The two major differences of XES and UPS are the transition matrix elements (XES: transition to a core hole, UPS: transition to an unbound state), leading to different relative intensities, and the dynamics, which can occur for XES during the core hole lifetime, but not in the instantaneous photoemission process. In Fig. 4.12, the positions of the spectral features of XES (red line, plotted versus emission energy, upper axis) and UPS (black line, plotted versus binding energy, lower axis) in Fig. 4.12 coincide best when assuming an O *1s* binding energy of 538.7 eV with respect to the vacuum level. This value is reasonably close to the binding energy of 538.1 eV for the O *1s* electron in liquid water reported in [107]. Apart from a small shift of approx. 0.5 eV in the *$1b_2$* position, there are two significant differences between XES and PES: a significantly smaller XES intensity of the *$2a_1$* feature, which had to be amplified by a factor of 20 in order to make it visible, and an additional feature in XES about 0.85 eV below the *$1b_1$* peak, which has no counterpart in PES. The former difference has a simple explanation: the dipole transition matrix element for a radiant transition to the O *1s* core level is very low, since the *$2a_1$* orbital has a dominant s-character at the oxygen site, due to its dominating contribution from the oxygen *2s* level (see Fig. 4.10). The latter difference is much more intriguing, since it is not a pure intensity effect. In XES, the *$1b_1$* orbital appears to be split into two components, with the high-energy (HE) component being at the 'normal' (PES) position of the *$1b_1$* orbital. While this splitting was reported for XES of amorphous ice [221], the worse energy resolution of existing XES studies of the liquid state did not allow to resolve the two components. This new finding suggests the existence of a second species in liquid water, which is responsible for the low-energy (LE) component of the *$1b_1$* peak. Since this species is absent in PES, it seems not inherent to the liquid state of water but rather formed by dynamics
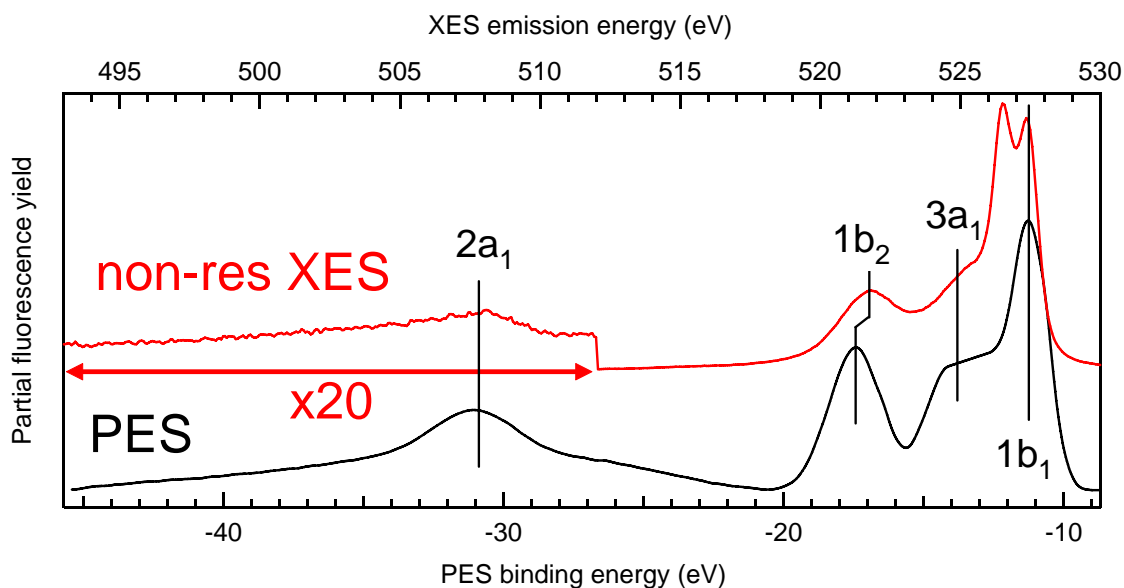
Figure 4.12: Non-resonant XES (red, plotted vs. emission energy, upper x-axis) and PES (black, binding energy, lower axis, reproduced from [114]) spectra of liquid water. Labels indicate the orbitals contributing to the observed spectral features. Below an emission energy of 512 eV, the XES spectrum is multiplied by 20.

during the core hole lifetime (3.6 fs for the O *1s* state according to [50]).

The dynamics during the core-excited state could be either purely electronic (e.g. charge transfer or other screening effects, like observed in [59]) or involve atomic motion, e.g. the dissociation observed in the case of HCl [58]. Due to the large difference in the mass of oxygen and hydrogen atoms, the latter would be clearly dominated by proton dynamics, which are known to take place at a high rate in liquid water, as studies of the unexpectedly high mobility of protons and hydroxide ions indicate [228, 229]. According to these, protons are easily transferred from one water molecule to the other along a hydrogen bond. This kind of ion transport in water is also known as the 'Grotthuss mechanism'. And even in the absence of ions and external influences, water is known to "auto-dissociate", which describes a proton transfer between two adjacent neutral molecules, leading to an H_3O^+- and an OH^--ion.

The question whether proton dynamics is involved in the formation of the unidentified species can be answered directly by comparing XES spectra of heavy water (D_2O) with H_2O. Since in D_2O, the proton dynamics is slower by a factor of almost two (17/9), the formation of that species should be hindered in D_2O if it was linked to proton dynamics. Apart from that, D_2O is known to have the same electronic structure, except for slightly stronger HBs compared to H_2O at the same temperature [214, 224, 225]. An isotope effect in XES of liquid water is reported in [122]

and explained on the basis of proton dynamics, which are influenced by intact HBs. However, this study was not able to resolve the two components.

In the left graph of Fig. 4.13, non-resonant XES spectra (excitation energy: 550 eV) of H_2O (blue) and D_2O (red) are shown for the solid state of amorphous ice (top) and for the liquids (below). In addition, at the bottom of the left graph, a temperature-dependent series of H_2O is displayed. The weak *2a₁* feature is not shown. The comparison of the intensities of the LE *1b₁* component of the two different isotopes demands, that the yet unidentified species is linked to proton dynamics, since its occurrence is strongly reduced for D_2O compared to H_2O, both for amorphous ice and for the liquid. Further, there is a clear temperature dependence: the higher the temperature becomes, the lower the LE component. Consequently, this component is higher for ice than for the liquid. Gilbert *et al.* have even observed, that for crystalline ice, only the LE component remains in the XES spectra [221]. Based on these experimental findings, the following picture develops: the formation of the dynamic species requires and involves proton dynamics, and it is promoted by intact HBs, which number increases for lower temperatures. In crystalline ice, almost all 4 possible hydrogen bonds per molecule are intact, leading to a dominating signal from the dynamic species in Fig. 2 of [221].

Since ultra-fast dissociation was reported in ice [230] and in water vapor for resonant excitation of the unoccupied *4a₁* orbital [231], we should consider this dynamic process as the possible key to the occurrence of our dynamic species. Ultra-fast dissociation on the timescale of the core hole lifetime can lead to two components in XES [58] and Auger electron spectroscopy [231], namely a molecular and a dissociated fraction. Since water dissociates into a proton and an OH^--ion, it might be instructive to compare the spectrum of the dynamic water species with that of highly concentrated NaOH solution.

The strong difference of the intensity of the LE component in D_2O and H_2O XES spectra allows to separate the spectral contributions of the dynamic species from the water spectrum. This is shown in the right graph of Fig. 4.13. The two spectra at the top are again the non-resonant XES spectra of the liquids. In order to separate the components, the D_2O spectrum was subtracted from the H_2O spectrum after rescaling it such that a minimal residual spectrum remains, while avoiding negative intensities. The result is the spectral signature of the dynamic species, denoted as d_2. The same procedure can be applied for extracting the 'normal' water species: Subtracting the H_2O spectrum from that of D_2O results in the component d_1. Both difference spectra are shown in the center of the right graph. As expected, the main features of d_1 and d_2 are the HE and LE components of the *1b₁* orbital, respectively. While in d_1, only the HE component of the *1b₁* orbital is left in agreement with the PES spectrum in Fig. 4.12 and with the gas phase XES spectrum in [223], the d_2-component resembles spectra of NaOH and NaOD solutions, which were excited
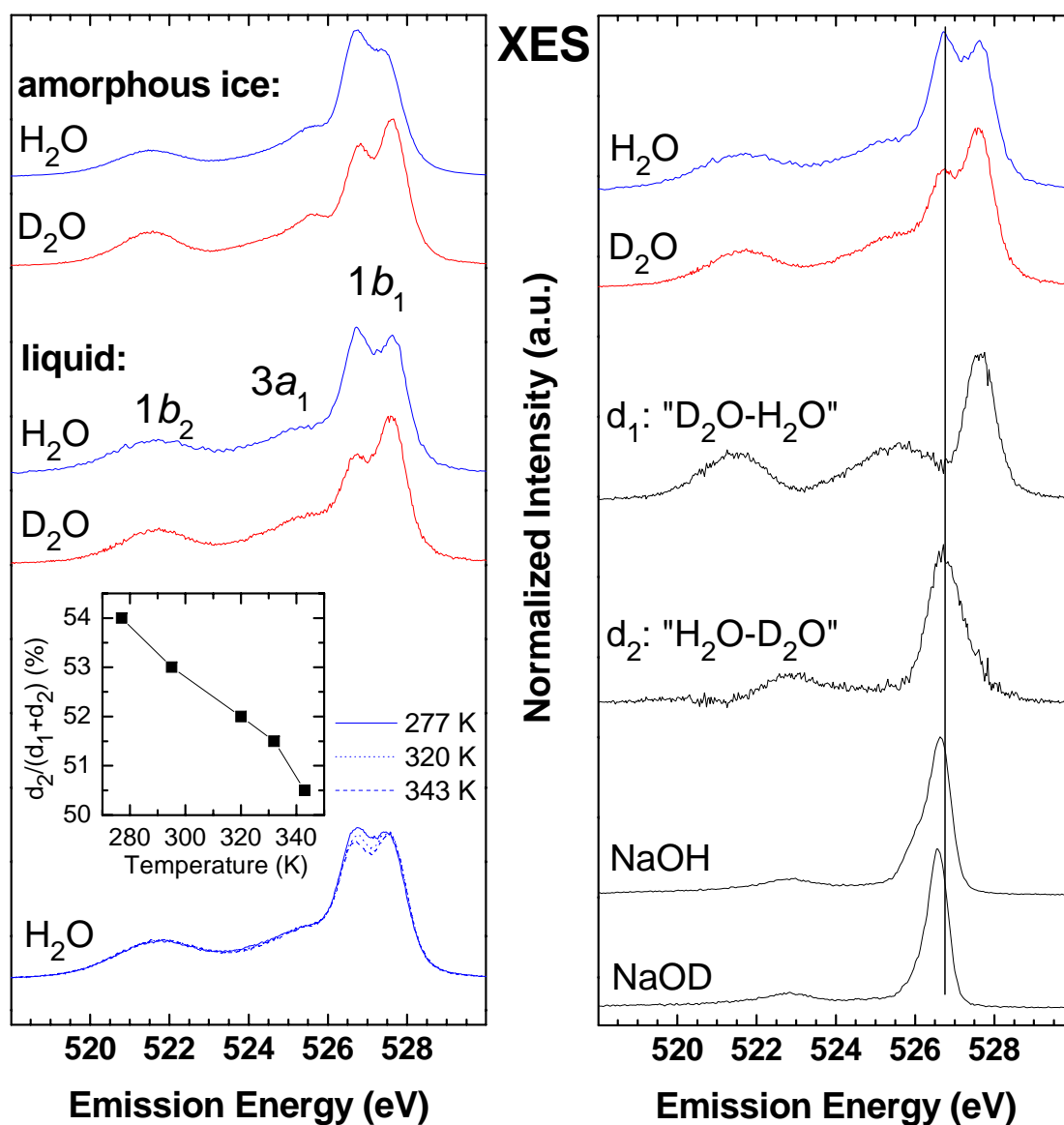
Figure 4.13: Left: Non-resonant XES spectra of H_2O (blue) and D_2O (red) for amorphous ice (top) and the liquids (below). At the bottom, a temperature-dependent XES series of H_2O is plotted. The inset shows the temperature-dependent contribution of the d_2-component (see right panel) to the H_2O spectra. Right: Non-resonant XES spectra of liquid H_2O (blue) and D_2O (red), differences between these spectra (d_1: D_2O-0.62 H_2O, d_2: H_2O-0.87 D_2O), and resonant spectra of NaOH and NaOD solutions ($h\nu$ = 533.5 eV). Unless stated otherwise, the spectra of the liquids were acquired at T = 277 K, those of ice at T $\approx$ 100 K.
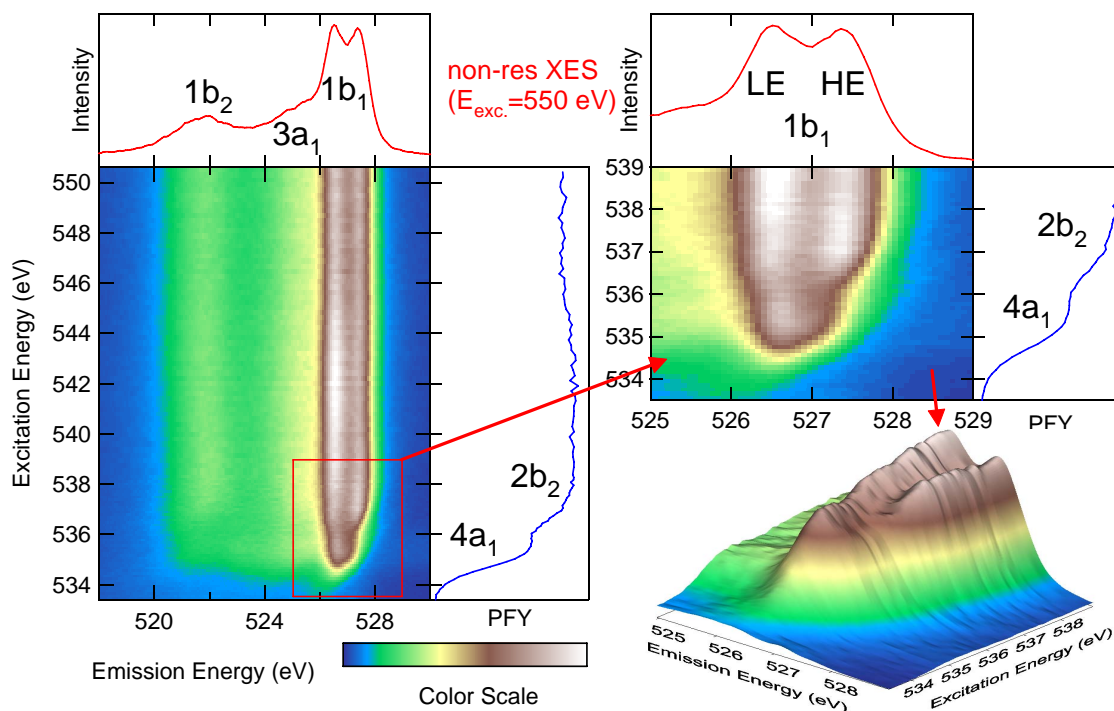
Figure 4.14: RIXS map of liquid water (left: overview, right: detail view of the absorption onset at the $1b_1$ feature), taken at a temperature of 277 K.

below the water edge (at an excitation energy of 533.5 eV as shown in 4.11) in order to suppress contributions from water. Apart from a high-energy shoulder at the main peak of the d_2 component, which might be due to intermediate species occurring during the ultra-fast dissociation process, it looks very similar to the OH^- and OD^- spectra, corroborating the interpretation of d_2 as the dissociated water species.

These findings, and in particular the strong observed isotope effect, lead to the conclusion, that ultra-fast dissociation takes place in liquid water, resulting in the d_2-component in the XES spectra. This dissociation is promoted by the attractive force of intact HBs towards neighboring molecules, which explains the dominance of the dissociated species in the XES spectra of crystalline ice [221], and the fact, that ultra-fast dissociation in gas phase water is only found for resonant excitation into the highly anti-bonding $4a_1$ orbital [231]. The latter result for gas phase water suggests, that the dissociative fraction should also dominate in liquid water for resonant excitation into the anti-bonding $4a_1$ orbital. This can indeed be seen in the 2-dimensional RIXS map of H_2O shown in Fig. 4.14. Below the $2b_2$ onset (excitation energy: 536.4 eV), which is magnified in the 2- and 3-dimensional plots on the right side, the HE component of the $1b_1$ feature at an emission energy of 527.4 eV is suppressed. According to the dissociation model derived above, this can

have two reasons: resonant excitation to the *4a₁* orbital could either lead to selective excitation of highly coordinated water molecules (i.e. with many intact HB bonds) with higher dissociation probability, or it could lead to accelerated dissociation due to a stronger repelling force in that excited state, making dissociation possible on the timescale of the 'core hole clock' even for poorly coordinated molecules. Due to the results for gas phase water [231], where HBs do not play a role, the latter explanation seems very likely, but of course both effects could contribute to the observed finding. The question whether and which distinct HB configurations are resonantly excited upon excitation to the *4a₁* orbital is the subject of ongoing vivid discussions [97–99, 101–103, 116].

From the spectral intensity ratios of d_1 and d_2, neither the concentration of highly coordinated water molecules (i.e. molecules with a high number of intact HBs) can be determined, nor the typical dissociation time can be derived by applying Equation 2.9 (page 20), since the dissociation probability is clearly influenced by both the number of intact hydrogen bonds and the 'core hole clock' timescale, but the relative strengths of these influences are unknown. We can only give an upper limit for the typical dissociation time based on the fraction of the d_2 intensity found in non-resonantly excited H_2O and D_2O spectra. At 277 K, the fraction of d_2 is 54 % for H_2O and 41.5 % for D_2O. Equation 2.9 yields a maximum characteristic dissociation time of 2.2 fs for H_2O and 3.2 fs for D_2O when assuming a core hole lifetime for O *1s* of 3.6 fs [50].

Shortly after publication of these results in [124], Tokushima *et al.* published comparable XES data of liquid water in [123], however with a different interpretation: they believe, that the two components of the *1b₁* represent two different HB configurations of the initial state, although this is in conflict with the strong isotope effect which indicates that the two components occur due to dynamic effects in the intermediate state. Since this interpretation as well as their criticism [212] on the interpretation presented in this thesis is based solely on the results of DFT calculations, it is very interesting in this respect to look at the historical evolution of the results of DFT calculations on XES of liquid water. By the time when XES spectrometers were not able to resolve the two *1b₁* components, also the DFT calculations resulted in only one *1b₁* contribution [119, 122]. In contrast, the DFT calculations used by Tokushima *et al.* to interpret the new high-resolution XES data in [123] and [212] suddenly predict a splitting of the *1b₁* contribution stemming from different initial state HB configurations. And finally, the most recent publication of DFT calculations on water XES [213] presents a splitting of the *1b₁* contribution based on intermediate state dynamics, in agreement with the interpretation of this thesis. In conclusion, it seems that current DFT calculations of such a highly complex system like liquid water require empirical assumptions which introduce too many degrees of freedom, allowing to tune these calculations to yield a multitude of different results. In this context, it seems to be a good choice to
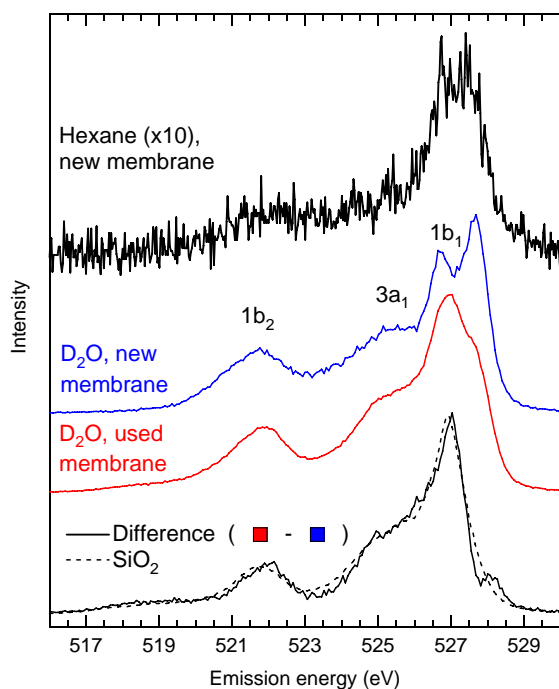
Figure 4.15: Characterization of membrane oxidation effects. Topmost spectrum: oxygen-free Hexane behind a new membrane, amplified by a factor of 10. The spectra below were taken with the same membrane and D_2O in the cell. The blue spectrum was taken with the fresh membrane, and the red one after many hours of irradiation. The bottom spectra are the difference spectrum of the red and blue spectra (solid), and a silicon dioxide reference spectrum (dashed).

base interpretations on pure experimental findings like e.g. the observed isotope effect, rather than on DFT calculations of insufficiently defined systems.

Beam damage effects at the silicon nitride membrane

A major difficulty in obtaining meaningful and reliable spectra of liquid water was a beam-induced oxidation of some silicon nitride membranes. It turned out that with increasing irradiation time, the LE component of the *1b₁* orbital in the water XES spectra sometimes increased due to a formation of silicon dioxide at the membrane-water interface. Fig. 4.15 shows the most extreme cases found during the experiments with D_2O. The topmost spectrum verifies, that the pristine membrane showed no spectral contributions at the oxygen edge other than a weak signal (magnified by a factor of 10) presumably from a thin water layer on the inner membrane surface. Since the 100 nm thin membranes are destroyed by the synchrotron beam without a cooling liquid behind them, the cell was filled with water-free hexane (C_6H_{14}). The blue spectrum below shows a spectrum of D_2O taken with the same membrane. It looks like a typical D_2O spectrum similar to those discussed above. The red spectrum shows the same experiment with a used membrane after many hours in the synchrotron beam. It exhibits additional spectral intensity compared to the blue spectrum, which was isolated by subtracting the blue spectrum. The result is shown in the spectrum at the bottom of the graph (solid line). It looks

very similar to a silicon dioxide reference spectrum (dashed line).

These results suggest, that the excitation of water with x-rays, appearing right at the membrane-water interface, produces aggressive oxygen and/or hydroxide radicals as a result of the dissociation of water molecules discussed above. Since this effect was only observed for some membrane batches, it can be speculated, that membranes with a silicon-rich stoichiometry are more sensitive to those radicals. According to the manufacturer of these membranes (*Silson Ltd.*), the stoichiometry is not thoroughly controlled and checked during and after the manufacturing process. Since the spectral contributions of silicon oxide lead to spuriously enhanced intensity coinciding with the positions of the spectral features of water (as seen in Fig. (4.15), it is very important to always keep track of membrane contributions at the oxygen edge. As an additional measure, silicon nitride membranes from other manufacturers (e.g. *NTT Advanced Technologies* or *SPI supplies*) should be tested.

4.4 XAS and XES study of amino acids

The 22 naturally occurring amino acids are the building blocks of many biologically relevant macromolecules, with the most prominent representatives being peptides and proteins [232]. While the geometric structure of such macromolecules is being studied by x-ray crystallography and nuclear magnetic resonance spectroscopy [233], little is known about the electronic structure of bio-molecules in their native environment, i.e., in aqueous solution. Many unanswered questions like the origin of the Hofmeister series [18, 19], the mechanism of the selective permeation of ion channels in bio-membranes [20, 21], and the interaction of anti-freeze proteins with water [234] are strongly linked to the electronic structure of proteins in solution and their interaction with water and ions. And even the local electronic structure of the seemingly simple system of liquid water itself as the liquid medium of all biochemical reactions, is still mysterious in many respects, as discussed in Section 4.3.

In literature, the electronic structure of amino acids and peptides was mostly investigated by x-ray absorption and x-ray photoemission spectroscopy (XAS and XPS) of the solid state [118, 203, 204, 235–249]. Few investigations of the occupied valence states of the solid phase are reported, some by ultra-violet photoemission spectroscopy (UPS) [235, 248], and one XES study of glycine [169, 237, 238]. Gas phase studies of the electronic structure of amino acids have been carried out by means of XAS [244, 250, 251] and PES [252–258].

Amino acids crystallize in the *zwitterionic* state, resulting in the salt-like appearance of the amino acid powders, which possess high melting points due to the ionic intermolecular bonds. A lot more interesting are amino acids in aqueous solutions. Then, their net charge depends on the pH-value due to its influence on dynamic protonation and deprotonation processes as discussed below. Studies of the electronic structure of amino acids in aqueous solution are very rare due to the technical difficulties described in Section 3.2. Recently, first pH-dependent XAS [70, 259] and XPS spectra [105] of aqueous solutions of amino acids were reported.

Experimental details

All spectra were recorded at the Advanced Light Source, beamline 8.0.1, the energy of which was calibrated at the nitrogen K edge by recording an XAS spectrum of N_2 gas. The absorption energies of all vibrational N_2 resonances are well-known from electron energy loss spectroscopy [260]. The XES spectra were taken with the permanently installed SXF endstation [76], the energy scale of which was calibrated at the high-energy side with several elastically scattered monochromatic beams of the calibrated beamline. Due to the known nonlinearity of the energy scale for Rowland type spectrographs, the low-energy side might be slightly off. The XAS measurements were acquired in the fluorescence yield (FY) mode. For the half-saturated liquid solutions (12.5 g/100 ml for glycine and 2 g/100 ml for histidine), the liquid cell described in Section 3.2 was used in combination with nitrogen-free silicon carbide (SiC) membranes. The pH-values were adjusted by adding appropriate amounts of sodium hydroxide (NaOH) pellets.

Radiation sensitivity of amino acid powders

As already outlined in Section 4.2, a problem for synchrotron studies of organic molecules is the high x-ray intensity, which can cause severe beam damage within less than a second of irradiation. Such decomposition processes of organic molecules caused by electronic excitation were studied in much detail with many techniques [179–204, 251, 261, 262]. For amino acids, possible pathways of beam damage are dehydration, decarboxylation, decarbonylation, deamination and desulfurization accompanied by desorption of H_2, H_2O, CO_2, CO, NH_3 and H_2S and an increasing number of C–O and C–N double and triple bonds [203]. Therefore, possible beam-induced effects have to be ruled out carefully for all techniques involving photon and electron irradiation, and especially for XES due to the extremely high radiation intensity.
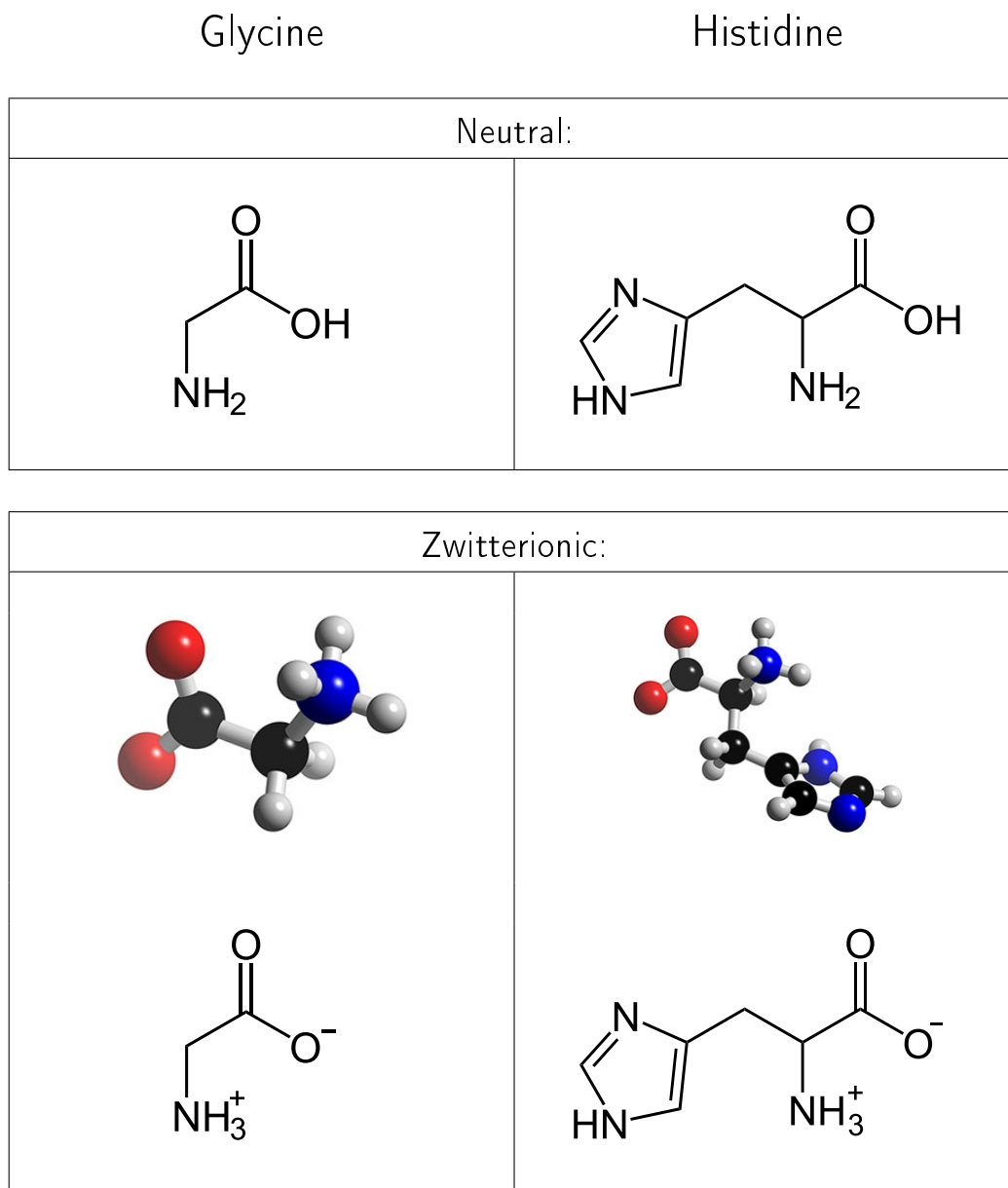
Glycine   Histidine

Figure 4.16: Neutral (top) and zwitterionic (bottom) chemical structures of glycine (left) and histidine (right).
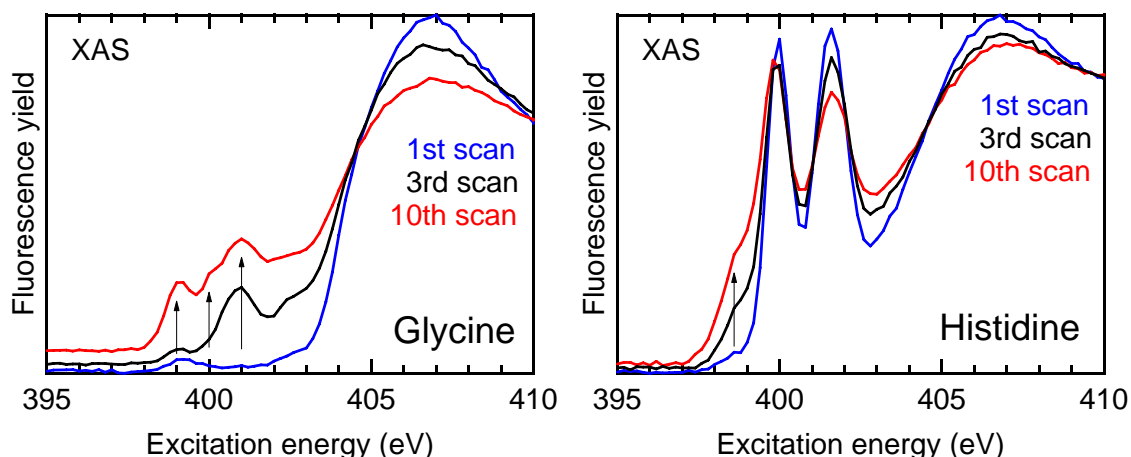
Figure 4.17: Consecutive XAS spectra of glycine (left) and histidine (right) in powder form. The first scans (blue) were taken on pristine sample spots. Arrows indicate additional π^*-resonances appearing as a result of beam-induced deprotonation.

In Fig. 4.16, the chemical structures of glycine (left) and histidine (right) are shown. The topmost images are representations of the *neutral* form. Below, the chemical structures of the *zwitterionic* forms are displayed as 3D- and 2D-representations. Of particular interest are the nitrogen atoms, since their local electronic structure is probed in the spectra discussed below. The glycine molecule possesses only one nitrogen atom, which forms the amino group (NH_2), while histidine offers 3 chemically different nitrogen atoms, one again of the amino group, and two inside the imidazole ring: One is involved in a C=N double bond, while the other has a non-binding lone pair orbital.

Fig. 4.17 shows scan number 1, 3, and 10 of XAS beam damage series of glycine (left) and histidine (right) in powder form. Each spectrum was normalized to the photoeffect current of a clean gold grid, which is proportional to the intensity of the synchrotron beam passing through it. The series spectra started at pristine spots (bottom spectrum) on the powder samples pressed into clean Indium foil. For glycine, significant beam damage effects are already evident in the third spectrum (black), despite the fact that one spectrum took less than 2 minutes and both entrance and exit slits of the beamline monochromator were closed to the minimum settings. The most prominent change is a build-up of several pre-peaks (indicated by arrows), which are π^*-resonances of C–N double and triple bonds resulting from deprotonation [203]. For histidine (right series of Fig. 4.17), strong π^*-resonances belonging to the C=N double bond of the imidazole ring are detected already for the first (blue) scan at 400.0 and 401.6 eV excitation energy. The latter resonance decreases with increasing beam damage, indicating the deprotonation of the imidazole ring. In parallel, at an excitation energy of 398.5 eV, a shoulder is rising with

increasing beam damage due to the formation of additional C–N double and triple bonds. The first spectra, i.e., from pristine spots of both amino acid samples, are similar to published solid state XAS spectra of glycine and histidine [240].

PH-dependence of amino acid solutions

For the study of aqueous solutions with the liquid flow cell, beam damage effects are far less severe compared to the situation in powders, since the rapid flow will remove a large fraction of the dissociation products. Of course, the membrane has to be checked frequently for deposited beam damage products.

In aqueous solution, the carboxyl group (COOH) acts as an acid (proton donor) in amino acids, while the amino group (NH_2) is a base (acceptor). In order to accurately describe the pH-dependent concentrations of different species of the dissolved amino acids, we need to treat the dynamic equilibria of all potential proton acceptors and donors separately, since they have different acidity constants pK_a, defined in the law of mass action as:

$$pK_a = -\log_{10}(K_a) = -\log_{10}\frac{[H^+] \cdot [A^-]}{[HA]} = -\log_{10}\frac{[A^-]}{[HA]} - pH. \qquad (4.1)$$

'A' denotes the deprotonated anionic rest. Strictly speaking, the H^+ ion does not exist as such. It reacts with water to H_3O^+, but for the quantitative analysis, this reaction can be disregarded for the sake of simplicity as long as water is abundant, i.e. for sufficiently diluted solutions.

If the acidity constant pK_a of a certain proton accepting or donating group is known, the fraction of protonated groups can be expressed as a function of the pH-value, as derived from Equation 4.1:

$$\frac{[HA]}{[A^-] + [HA]} = \frac{1}{1 + 10^{(pK_a - pH)}}. \qquad (4.2)$$

Since the pK_a of the carboxylic and the amino group of amino acids are relatively universal, their average values can be used to calculate the protonated ratios as a function of pH. According to [263], the pK_a of the carboxylic group is 2.1 ± 0.3 and that of the amino group 9.5 ± 1.5. The error bars are due to differences between the various amino acids. In the special case of histidine with its imidazole ring, the nitrogen lone-pair orbital can accept another proton depending on the pH-value of the solution. The pK_a of the lone pair nitrogen atom in the imidazole ring of histidine is 6.0 [263]. These values were inserted into Equation 4.2 to calculate the protonated

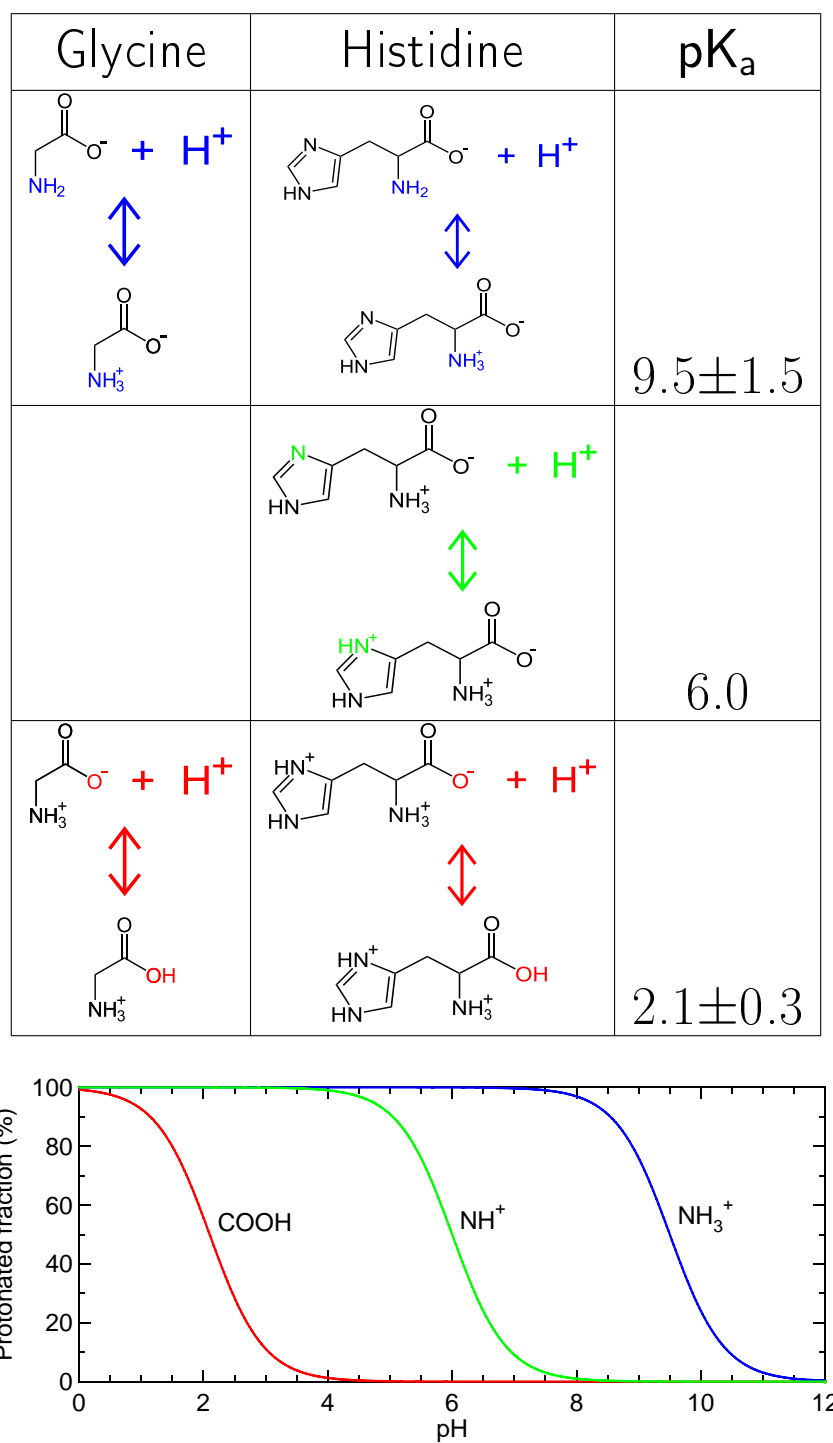| Glycine	Histidine	pK$_a$
		9.5±1.5
		6.0
		2.1±0.3

Figure 4.18: Table: all possible protonation reactions for glycine (left) and histidine (center) and their pK$_a$ values (right) according to [263]. Bottom graph: The protonated fractions of the carboxylic (red) and amino (blue) groups of glycine and histidine, and the imidazole (green) group of histidine as a function of pH.
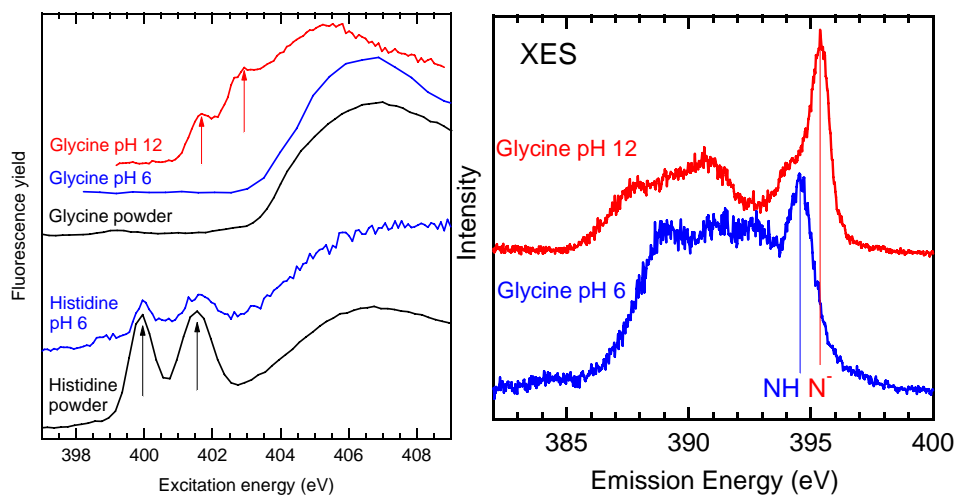
Figure 4.19: Left: XAS spectra of glycine and histidine powder (black), pH 6 solution (blue) and glycine in pH 12 solution (red). Arrows indicate additional π^*-resonances appearing as a result of deprotonation. The black arrows are indicative for a beam-induced deprotonation of the imidazole group in histidine powder, and the red arrows indicate deprotonated amino groups in glycine induced by the high pH-value. Right: Non-resonantly excited x-ray emission spectra of glycine at pH 6 and 12. Two separated features indicate protonated (blue line) and deprotonated amino groups (red line).

fractions of these three groups. The three possible protonation/deprotonation reactions for glycine and histidine (amino group, imidazole ring, and carboxyl group) with their pK_a-values and the fractions of the protonated species as a function of pH are displayed in Fig. 4.18. The protonation of the amino group is color-coded in blue, the imidazole ring in green, and the carboxyl group in red.

At moderate pH, the zwitterionic state with its characteristic COO^- and NH_3^+ groups is dominating. This is the reason, why the XAS spectra of the powders (black) in the left panel of Fig. 4.19 are qualitatively similar to those in aqueous solution at a pH of 6 (blue). In solutions, the interaction of the nitrogen atoms with the surrounding water seems to be rather weak, since otherwise significant changes would be expected in the spectra compared to the solid state. However, there is one quantitative difference in the histidine spectra, which have been normalized to the edge jump: the two pre-peaks (marked with black arrows in the left of Fig. 4.19) are much more intense in the powder spectrum as compared to the pH 6 solution. According to the bottom graph of Fig. 4.18 these features are indicative of the deprotonated imidazole ring, since it should have a fraction of $\approx 50\%$ at a pH of 6, and 100% in the powder.

The glycine XAS spectrum at a pH of 12 exhibits two features marked with red arrows, which are indicative of the deprotonated amino group. This interpretation becomes obvious when comparing the pH 12 spectrum with a spectrum of

gaseous glycine [244]. The gas spectrum exhibits exactly the same two features with comparable intensity compared to the pH 12 spectrum. In contrast to the solid zwitterionic state, amino acid molecules in the gas phase are in neutral form. As depicted on the top of Fig. 4.16, this form has a deprotonated (i.e. neutral) amino group, thus leading to the same local electronic structure at the nitrogen atom as in the case of the pH 12 solution. Furthermore, both spectra from the glycine solution are in excellent agreement with the N K spectra at pH 6 and 12 published by Messer et. al. [70], who came to the same conclusion. It is also note-worthy that for such diluted solutions, the saturation effects of fluorescence yield XAS spectra are hardly noticeable, as discussed in 2.1. This can be seen in the relative heights of the two onsets marked by the red arrows at pH 12 compared to the main edge. The intensity ratios of the three steps at the absorption onset are equal to those in the electron yield spectra in Fig. 6 of [70].

Similarly obvious changes are evident as a function of pH in the non-resonant x-ray emission spectra of glycine shown in the right panel of Fig. 4.19. In contrast to the XAS spectra, which offer distinct spectral features only for deprotonated nitrogen species, in XES of glycine at pH 6 (protonated amino group) and 12 (deprotonated), clear spectral features indicative of both protonated (blue line) and deprotonated (red line) amino groups are evident.

Summary and outlook

The liquid cell introduced in part 3.2 has shown its potential to allow the study of amino acid powders and solutions at the previously inaccessible nitrogen edge. PH-induced protonation and deprotonation of the amino group of glycine have a characteristic influence on the XAS and XES spectra. This important step was made possible by the use of silicon carbide membranes manufactured by *NTT Advanced Technologies*. The analysis of beam damage for the powders shows, that one must be aware of possible radiation-induced dissociation of the molecules.

The next step must be to record high-quality RIXS maps as described in 2.3.1 with the novel spectrometer introduced in 3.1. An example of a liquid water RIXS map is given on page 69. Since the preliminary results in this Section have already demonstrated a high sensitivity of XAS and non-resonant XES for the electronic state of amino acids, RIXS maps at all relevant edges (C K, N K, and O K and for some amino acids S $L_{2,3}$) will probably provide a wealth of novel information, especially when recorded at selected pH-values. From the bottom graph of Fig. 4.18, it can be derived, that glycine features three distinct states of protonation at pH 0 (carboxyl and amino group protonated), 6 (amino group protonated), and 12 (deprotonated). Histidine with its additional protonation path at the imidazole ring

has even four distinct states at pH 0, 4, 7.5, and 12. The protonation of the carboxyl group should have a visible effect on the oxygen spectra even though they will be dominated by the water signal, the nitrogen spectra will be most sensitive to changes in the amino and imidazole groups, while the carbon spectra should be affected by all protonation/deprotonation reactions.

4.5 Summary of Chapter 4

Chapter 4 contains x-ray absorption spectroscopy (XAS) and resonant inelastic x-ray scattering (RIXS) studies of the electronic structure of organic molecules in solid (powders) and liquid form (aqueous solutions), thereby demonstrating the potential of the technical developments shown in the previous Chapter.

In Section 4.1, the RIXS map technique (see 2.3.1) was used to study C_{60} molecules with negligible intermolecular interaction. The results of a previous conventional RIXS study [63] could be confirmed and extended by experimental data superior in both quantity and quality. The RIXS map taken in only 25 minutes allows a quantitative analysis of energy differences and slopes, yielding, for example, the HOMO–LUMO distance. It also identifies a core-excitonic state and facilitates a quantitative comparison of its binding energy with that of valence excitons in C_{60}. Furthermore, decay-channel resolved partial fluorescence yield XAS spectra can be extracted from the RIXS map, yielding information on the population of the core-excitonic state as a function of excitation energy. All results are of purely experimental nature without having to rely on quantum-mechanical simulations.

Section 4.2 contains a symmetry-resolved XAS and RIXS study of a highly ordered, flat-lying PTCDA multilayer on a Ag(111) surface, thereby demonstrating how vital an efficient x-ray spectrometer is for investigating organic molecules suffering from beam damage effects. These rapidly occurring effects are characterized on the basis of irradiation-time dependent series of C and O XES spectra. Upon varying the excitation energy and emission geometry, atom- and symmetry-specific carbon K XES spectra with negligible beam damage effects are obtained that give direct insight into the electronic structure in σ and π symmetry. A DFT calculation of the PTCDA molecule [15] reproduces the energy positions of the most prominent emission features remarkably well. In addition, the energy positions of the σ and π emissions agree well with the calculated energies of the respective orbitals.

The liquid cell presented in detail in Section 3.2 was used in Sections 4.3 and 4.4 to record RIXS spectra of liquid water and aqueous solutions of amino acids, respectively. In the case of water, a comprehensive oxygen K RIXS map was recorded and analyzed in detail. A temperature-dependent comparison with XAS and RIXS

data of deuterium oxide (heavy water), sodium hydroxide, and sodium deuteroxide leads to the conclusion, that ultra-fast dissociation takes place in liquid water on the timescale of the oxygen *1s* core hole lifetime, resulting in a distinct spectral contribution in the RIXS spectra. The dissociation is promoted by intact hydrogen bonds with neighboring molecules.

Section 4.4 contains pH-dependent XAS and XES studies of the amino acids glycine and histidine at the nitrogen K edge, both for powders and aqueous solutions. For this purpose, novel nitrogen-free silicon carbide membranes are used. The aqueous solutions are analyzed at pH-values of 6 and for glycine also at pH 12. A pH-value of 12 causes deprotonation of the amino group, leading to significant changes in the nitrogen spectra as compared to pH 6.

The present results were made possible by the technical developments introduced in Chapter 3, namely the high-transmission x-ray spectrometer and the temperature-controlled flow-through liquid cell. First results with the meanwhile finished next-generation liquid cell (see Section 3.3) on acidic acid and amino acid solutions [264] show, that with this novel experimental setup, it is possible to routinely record comprehensive high-quality RIXS maps of liquids at different pH-values, temperatures, and concentrations in a short time, which promises to open up completely new possibilities for studying the electronic structure of liquids. But also for more conventional experiments like band structure studies on solid state samples, the novel RIXS map approach reveals unprecedented details, as has been shown in [60].

SUMMARY

In this thesis, soft x-ray absorption spectroscopy (XAS) and resonant inelastic x-ray scattering (RIXS) studies of the electronic structure of selected organic molecules and liquids were carried out. The first part focuses on the used experimental techniques and the development of the instrumentation necessary for these studies, namely a soft x-ray emission spectrometer, and a temperature-controlled flow-through liquid cell. The former was optimized by a special analytical ray tracing method developed exclusively for this purpose. Due to its high transmission, the spectrometer facilitates a novel experimental approach of recording comprehensive 'RIXS maps', which are 2-dimensional plots of x-ray scattering intensities as a function of both, excitation and emission photon energy. The liquid cell extends these possibilities to the study of liquids, especially the interaction of molecules in liquids and their chemical reactions under well-controlled conditions.

Organic molecules have attracted considerable attention in the last decade. The intense research activities related to these materials have two main motivations: on the one hand, organic molecules have a technological application as building blocks of organic semiconductors, while, on the other hand, organic molecules are the functional elements in biological systems.

In order to cost-effectively produce optimized organic electronic devices, a fundamental knowledge of the electronic properties of the overwhelming manifold of organic molecules and the metal-organic interface is necessary. Therefore, many studies of the electronic structure of potential candidates for organic electronics exist. Two of these candidates, namely C_{60} ('Buckminsterfullerene') and well-ordered multilayers of 3,4,9,10-perylene tetracarboxylic acid dianhydride (PTCDA) on a Ag(111) surface are investigated in this thesis.

For the study of C_{60} molecules, a comprehensive 'RIXS map' was recorded and analyzed. The results of a previous conventional RIXS study could be confirmed and extended. The RIXS map taken in only 25 minutes allows a quantitative

analysis of energy losses, yielding for example the HOMO–LUMO distance (i.e. the distance between valence and conduction band). It also identifies a core-excitonic state and facilitates a quantitative comparison of its binding energy with that of valence excitons in C_{60}. Furthermore, decay channel-selective partial fluorescence yield XAS spectra can be extracted from the RIXS map, yielding information on the population of the core-excitonic state as a function of excitation energy.

As a second model system of organic molecules relevant for organic electronics, PTCDA was chosen. The complex electronic structure of the occupied states of a highly ordered, flat-lying PTCDA multilayer on a Ag(111) surface was investigated by symmetry-resolved resonant x-ray emission spectroscopy. The rapidly occurring beam damage effects were characterized on the basis of irradiation-time dependent series of C and O x-ray emission spectra. Upon varying the excitation energy and emission geometry, atom- and symmetry-specific carbon K emission spectra with negligible beam damage effects were obtained that allow to distinguish between electronic states with σ and π symmetry. A density functional theory calculation of the PTCDA molecule reproduces the energy positions of the most prominent emission features remarkably well. In addition, the energy positions of the σ and π emissions agree well with the calculated energies of the respective orbitals.

In order to shed light on the second aspect of organic molecules, namely their role in biological systems, first a detailed investigation of the electronic structure and proton dynamics of liquid water as the medium of most chemical and biochemical reactions was carried out. Therefore, a comprehensive oxygen K RIXS map of liquid water was recorded and analyzed in great detail. A temperature-dependent comparison with XAS and RIXS data of deuterium oxide (heavy water), sodium hydroxide, and sodium deuteroxide leads to the conclusion, that ultra-fast dissociation takes place in liquid water on the timescale of the oxygen *1s* core hole lifetime, resulting in a characteristic spectral contribution in the RIXS spectra. The dissociation is promoted by intact hydrogen bonds with neighboring molecules. In consequence, the rate of dissociation directly depends on the initial hydrogen bond configuration.

In the next step towards biologically relevant systems, the nitrogen K edges of the amino acids glycine and histidine were investigated in powderous form as well as in their native environment, namely in aqueous solution. X-ray absorption and emission spectra of the aqueous solutions were analyzed at pH-values of 6 and for glycine also at pH 12 and compared to the spectra of powders. A pH-value of 12 causes deprotonation of the amino group, leading to significant changes in the nitrogen spectra as compared to pH 6.

The results from these four examples demonstrate that a wealth of novel information can be obtained by using the new experimental tools developed in this thesis, namely a highly sensitive x-ray spectrometer and a flow-through liquid cell.

ZUSAMMENFASSUNG

Diese Arbeit beschäftigt sich mit der Untersuchung der elektronischen Struktur ausgewählter organischer Moleküle und Flüssigkeiten mittels Röntgenabsorptionsspektroskopie (XAS) und resonanter inelastischer Röntgenstreuung (RIXS). Der erste Teil beschreibt die verwendeten spektroskopischen Methoden und die Entwicklung der dafür notwendigen Geräte, insbesondere eines Röntgenspektrometers und einer temperierten Durchflussnasszelle. Ersteres wurde mittels einer eigens dafür entwickelten analytischen Raytracing-Methode optimiert. Aufgrund seiner hohen Transmission ermöglicht das Spektrometer einen für weiche Röntgenstrahlung neuartigen experimentellen Ansatz, nämlich die Aufnahme einer umfassenden 'RIXS-Karte'. Das ist eine 2-dimensionale Auftragung der Röntgenstreuintensität als Funktion der Anregungs- und der Emissionsphotonenenergie. Die Nasszelle erweitert diese experimentellen Möglichkeiten auf die Untersuchung von Flüssigkeiten, speziell auf deren Wechselwirkungen in Flüssigkeiten und ihre chemischen Reaktionen unter wohldefinierten Bedingungen.

Organische Moleküle haben im letzten Jahrzehnt erhebliche Aufmerksamkeit auf sich gezogen. Die intensiven Forschungsaktivitäten an diesen Materialen haben zwei Hauptmotivationen: einerseits haben organische Moleküle technologische Anwendung als organische Halbleiter, und andererseits sind organische Moleküle die funktionalen Einheiten in biologischen Systemen.

Um optimierte organische Halbleiterbauelemente kostengünstig produzieren zu können, muss man über die elektronischen Eigenschaften der organischen Moleküle und der Metall-Organik-Grenzfläche genauestens Bescheid wissen. Deshalb wurde bereits eine Vielzahl an Untersuchungen potentieller Kandidaten für organische Halbleiterbauelemente durchgeführt. Zwei dieser Kandidaten, nämlich C_{60} ('Buckminster-Fulleren') und wohlgeordnete Multilagen von 3,4,9,10-Perylen Tetracarboxylsäure Dianhydrid (PTCDA) auf einer Ag(111)-Oberfläche werden in dieser Arbeit untersucht.

Für die Untersuchung der C_{60} Moleküle wurde eine RIXS-Karte aufgenommen und analysiert. Damit konnten die Resultate eines früheren konventionellen RIXS Experiments erweitert werden. Die in nur 25 Minuten aufgenommen RIXS-Karte erlaubt eine quantitative Analyse von Energieverlusten, woraus sich direkt die HOMO–LUMO Distanz ergibt (d. h. der Abstand zwischen Valenz- und Leitungsband). Außerdem lässt sich die Existenz eines rumpfexzitonischen Zustands beobachten, dessen Bindungsenergie man quantitativ mit der Valenzexzitonenbindungsenergie in C_{60} vergleichen kann. Überdies können aus der RIXS-Karte Zerfallskanal-selektive Fluoreszenzausbeute XAS Spektren extrahiert werden, die zum Beispiel Auskunft über die Besetzung des rumpfexzitonischen Zustands als Funktion der Anregungsenergie geben.

Als zweites Modellsystem wurde PTCDA ausgewählt. Die komplexe elektronische Struktur der besetzten Zustände von hochgeordneten, flach liegenden PTCDA Multischichen auf einer Ag(111)-Oberfläche wurde mittels symmetrieaufgelöster resonanter Röntgenemissionsspektroskopie untersucht. Die dabei rasch einsetzenden Strahlenschäden wurden anhand von Bestrahlungsdauer-abhängigen Serien von Kohlenstoff- und Sauerstoffspektren charakterisiert. Durch Variation der Anregungsenergie und Emissionsgeometrie wurden atom- und symmetriespezifische Kohlenstoffspektren mit vernachlässigbarem Strahlenschaden gewonnen. Diese erlauben die Unterscheidung von elektronischen Zuständen mit σ- und π-Symmetrie. Eine Dichtefunktionaltheorie-Rechnung stimmt bemerkenswert gut mit den Energiepositionen der spektralen Signaturen überein. Darüberhinaus passen die spektralen σ- und π-Anteile zu den Symmetrien der berechneten Orbitale an den jeweiligen Energiepositionen.

Um den zweiten Aspekt organischer Moleküle, nämlich ihre Rolle in biologischen Systemen zu beleuchten, war es zunächst notwendig, die elektronische Struktur und Protonendynamik von flüssigem Wasser zu studieren, das bekanntermaßen das Medium vieler chemischer und biochemischer Reaktionen darstellt. Zu diesem Zweck wurde eine vollständige RIXS-Karte der Sauerstoff K Kante aufgenommen und im Detail analysiert. Ein temperaturabhängiger Vergleich mit XAS and RIXS Daten von Deuteriumoxid (schwerem Wasser), Natriumhydroxid und Natriumdeuteroxid erlaubt die Schlussfolgerung, dass ultra-schnelle Dissoziation auf der Zeitskala der Sauerstoff *1s* Rumpflochlebensdauer in flüssigem Wasser stattfindet, die zu einer charakteristischen spektralen Signatur in den RIXS Spektren führt. Diese Dissoziation wird gefördert durch intakte Wasserstoffbrückenbindungen mit benachbarten Wassermolekülen. Damit hängt die Dissoziationsrate direkt von der Ausgangskonfiguration der Wasserstoffbrückenbindungen ab.

Im nächsten Schritt in Richtung biologisch relevanter Systeme wurde die Stickstoffkante der Aminosäuren Glyzin und Histidin sowohl in Pulverform als auch in wässriger Lösung untersucht. Röntgenabsorptions- und -emissionsspektren der

wässrigen Lösungen wurden bei pH-Werten von 6 und im Falle des Glyzins auch bei pH 12 analysiert und mit den Pulverspektren verglichen. Ein pH-Wert von 12 führt zur Deprotonierung der Aminogruppe, was zu signifikanten Änderungen in der spektralen Signatur der Stickstoffspektren führt.

Die Ergebnisse dieser vier Beispiele demonstrieren, dass eine Vielfalt neuartiger Information gewonnen werden kann durch die Anwendung der neuen experimentellen Werkzeuge, die in dieser Arbeit entwickelt wurden, nämlich eines hochempfindlichen Röntgenspektrometers und einer Durchflussnasszelle.

How to design a Hettrick-Underwood spectrometer

This Chapter serves two purposes: on the one hand, it describes the procedure how the optimum parameters have been found for the spectrometer developed in this work (as described in Section 3.1), and on the other hand, it serves as a working instruction for how to find the optimum parameters for future instruments with different energy ranges, source spot sizes, etc. The goal of the optimization is to meet the desired energy resolution with well-balanced resolution limits (spot size, aberrations, and detector pixel size), while maximizing the throughput of the instrument.

The diffraction grating demagnifies/magnifies the source spot when using inner/outer orders, respectively. Hence, realistic source spot sizes are only tolerable when using inner (positive) diffraction orders. Therefore, the optimization procedure does not consider the use of outer (negative) orders. A quantitative analysis of this aspect can be found in [92].

Before starting the design of a spectrometer, it is essential to develop a set of requirements the spectrometer design aims for. The following information is necessary to optimize the design parameters:

- The photon energies the spectrometer will be used for determine the included angle φ on mirror and grating facets to ensure sufficient reflectivity.

- The characteristic photon energy E_{opt} the spectrometer will be optimized for. For best results, this energy should be the harmonic mean of all photon energies of interest, reduced to the 1st order. This step requires well-chosen diffraction orders for the individual photon energies, as detailed below.

- The resolving power $E/\Delta E$ the spectrometer is aiming for.

- The vertical source spot size s.

- The pixel size p of the used detector.

- The distance r_1 between the source and the center of the first optical element (i.e., the spherical mirror) as defined in Fig. 3.2 (page 29). This distance should be chosen as short as possible in order to realize the maximum acceptance angle in non-dispersive direction. In practice, the minimum distance is determined by mechanical boundary conditions like the size of the analysis chamber.

Especially if the spectrometer is intended for a wide energy range, special attention should be given to the second step: the spectrometer performance in both throughput and energy resolution is tremendously improved by the use of suitable diffraction orders for different photon energies, such that the wide energy range is translated to a small exit angle range. Using the example of the present instrument, the four energies of interest are 150 eV (sulfur, 1st order), 280 eV (carbon, 2nd order), 390 eV (nitrogen, 2nd order), and 525 eV (oxygen, 3rd order), an energy range which could not be covered by a single VLS grating if all emission lines were detected in 1st diffraction order. However, by using the given diffraction orders, these energies are converted to 150, 140, 195, and 175 eV when reduced to the first order, and their harmonic mean is 162 eV. With this trick, all emission lines were brought close together in a narrow exit angle range while avoiding overlapping spectra. In consequence, the throughput is excellent due to the always close to perfect blaze angle, and the imaging aberrations are low because the VLS parameters can always largely cancel the spherical aberrations introduced by the mirror. Furthermore, all emission spectra fit on the detector area "in one shot". Care has to be taken, that the different emission spectra do not overlap when investigating samples containing many different chemical elements.

A.1 Optimizing the included angle

A sufficiently high reflectivity in the soft x-ray range can only be achieved for grazing incidence. The reason is the high absorption in this photon energy range. Since for these energies, the index of refraction in matter is smaller than 1, the phenomenon of total reflection can (and has to) be exploited. But the higher the photon energy, the more grazing (higher) the included angle $\varphi = \alpha + \beta$ (all three defined in Fig. 3.2 on page 29) needs to be in order to achieve a high reflectivity. For a given photon energy, coating material, and surface roughness, reflectivities $\mathcal{R}(\varphi)$ can be calculated as a function of φ with freely available software. One possibility is
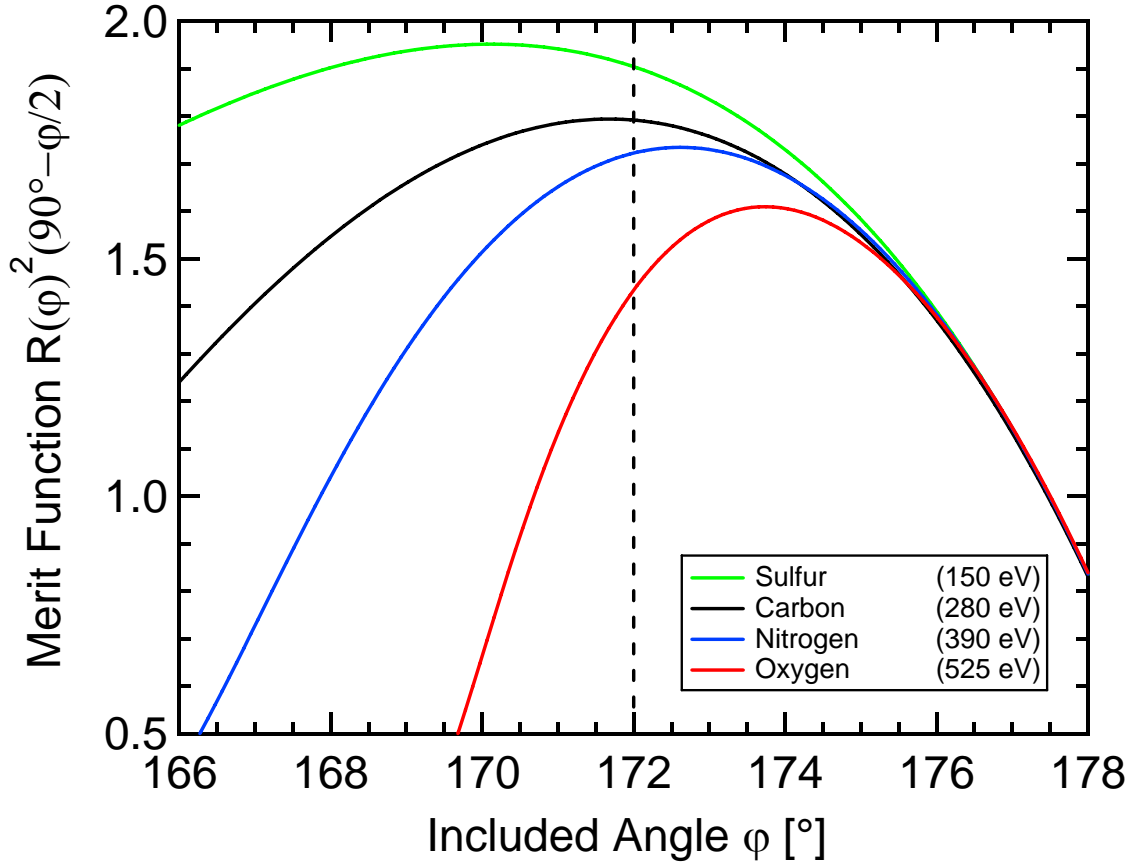
Figure A.1: The merit function $\mathcal{M}(\varphi)$ for photon energies of 150, 280, 390, and 525 eV. Surface conditions for the calculation: Nickel, micro roughness of 10 Å, calculated with [265].

to use the online tools of the Center for X-ray Optics (CXRO), Lawrence Berkeley National Laboratory [265]. Note that usually, the parameter is not the included angle φ chosen here, but rather the grazing incidence angle $90° - \varphi/2$.

For maximizing the throughput, the merit function $\mathcal{M}(\varphi)$ defined as:

$$\mathcal{M}(\varphi) = (90° - \varphi/2) \cdot \mathcal{R}^2(\varphi) \tag{A.1}$$

needs to be maximized. $\mathcal{R}(\varphi)$ is squared because the photons undergo two reflections (at mirror and grating). The factor $(90° - \varphi/2)$ takes into account, that for a given mirror and grating length, the acceptance angle in energy dispersive direction (and consequently, the throughput) is linear to $\sin(90° - \varphi/2) \approx (90° - \varphi/2)$. The approximation is valid for grazing included angles φ close to 180°.

Fig. A.1 shows the merit function for the four photon energies the present spectrometer was optimized for. The chosen φ of 172° (dashed line) leads only to an

11% loss for 525 eV and a 2.5% loss for 150 eV while being optimal for 280 and 390 eV and hence constitutes a good compromise.

The resulting included angle is then chosen for the center photon energy E_{opt}.

A.2 Optimizing the grating line density

After the optimum value for φ considering all photon energies of interest has been found, the next step is to find a suitable grating line density n meeting the design goal for the resolving power. This has a high impact on both throughput and resolution. In general, the higher the line density, the higher is also the achievable resolving power, but since for a given included angle φ, the incidence angle α on the grating increases (i.e., gets more grazing) with increasing line density, the acceptance angle goes down rapidly. In addition, with increasing line density, it becomes increasingly difficult to manufacture the grating with a high surface quality, leading to an overall drop in performance. Therefore, the design goal for the resolving power should be chosen carefully.

As already discussed in conjunction with Fig. 3.3 on page 31, three factors limit the overall resolving power: spot size, aberrations, and detector pixel size. The spot size limited resolving power is best suited to find the optimum line density, since its final form (equation A.6), which will be derived in the following paragraphs, is independent from other design parameters, in particular from r_3.

The central equation describing the energy dispersion of the grating is the so-called grating equation:

$$\sin(\alpha) - \sin(\beta) = n \cdot m \cdot \frac{hc}{eE} \tag{A.2}$$

where α and β are the grating incidence and exit angle, respectively (see Fig. 3.2), n is the line density to be optimized, m is the diffraction order, h is the Heisenberg constant, c is the speed of light, e is the elementary charge, and E is the photon energy.

Solving the grating equation for β and taking the derivative with respect to E yields an expression for the angular dispersion $\frac{\mathrm{d}\beta}{\mathrm{d}E}$ of the grating:

$$\frac{\mathrm{d}\beta}{\mathrm{d}E} = \frac{c \cdot h \cdot m \cdot n}{e \cdot E^2 \cdot \cos\beta}. \tag{A.3}$$

This equation by itself does not suffice to optimize the line density n. In addition, one must consider the vertical dimension s of the source spot and find an expression for the source-size limited resolving power. To accomplish this, the magnification of mirror and grating have to be calculated. While the mirror naturally has an angular
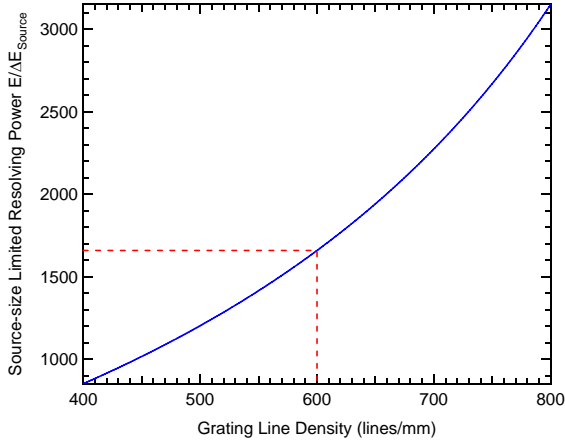
Figure A.2: The source-size limited resolving power as a function of the grating line density n plotted for the present spectrometer. The chosen line density of 600 lines/mm is marked by the red dashed line.

magnification of 1 (incidence angle equals reflected angle), that of the grating is $\frac{\mathrm{d}\beta}{\mathrm{d}\alpha} = \frac{\cos\alpha}{\cos\beta}$. The total magnification M with the arm lengths r_1, r_2, and r_3 (according to Fig. 3.2) is therefore given by:

$$M = \frac{r_2 + r_3\frac{\cos\alpha}{\cos\beta}}{r_1} \approx \frac{r_3\cos\alpha}{r_1\cos\beta}. \tag{A.4}$$

In the second step, M was approximated by neglecting the distance between mirror and grating r_2, which should anyway be kept as short as mechanically possible for the sake of a high acceptance angle in non-dispersive direction.

The sought source-size limited resolving power is then given by:

$$\frac{E}{\Delta E_{\mathrm{source}}} = \frac{E \cdot \frac{\mathrm{d}\beta}{\mathrm{d}E} \cdot r_3}{s \cdot M} = \frac{E \cdot \frac{\mathrm{d}\beta}{\mathrm{d}E} \cdot r_1 \cdot \cos\beta}{s \cdot \cos\alpha}. \tag{A.5}$$

Inserting equation A.3 and expressing α by $\arcsin\frac{nmhc}{2eE\cos(\varphi/2)} + \varphi/2$, as derived from the grating equation and the relationship $\varphi = \alpha + \beta$ yields a source-size limited resolving power of:

$$\frac{E}{\Delta E_{\mathrm{source}}} = \frac{\frac{c \cdot h \cdot m \cdot n}{e \cdot E} \cdot r_1}{s \cdot \cos(\arcsin\frac{nmhc}{2eE\cos(\varphi/2)} + \varphi/2)}. \tag{A.6}$$

With this equation, $\frac{E}{\Delta E_{\mathrm{source}}}$ can be plotted as a function of the line density n and from this plot, n can be chosen according to the desired resolving power. For this plot, the photon energy E should be chosen to be representative for the future use of the spectrometer. A good compromise is usually E_{opt}, the harmonic mean of all photon energies to be studied with the instrument, reduced to the 1st order. Fig. A.2 shows the plot for the present instrument with $E_{\mathrm{opt}} = 162$ eV. The source size s was assumed to be 30 microns, φ is 172°, and r_1 is 400 mm.

A.3 Optimizing the exit arm length r_3

Now, the pixel-limited resolving power can be matched to the design goal by choosing an appropriate distance between grating and detector r_3. The pixel-limit is closely connected with the angular dispersion (equation A.3). Considering the pixel-size p in energy-dispersive direction, the pixel-limited resolving power is:

$$\frac{E}{\Delta E_{\text{pixel}}} = \frac{E \cdot \frac{\mathrm{d}\beta}{\mathrm{d}E} \cdot r_3}{p} \tag{A.7}$$

After inserting the line density n and E_{opt} determined before, the equation can be solved for r_3. r_3 should be chosen such that the pixel-limited resolving power is about 3 to 4 times higher than the source-limit in order to avoid undersampling artifacts for extremely narrow features. For a more detailed discussion of this aspect, please refer to Section 3.1.

A.4 Finding the right radius of curvature for the spherical mirror

For calibration purposes (see Appendix B), it is very helpful to have the 0th diffraction order focused on the detector. At least for the present spectrometer, no gain in performance could be achieved by moving the 0th order out of focus. Since in 0th order, the grating does not contribute to the focussing, it is sufficient to consider the focus condition for a spherical concave mirror at an included angle φ with entrance arm length r_1 and exit arm $r_2 + r_3$ and solve it for the radius of curvature R:

$$R = \frac{2r_1(r_2 + r_3)}{\cos(\varphi/2)(r_1 + r_2 + r_3)} \tag{A.8}$$

In the present case, R is calculated to 8.41031 m.

A.5 Optimizing the grating blaze angle

For a high efficiency, it is important to use a blazed grating. The highest efficiency boost is given, if the incidence angle on the blaze facets is equal to the exit angle
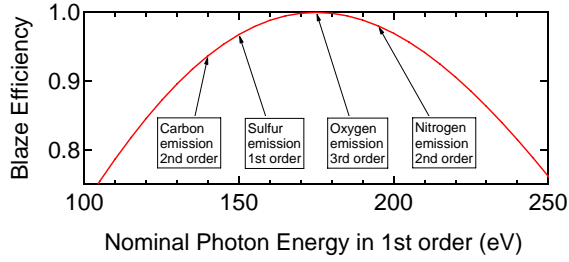
Figure A.3: The blaze efficiency resulting from a blaze angle of 1.79° (optimized for oxygen K emission) as a function of the photon energy.

relative to the facets. This condition yields for the blaze angle γ:

$$\gamma = \frac{\alpha - \beta}{2} \tag{A.9}$$

α and β can be calculated from the grating equation for any photon energy (and order). Normally, this should be the design energy E_{opt}. For the present spectrometer, the photon energy of 525 eV in 3rd order (effectively 175 eV) was chosen for the blaze angle optimization, yielding a blaze angle of 1.79°. The resulting blaze efficiency as a function of the photon energy is shown in Fig. A.3. This plot also shows the advantage of using the selected diffraction orders. It brings the emission lines close together, leading to a high blaze efficiency above 90% for all photon energies of interest.

A.6 Optimizing the VLS grating parameters

The line density in the grating center was already chosen in Section A.2. Optimizing the VLS parameters means to modulate the line density of the grating along its surface by a polynomial function such, that the spherical aberrations of the mirror are canceled as well as possible for the set of interesting photon energies in their respective diffraction orders. The polynomial coefficients are called VLS parameters. Two optimization approaches are possible: 1. The local line density is chosen such that a stigmatic (aberration-free) image results for the central photon energy E_{opt}. 2. The local line density is optimized for all photon energies of interest simultaneously. Both approaches require ray tracing.

For the present spectrometer, the latter (and more complex) approach was chosen. Since no freely available ray tracing software is capable of optimizing several energies simultaneously, a novel analytic ray tracing algorithm based on the symbolic math software Mathematica® was developed. Ray tracing means, that the propagation of rays emanating from the source spot within the accepted solid angle of the instrument is calculated.

For conventional numeric ray tracing programs, this is done in a sequential way: First, a ray leaving the source in a random direction is defined. Second, the interception point and incidence angle on the spherical mirror is calculated. Third, the new direction of the ray after reflection on the mirror is determined. Fourth, the interception point and incidence angle on the grating is computed. At this point, the software can compute the exit angle on the grating, which would lead to a stigmatic image, i.e., the exit angle which would allow the ray to end up on the optical axis (which is the position of the central ray) on the detector. With the information on the incidence angle, interception point, exit angle, and photon energy to optimize the VLS parameters for, it simply requires the grating equation to compute the "right" line density for this point on the grating. Of course, this only works for a single photon energy. Performing this numeric computation for a sufficient number of rays yields the sampling points of line densities on the surface required to define the polynomial. The higher the order of the polynomial (and thus, the higher the number of calculated VLS parameters), the higher is the number of required calculated rays.

For the novel analytic approach, all required quantities (i.e., incidence angle and interception point on the grating, exit angle, and interception point on the detector) are computed as symbolic functions of all relevant design parameters (i.e., photon energy, VLS parameters, mirror radius, distances r_1, r_2, and r_3, tilt angles of mirror, grating, and detector). By applying the grating equation, it is then straightforward to give the optimum line density variation on the grating as a function of the position on the grating for any photon energy. This analytic function can then be expanded in a Taylor series of arbitrary order, delivering the optimal VLS parameter set for a given photon energy in one shot.

Even more powerful is the possibility to derive a quantitative measure Q for the overall imaging aberrations of a whole set of photon energies and diffraction orders as an analytic function of all relevant design parameters. Q is defined as the sum of the squares of the imaging aberrations of 8 equidistant rays for each of the four photon energies of interest. Figure A.4 visualizes the definition of Q using the example of the already optimized imaging aberrations. For each emission line (N, O, S, C) as well as for their harmonic mean (162 eV), the distance from the central ray (optical axis) on the detector in dispersive direction is plotted as a function of the angular deviation from the optical axis. Ideally (i.e., without imaging aberrations), this deviation would be zero for all deviation angles within the accepted solid angle of the spectrometer. For the optimized VLS parameters, this ideal case is realized for the harmonic mean (black dotted line). The 8 deviation angles of the equidistant rays are given as dashed vertical lines. At these angles, the imaging aberrations of all 4 emission lines are marked with filled circles and Q is the sum of the 32 squares of these marked points.
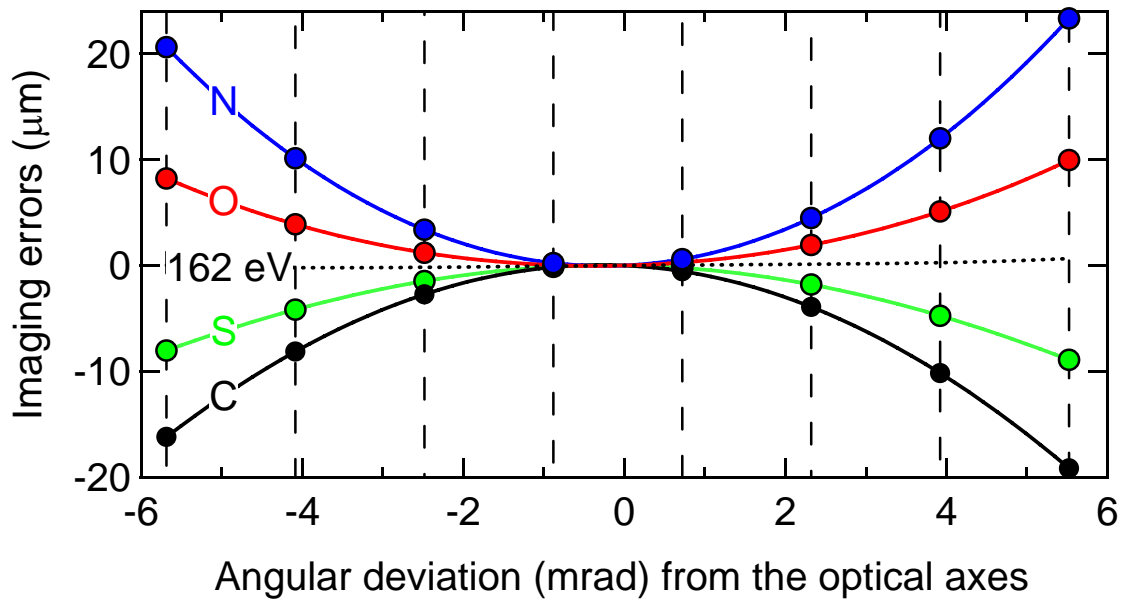
Figure A.4: The imaging aberrations for the four emission lines (N, O, S, C) as well as for their harmonic mean (162 eV) is plotted as a function of the angular deviation from the optical axis. The x-axis extends over the whole acceptance angle in dispersive direction. The angular deviations of 8 equidistant rays covering this acceptance angle are marked by dashed vertical lines. The imaging aberrations of the four emission lines at all of these angles are marked by filled circles. These are the values the quantitative measure Q for the overall imaging aberrations is composed of.

With this analytic form of Q, it is possible to optimize arbitrary sets of design parameters including VLS parameters, mirror radius, distances r_1, r_2, and r_3, and tilt angles of mirror, grating, and detector. This optimization is in fact a minimization algorithm for Q. For this minimization it is of great value, that since Q is given in closed analytical form, also symbolic derivatives of Q with respect to all design parameters (the elements of the "Jacobian matrix") are available in Mathematica. With this information, a minimization algorithm based on Newton's method can be applied, which quickly converges reliably even in a high-dimensional parameter space, allowing to optimize a large set of parameters simultaneously. In practice, the limits of this minimization algorithm were never reached during the optimization of the present spectrometer. A full optimization of all free design parameters revealed in a very early design stage, that introducing additional tilt angles on the optical elements, especially the detector, does not significantly improve the performance of the instrument. The same is true for changing the mirror radius or arm lengths such that the 0th diffraction order is no longer in focus.

The VLS parameters found by the symbolic ray tracing algorithm are given in table 3.1 on page 30.

SPECTROMETER ALIGNMENT PROCEDURE

This Chapter describes the proper alignment of the optical elements of the newly designed spectrometer introduced in Section 3.1 as developed during this work. The proper alignment is very important for achieving a good performance, especially a good energy resolution, and hence must be documented for future users.

The top of Fig. B.1 illustrates the function of the knobs adjusting the optics, while at the bottom, the optical path is illustrated with the same color code for the optics. In addition to these knobs, there are two more settings to be adjusted: the vertical detector position and the alignment of the spectrometer as a whole relative to the source. The latter is the most important and difficult alignment with the purpose to get the optical axis (defined by the central ray from the source to the center of the mirror as indicated by the black line at the bottom of Fig. B.1) centered on the grating. This adjustment is done by turning the vertical threaded struts supporting the spectrometer, thereby tilting it with respect to the laboratory coordinate system. In the spectrometer system, this adjustment effectively defines the vertical position of the source. It is sufficient to either adjust the front or the back struts. Which one to turn is merely a question of the bellows between the analysis chamber and the spectrometer, since for the optical alignment, it does not matter whether to move the front struts up or the back struts down and vice versa. In the following, this adjustment will be referred to as 'spectrometer tilt'.

The alignment is perfect if the following conditions are met:

1. The source is 400±5 mm away from the mirror center (278.4±5 mm from the flange of the spectrometer valve).

2. The optical axis is centered on the grating.

3. The zero order is in focus, i.e., the incidence angle $\varphi/2$ on the mirror is correct.
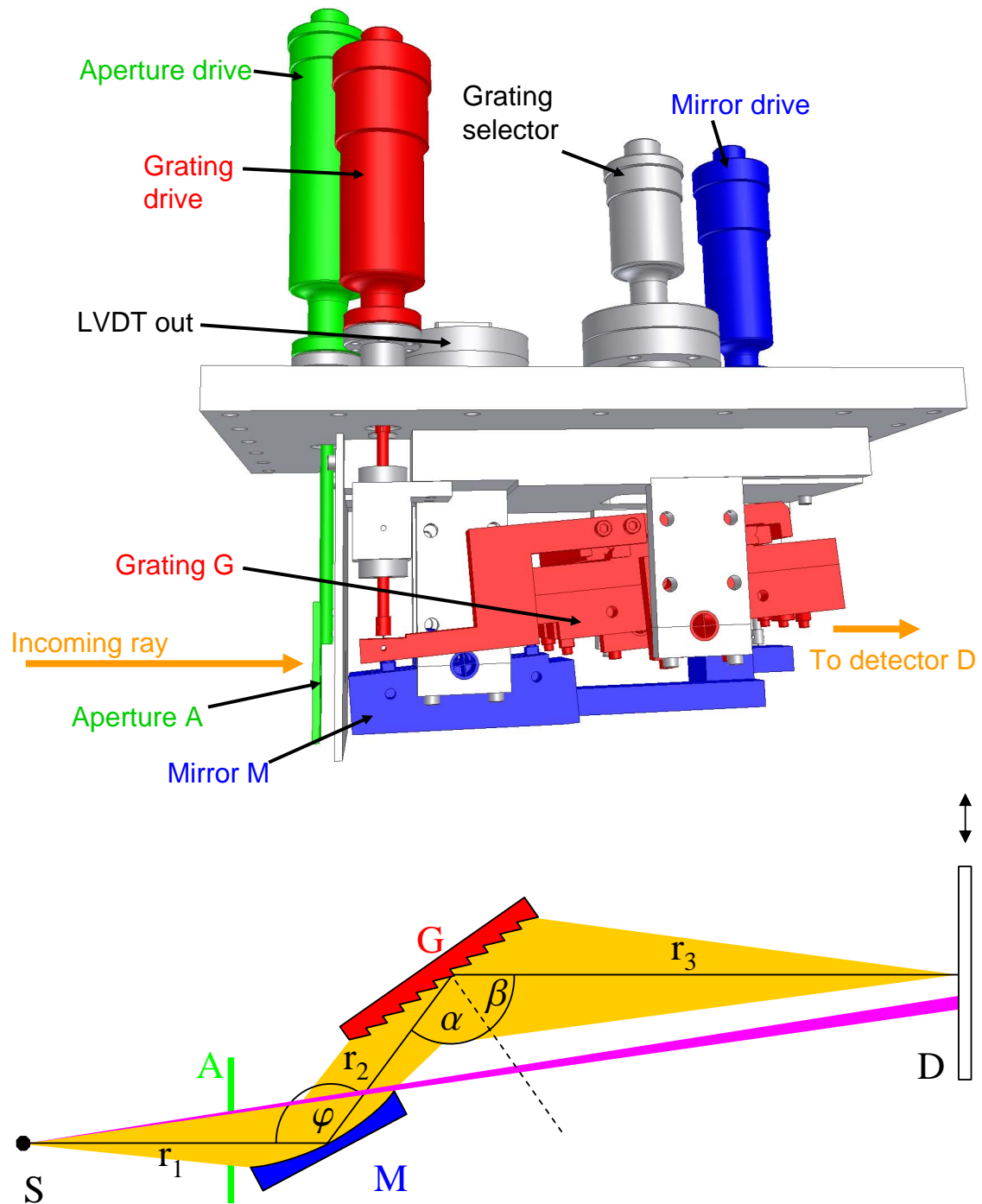
Figure B.1: The spectrometer mechanics (top) and its optical path (bottom) with the same color code for the optics **A** (aperture), **M** (mirror), **G** (grating), and **D** (detector). The pink beam represents direct light passing mirror and grating due to the too far open aperture **A**.

4. The first order of 162 eV is in focus, i.e., the grating incidence angle α is correct).

5. The whole mirror is illuminated while the direct (not reflected) light (pink beam in Fig. B.1) is blocked by the Aperture A.

6. The image spreads over the whole CCD in non-dispersive direction, i.e. the spectrometer is aligned symmetrically to the source in horizontal direction.

7. Only applicable for an elongated source spot: the source spot has to be aligned parallel to the optical elements of the spectrometer

The main difficulty is the fact that conditions 2. and 3. are interdependent. It is relatively easy to adjust the spectrometer tilt and the mirror angle such that the zero order is focused on the detector. But doing so, one will not necessarily hit the center of the grating with the center ray (defining the optical axis) on the mirror. This is especially crucial for VLS gratings since their line density varies along the grating surface. Therefore it is necessary to follow an iterative approach: after centering the optical axis on the grating, the zero order has to be focussed. Then the ray needs to be centered on the grating again, which will partly cancel the focal adjustment. Hence, the iteration loop has to start over until both conditions are met satisfactorily.

Grating and mirror are equipped with LVDTs (Linear Variable Differential Transformers), which output a reliable and reproducible voltage linear to the tilt angle. After the spectrometer has been calibrated, there are a few important numbers to keep in a save place, which make a later readjustment simple. These numbers are:

- The detector position ± 10 microns (mechanical scale)

- The voltage of the mirror LVDT

- The voltage of the grating LVDT for zero order mode

- The pixel position of the zero order light in zero order mode

- The voltage of the grating LVDT in normal operation mode

Once these numbers are known, it is fairly easy to move the source to the right distance and to adjust the spectrometer tilt such that the zero order light in zero order mode shows up at the right pixel position. After checking the knife edge position blocking the direct light (condition 5) and adjusting the spectrometer tilt in the non-dispersive direction such that condition 6 is fulfilled, the alignment should be restored.

Finding the above-mentioned numbers is a complex task, since not only the angles of mirror and grating have to be adjusted, but also the tilt angle of the whole spectrometer with respect to the vacuum chamber has to be right to ensure a proper source spot position with respect to the mirror. Even a high-precision mechanical calibration of the mirror and grating angles is not sufficient to guarantee a good adjustment, since the mirror radius could easily be off by several percent, requiring an individual in-situ correction (i.e. with x-rays) of both mirror and spectrometer angle. Still, a mechanical angle calibration, which is typically done on a granite bench with a water-level, is valuable for finding a good starting point for the in-situ optimization, namely an angle of $\approx 4°$ of mirror and grating relative to the spectrometer base.

The initial adjustment procedure consists of the following steps:

1. bring source to the right distance

2. tilt mirror and grating $\approx 4°$ to base

3. position the detector close to the lower hard stop or at the last known measurement position

4. prepare synchrotron, sample, and software

5. find mirror center (zero order)

6. find grating center (zero order)

7. overcompensate defocus in the mirror center (zero order)

8. iterate steps 5–7 until zero order is in focus

9. find grating angle which brings the 1st order in focus

10. set aperture knife edge to block direct light

11. align optical axis parallel to the synchrotron plane

12. align spectrometer in non-dispersive direction

13. check detector rotation and setting in the software

14. calibrate the energy scale

In this Chapter, the quite complex steps 4–11 and 14 will be explained in detail.

B.1 Step 4: Preparing synchrotron, sample and software

In zero order, which is used for the mirror alignment (steps 5–8), the grating does not demagnify the image. Therefore, the vertical size of the source has to be as small as possible (max. 15 microns). In case the horizontal dimension of the synchrotron spot is significantly higher (in this case it is more appropriate to speak of a 'source line' instead of a 'source spot'), it is also important to check that the source line is aligned parallel to the optical elements of the spectrometer. Otherwise, the spectrometer 'sees' a vertical spot size which is enlarged by the horizontal spot length multiplied by the sine of the misalignment angle due to the absence of an entrance slit.

Since in zero order the photon energy does not matter, it is favorable to go for a high intensity at the cost of energy resolution. In contrast, for the first order alignment (step 9), the photon energy should be between 157 and 167 eV, with a full width at half maximum (FWHM) of not more than 0.1 eV, which corresponds to a resolving power of ≈ 1600 or a dispersion of 2 pixels FWHM on the detector.

For calibration purposes in first order, a high-intensity Rayleigh line of about 162 eV is required. Therefore the sample should have a high elastic reflectivity at 162 eV. A good candidate is, e.g., a cadmium sulfide single crystal oriented in mirror reflection geometry (incidence angle = exit angle), since it possesses unoccupied states excitable at 162 eV. In principle, any sample material which does not emit too much visible light can also be used, at the cost of intensity and consequently longer adjustment duration.

For preparing the data acquisition software, it is essential to check the slope setting of the linear curvature, which has to match the mechanical detector alignment. Otherwise, all measured peaks are artificially broadened.

B.2 Step 5: Finding the mirror center

A movable aperture with a knife edge to block the light passing the mirror and several discrete slits of varying widths to mask the mirror illumination is installed directly in front of the mirror (green element in Figure B.1). A detailed picture of the aperture is given in Fig. B.2. For steps 5–9, the smallest of the slits is used to limit the illumination of the mirror to a small stripe. When driving this aperture up and down, this stripe moves across the mirror. Along the way, the imaging aberrations of the system can be watched on the CCD image. In order to interpret them correctly, it is helpful to simulate the aberrations with a special ray tracing
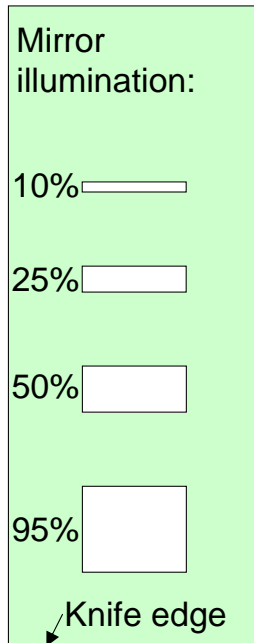
Figure B.2: Sketch of the aperture defining the mirror illumination (green element in Fig. B.1). The knife edge is used to block the direct light (pink beam in the bottom of Fig. B.1) at a mirror illumination of 100%. This is the normal operation mode. The 95% slit can be used to block light hitting the front of the mirror holder in the case this causes stray light on the detector. The smallest slit with 10% illumination is used for the adjustment procedure described in this Chapter.

software which was written in IGOR®. This software allows to plot the imaging aberrations of the spectrometer, i.e. the channel number on the CCD as a function of the illuminated spot on the mirror, for every conceivable tilt of the optical elements and for arbitrary diffraction orders and photon energies. The interesting information is not the absolute line position on the detector, since the CCD position could easily be off by many channels, but rather the relative movement on the detector due to the motion of the photon beam along the mirror. Since it is very important to always make sure that the optical axis is centered on the grating, it is often necessary to determine the slit position which illuminates the center of the mirror (and thereby defines the optical axis) during the alignment procedure and is hence described in advance.

The center of the mirror has to be found in zero order, because only then the grating is 'long enough' to reflect light from the whole mirror length towards the detector in order to find the edges of the mirror. Once the illuminated areas on mirror and grating are roughly centered, the mirror length is limiting the light path on both ends in zero order. To accomplish this, the zero order intensity on the detector has to be maximized by tilting the spectrometer with the vertical struts, while mirror and grating are tilted $\approx 4°$ relative to the spectrometer base plate. During this, the aperture knife edge always has to be kept in a position which blocks the direct light but still illuminates the mirror fully.

After this rough centering of the mirror light on the grating, we will now use the aperture for fine-tuning. With the smallest aperture slit moved in, we have to find

the slit positions where the line on the detector just vanishes due to slipping off the mirror or the grating. After placing the slit there, the grating must be tilted towards the mirror. If then the line reappears, the grating length was limiting on this side. In this case the whole spectrometer has to be tilted in order to bring the footprint on the grating closer to its center. If the line does not reappear due to tilting the grating, the desired slit position has been found for this edge of the mirror. The same procedure must be repeated for the opposite end of the mirror. The mean value of these two positions finally gives the slit position which illuminates the mirror center. This will be referred to as 'center slit position' hereafter. It depends slightly on the spectrometer tilt, hence it has to be redetermined after each iteration. Exclusively changing the mirror angle does not affect the center slit position.

B.3 Step 6: Finding the grating center

In the center slit position, the mirror should reflect the ray right towards the grating center. This has to be checked by turning the grating drive clockwise. As the grating turns to more and more grazing angles, the zero order shifts up on the detector while higher orders enter the detector from below. Follow the second order with the detector until it vanishes due to slipping off the grating. Then adjust the mirror angle to bring the signal back. Find the mirror angle that keeps the second order visible for the most extreme grazing grating angles. For the next step, tilt the grating back to 4° and move the zero order roughly to channel 1024 by moving the detector back down.

B.4 Step 7: Overcompensation of the zero order defocus

Since in zero order the grating acts like a plane mirror, the focus is only determined by the incidence angle on the spherical mirror, which varies upon changing the spectrometer tilt or the mirror angle. Even a perfectly focussed zero order is still about 30 pixels (400 microns!) wide on the CCD due to the not corrected higher order imaging aberrations of the mirror. This image width is quite insensitive to the focus condition and therefore not suitable for determining whether the spectrometer is in focus or not. One rather has to use the manifestation of the defocus term as a slope in the imaging aberrations at the center of the mirror. The mirror is in focus, if the line position on the detector gets extremal when the slit passes this center slit position. In practice, instead of evaluating the slope in the mirror center, it

is easier to compare the line position on the detector at both ends of the mirror. If the zero order is in focus, the emission line should appear at roughly the same position for both ends of the mirror. This situation can be achieved by adjusting the spectrometer tilt (vertical struts) and subsequently checking the focus condition repeatedly. For a quick convergence of the iterative adjustment approach, it is not sufficient to tilt the spectrometer to the perfect focus condition, but rather to overcompensate, i.e. to tilt the spectrometer twice as far. Since the spectrometer tilt has no scale, this can only be guessed. This overcompensation is necessary, since by tilting the spectrometer, the center ray moves out of the grating center, which has to be corrected by turning the mirror in the next iteration. This correction will exactly halve the effect the spectrometer tilt adjustment has on the incidence angle of the mirror. Continue the iteration in Section B.2 until no further improvement is possible.

B.5 Step 9: Adjusting the focus of the first order

Before trying to focus the first order, it is important to have finished the previous steps, i.e. the center ray needs to be centered on the grating and the zero order has to be in focus.

The first order focus should be adjusted with a photon energy between 157 and 167 eV and a beamline resolving power of at least 1600. At these energies, the imaging aberrations should be close to zero once the grating angle is correct.

First, with the aperture still at the center slit position, adjust the detector such that the zero order appears at channel 1024. Turn the grating drive clockwise until the first order shows up at channel 1024. Record the first order peak in order to have a reference peak width. Then move the aperture out until it barely blocks the direct light, illuminating the whole mirror. Tilt the grating until the first order peak is as narrow as possible. It should now be almost as sharp as the reference peak. To further quantify the focal properties, it is useful to put the narrowest aperture slit back in and watch the motion of the peak on the detector while moving across the mirror. The motion should not exceed one pixel width.

B.6 Step 10: Set aperture knife edge to block direct light

If the aperture is fully retracted, the direct light path is open. At the bottom of Fig. B.1, this path is shown in pink color. Since light following this path is neither

reflected at the mirror nor at the grating, it is very intense, forming a characteristic bright band on the detector image. The goal is to position the knife edge of the aperture in a way, that it just blocks the direct light while still allowing a full illumination of the mirror. In order to achieve this, the aperture has to be lowered until the direct light band just disappears completely. Then, in order to avoid spurious intensity from direct light, lower the aperture further by 0.6 mm. This distance is 0.1 mm less than the thickness of the mirror holder frame of 0.4 inch projected onto the aperture plane. Thus, in this position, the knife edge shades the mirror holder frame almost completely, avoiding reflections from there, while still allowing a full illumination of the mirror.

B.7 Step 11: Aligning the optical axis parallel to the synchrotron plane

Since an elongated synchrotron spot which is tilted with respect to the spectrometer optics dramatically decreases the achievable resolving power (compare the discussion at the beginning of Section B.1), it is important to ensure that the optical axis is aligned parallel to the synchrotron plane spanned by the synchrotron beam and the direction of its elongation. Thereby, it does not matter whether this elongation is intrinsic (i.e. the synchrotron by itself delivers an elongated spot) or is induced by the experimental geometry (e.g. grazing incidence or grazing emission geometry). The only way to ensure that the geometry reduces the resolving power under no circumstances, is to align the sample rotation axis (if there is one) perpendicular and the optical axis of the spectrometer parallel to the synchrotron plane.

The latter can be achieved by choosing an extremely grazing emission geometry and tilting the spectrometer with the vertical adjustment rods, such that the peak width on the CCD is minimized while maintaining the peak position on the CCD.

B.8 Step 14: Calibrating the energy scale

At this point, the energy resolution and the throughput are optimized. In order to get the energy scale right, we now need to adjust two parameters: the detector position which directly introduces a pixel offset, and the grating angle which influences the energy dispersion. While the first does not influence the adjustments made in the previous Chapter, the latter has already been adjusted for optimal energy resolution in Section B.5. Nevertheless, the grating angle has to be checked and fine-tuned for a good energy scale.

The central equation describing the energy dispersive diffraction of the grating, is the so-called grating equation (equation A.2 on page 92). Solving it for the photon energy E combined with the known incidence angle α, the exit arm length r_3, and the pixel size s yields an expression for E as a function of the diffraction order m and the pixel number $p = \frac{\beta \cdot r_3}{s} + p_0$ on the CCD:

$$E = \frac{n \cdot m \cdot h \cdot c}{e(\sin \alpha - \sin \frac{(p-p_0) \cdot s}{r_3})} = \frac{600 \frac{\text{lines}}{\text{mm}} \cdot m \cdot h \cdot c}{e(\sin(87.886°) - \sin \frac{(p+107721.28) \cdot 13.5 \mu\text{m}}{1\text{m}})} \tag{B.1}$$

The pixel offset p_0 was chosen such that the photon energy of 162 eV in first order is assigned to the center pixel 1024.

For fine-tuning the grating angle, it is favorable to use the nitrogen K edge, since the beamline can be easily calibrated with N_2 gas absorption, and the spectrometer is able record the second and third order around 400 eV simultaneously. The first vibrational resonance of N_2 appears at 400.88 eV [260], so we use this photon energy for calibration. At the right grating angle, the spread between the second and third order of a photon energy of 400.88 eV is 1339.5 channels. If the detected spread is smaller, turn the grating drive clockwise, and vice versa. It should be possible to correct the grating angle for the right energy spread without compromising the energy resolution.

Finally, the detector position needs to be adjusted by matching a known photon energy with the calculated energy scale. For example, the first nitrogen K resonance (400.88 eV) needs to appear at pixel 1689.0 (second order) and 349.5 (third order). This calibration procedure should provide an accurate energy scale over the whole detector range and for all orders, i.e. for photon energies between 130 and 650 eV.

BIBLIOGRAPHY

[1] G. Horowitz, "Organic thin film transistors: From theory to real devices", *J. Mater. Res.* **19**, 1946 (2004).

[2] H. Hoppe and N. S. Sariciftci, "Organic solar cells: An overview", *J. Mater. Res.* **19**, 1924 (2004).

[3] A. Dodabalapur, "Organic light emitting diodes", *Solid State Commun.* **102**, 259 (1997).

[4] V. Bulovic, P. E. Burrows, and S. R. Forrest, "Molecular organic light-emitting devices", *Electroluminescence I* **64**, 255 (2000).

[5] E. Umbach, "Characterization of organic overlayers on well-defined substrates", *Prog. Surf. Sci.* **35**, 113 (1990).

[6] J. Taborski, P. Vaterlein, H. Dietz, U. Zimmermann, and E. Umbach, "NEXAFS investigations on ordered adsorbate layers of large aromatic molecules", *J. Electron Spectrosc. Relat. Phenom.* **75**, 129 (1995).

[7] K. Glöckler, C. Seidel, A. Soukopp, M. Sokolowski, E. Umbach, M. Bohringer, R. Berndt, and W. D. Schneider, "Highly ordered structures and submolecular scanning tunnelling microscopy contrast of PTCDA and DM-PBDCI monolayers on Ag(111) and Ag(110)", *Surf. Sci.* **405**, 1 (1998).

[8] E. Umbach, K. Glöckler, and M. Sokolowski, "Surface "architecture" with large organic molecules: interface order and epitaxy", *Surf. Sci.* **404**, 20 (1998).

[9] V. Shklover, F. S. Tautz, R. Scholz, S. Sloboshanin, M. Sokolowski, J. A. Schaefer, and E. Umbach, "Differences in vibronic and electronic excitations of PTCDA on Ag(111) and Ag(110)", *Surf. Sci.* **454**, 60 (2000).

[10] F. S. Tautz, M. Eremtchenko, J. A. Schaefer, M. Sokolowski, V. Shklover, K. Glöckler, and E. Umbach, "A comparison of the chemisorption behaviour of PTCDA on different Ag surfaces", *Surf. Sci.* **502**, 176 (2002).

[11] L. Chkoda, M. Schneider, V. Shklover, L. Kilian, M. Sokolowski, C. Heske, and E. Umbach, "Temperature-dependent morphology and structure of ordered 3,4,9,10-perylene-tetracarboxylicacid-dianhydride (PTCDA) thin films on Ag(111)", *Chem. Phys. Lett.* **371**, 548 (2003).

[12] L. Kilian, E. Umbach, and M. Sokolowski, "Molecular beam epitaxy of organic films investigated by high resolution low energy electron diffraction (SPA-LEED): 3,4,9,10-perylenetetracarboxylicacid-dianhydride (PTCDA) on Ag(111)", *Surf. Sci.* **573**, 359 (2004).

[13] A. Schöll, Y. Zou, M. Jung, T. Schmidt, R. Fink, and E. Umbach, "Line shapes and satellites in high-resolution x-ray photoelectron spectra of large pi-conjugated organic molecules", *J. Chem. Phys.* **121**, 10260 (2004).

[14] A. Schöll, Y. Zou, D. Huebner, S. G. Urquhart, T. Schmidt, R. Fink, and E. Umbach, "A comparison of fine structures in high-resolution x-ray-absorption spectra of various condensed organic molecules", *J. Chem. Phys.* **123**, 044509 (2005).

[15] N. Dori, M. Menon, L. Kilian, M. Sokolowski, L. Kronik, and E. Umbach, "Valence electronic structure of gas-phase 3,4,9,10-perylene tetracarboxylic acid dianhydride: Experiment and theory", *Phys. Rev. B: Condens. Matter Mater. Phys.* **73**, 195208 (2006).

[16] Y. Zou, L. Kilian, A. Schöll, T. Schmidt, R. Fink, and E. Umbach, "Chemical bonding of PTCDA on Ag surfaces and the formation of interface states", *Surf. Sci.* **600**, 1240 (2006).

[17] F. S. Tautz, "Structure and bonding of large aromatic molecules on noble metal surfaces: The example of PTCDA", *Prog. Surf. Sci.* **82**, 479 (2007).

[18] M. G. Cacace, E. M. Landau, and J. J. Ramsden, "The Hofmeister series: salt and solvent effects on interfacial phenomena", *Q. Rev. Biophys.* **30**, 241 (1997).

[19] K. D. Collins and M. W. Washabaugh, "The Hofmeister effect and the behavior of water at interfaces", *Q. Rev. Biophys.* **18**, 323 (1985).

[20] B. Hille, *Ionic Channels of Excitable Membranes*, Sinauer, Sunderland, Massachusetts (1992).

[21] F. Bezanilla, "Ion Channels: From Conductance to Structure", *Neuron* **60**, 456 (2008).

[22] P. A. M. Dirac, "The Quantum Theory of the Emission and Absorption of Radiation", *Proceedings of the Royal Society of London. Series A* **114**, 243 (1927).

[23] D. W. Lindle and O. Hemmers, "Breakdown of the dipole approximation in soft-X-ray photoemission", *J. Electron Spectrosc. Relat. Phenom.* **100**, 297 (1999).

[24] D. P. Woodruff, "Non-dipole effects in high-energy photoelectron emission; identification and quantification using X-ray standing waves", *Nucl. Instrum. Methods Phys. Res., Sect. A* **547**, 187 (2005).

[25] O. Hemmers, R. Guillemin, and D. W. Lindle, "Nondipole effects in soft X-ray photoemission", *Radiat. Phys. Chem.* **70**, 123 (2004).

[26] K. Hosaka, J. Adachi, A. V. Golovin, M. Takahashi, T. Teramoto, N. Watanabe, T. Jahnke, T. Weber, M. Schoffler, L. Schmidt, T. Osipov, O. Jagutzki, A. L. Landers, M. H. Prior, H. Schmidt-Bocking, R. Dorner, A. Yagishita, S. K. Semenov, and N. A. Cherepkov, "Nondipole effects in the angular distribution of photoelectrons from the CK shell of the CO molecule", *Phys. Rev. A: At., Mol., Opt. Phys.* **73**, 022716 (2006).

[27] E. Fermi, *Nuclear Physics*, University of Chicago Press (1950).

[28] G. D. Mahan, "Final-state potential in x-ray spectra", *Phys. Rev. B: Condens. Matter Mater. Phys.* **21**, 1421 (1980).

[29] V. I. Grebennikov, Y. A. Babanov, and O. B. Sokolov, "Extra-atomic relaxation and x-ray-spectra of narrow-band metals: 1. formalism", *Physica Status Solidi B-Basic Research* **79**, 423 (1977).

[30] U. von Barth and G. Grossmann, "Dynamical effects in x-ray-spectra and the final-state rule", *Phys. Rev. B: Condens. Matter Mater. Phys.* **25**, 5150 (1982).

[31] J. Stöhr, *NEXAFS spectroscopy*, Springer, Berlin Heidelberg (1992).

[32] B. K. Teo, *EXAFS: basic principles and data analysis*, Springer-Verlag, Berlin (1986).

[33] Y. Zubavichus, Y. J. Yang, M. Zharnikov, O. Fuchs, T. Schmidt, C. Heske, E. Umbach, G. Tzvetkov, F. P. Netzer, and M. Grunze, "Local structure of amorphous ice as revealed by OK-edge EXAFS", *ChemPhysChem* **5**, 509 (2004).

[34] Y. Zubavichus, M. Zharnikov, Y. J. Yang, O. Fuchs, E. Umbach, C. Heske, and M. Grunze, "Oxygen K-edge X-ray absorption fine structure studies of vacuum-deposited ice films", *Langmuir* **22**, 7241 (2006).

[35] T. Attwood, *Soft X-rays and extreme ultraviolet radiation: principles*, Cambridge University Press (1999).

[36] M. O. Krause, "Atomic radiative and radiationless yields for K-shells and L-shells", *J. Phys. Chem. Ref. Data* **8**, 307 (1979).

[37] A. Nilsson, P. Bennich, T. Wiell, N. Wassdahl, N. Martensson, J. Nordgren, O. Bjorneholm, and J. Stöhr, "Direct probing of the adsorbate-substrate chemical-bond using angle-dependent x-ray-emission spectroscopy", *Phys. Rev. B: Condens. Matter Mater. Phys.* **51**, 10244 (1995).

[38] A. Nilsson, J. Hasselström, A. Föhlisch, O. Karis, L. G. M. Pettersson, M. Nyberg, and L. Triguero, "Probing chemical bonding in adsorbates using X-ray emission spectroscopy", *J. Electron Spectrosc. Relat. Phenom.* **110**, 15 (2000).

[39] A. Nilsson, "Applications of core level spectroscopy to adsorbates", *J. Electron Spectrosc. Relat. Phenom.* **126**, 3 (2002).

[40] F. de Groot, "High resolution x-ray emission and x-ray absorption spectroscopy", *Chem. Rev.* **101**, 1779 (2001).

[41] H. Kramers and W. Heisenberg, "Über die Streuung von Strahlung durch Atome", *Z. Phys. A* **31**, 681 (1925).

[42] Y. Ma, N. Wassdahl, P. Skytt, J. Guo, J. Nordgren, P. D. Johnson, J. E. Rubensson, T. Boske, W. Eberhardt, and S. D. Kevan, "Soft x-ray resonant inelastic-scattering at the C K edge of diamond", *Phys. Rev. Lett.* **69**, 2598 (1992).

[43] Y. J. Ma, "X-ray absorption, emission, and resonant inelastic scattering in solids", *Phys. Rev. B: Condens. Matter Mater. Phys.* **49**, 5799 (1994).

[44] V. Weisskopf and E. Wigner, "Berechnung der natürlichen Linienbreite auf Grund der Diracschen Lichttheorie", *Z. Phys. A* **63**, 54 (1930).

[45] J. J. Sakurai, *Advanced Quantum Mechanics*, Addison Wesley, Menlo Park, California (1967).

[46] T. A. Callcott, "Soft x-ray fluorescence spectroscopy", *Experimental Methods in the Physical Sciences* **32**, 279–300 (1998).

[47] T. X. Carroll, J. Hahne, T. D. Thomas, L. J. Saethre, N. Berrah, J. Bozek, and E. Kukk, "Carbon 1s core-hole lifetime in CO_2", *Phys. Rev. A: At., Mol., Opt. Phys.* **6104**, 042503 (2000).

[48] N. Saito, A. Hempelmann, F. Heiser, O. Hemmers, J. Viefhaus, and U. Becker, "Lifetime effects on the dissociation of core-excited N_2 and CO molecules", *Phys. Rev. A: At., Mol., Opt. Phys.* **6102**, 022709 (2000).

[49] A. P. Hitchcock and C. E. Brion, "K-shell excitation-spectra of CO, N_2 and O_2", *J. Electron Spectrosc. Relat. Phenom.* **18**, 1 (1980).

[50] F. Gel'mukhanov, H. Agren, M. Neeb, J. E. Rubensson, and A. Bringer, "Integral properties of channel interference in resonant X-ray scattering", *Phys. Lett. A* **211**, 101 (1996).

[51] M. O. Krause and J. H. Oliver, "Natural widths of atomic K-levels and L-levels, K-alpha x-ray-lines and several KLL auger lines", *J. Phys. Chem. Ref. Data* **8**, 329 (1979).

[52] K. Hämäläinen, D. P. Siddons, J. B. Hastings, and L. E. Berman, "Elimination of the inner-shell lifetime broadening in x-ray-absorption spectroscopy", *Phys. Rev. Lett.* **67**, 2850 (1991).

[53] J. Nordgren, P. Glans, K. Gunnelin, J. Guo, P. Skytt, C. Sathe, and N. Wassdahl, "Resonant soft X-ray fluorescence spectra of molecules", *Appl. Phys. A: Mater. Sci. Process.* **65**, 97 (1997).

[54] Y. J. Ma, "X-ray resonant inelastic scattering", *J. Electron Spectrosc. Relat. Phenom.* **79**, 131 (1996).

[55] S. Eisebitt and W. Eberhardt, "Band structure information and resonant inelastic soft X-ray scattering in broad band solids", *J. Electron Spectrosc. Relat. Phenom.* **110**, 335 (2000).

[56] J. E. Rubensson, "RIXS dynamics for beginners", *J. Electron Spectrosc. Relat. Phenom.* **110**, 135 (2000).

[57] T. Minami and K. Nasu, "Dissipation of core-hole momentum by phonons in soft-x-ray radiation processes from valence band to core level of wide-gap insulators", *Phys. Rev. B: Condens. Matter Mater. Phys.* **57**, 12084 (1998).

[58] O. Björneholm, S. Sundin, S. Svensson, R. R. T. Marinho, A. N. deBrito, F. Gel'mukhanov, and H. Agren, "Femtosecond dissociation of core-excited HCl monitored by frequency detuning", *Phys. Rev. Lett.* **79**, 3150 (1997).

[59] O. Björneholm, A. Nilsson, A. Sandell, B. Hernnas, and N. Martensson, "Determination of time scales for charge-transfer screening in physisorbed molecules", *Phys. Rev. Lett.* **68**, 1892 (1992).

[60] L. Weinhardt, O. Fuchs, A. Fleszar, M. Bär, M. Blum, M. Weigand, J. Denlinger, W. Yang, W. Hanke, E. Umbach, and C. Heske, "Resonant inelastic soft x-ray scattering of CdS: A two-dimensional electronic structure map approach", *Phys. Rev. B* **79**, 165305 (2009).

[61] O. Fuchs, M. Blum, M. Weigand, E. Umbach, L. Weinhardt, M. Bär, C. Heske, J. Denlinger, Y.-D. Chuang, W. McKinney, Z. Hussain, E. Gullikson, M. Jones, P. Batson, and R. Follath, "High-resolution, high-transmission soft x-ray spectrometer for the study of biological samples", *Rev. Sci. Instrum.* **80**, 063103 (2009).

[62] L. Weinhardt, O. Fuchs, M. Blum, M. Bär, M. Weigand, J. Denlinger, Y. Zubavichus, M. Zharnikov, M. Grunze, C. Heske, and E. Umbach, "Resonant x-ray emission spectroscopy of liquid water: novel instrumentation, high resolution, and the 'map' approach", *J. Electron. Spectrosc. Relat. Phenom., in print* , doi:10.1016/j.elspec.2009.02.014 (2009).

[63] J. H. Guo, P. Glans, P. Skytt, N. Wassdahl, J. Nordgren, Y. Luo, H. Agren, Y. Ma, T. Warwick, P. Heimann, E. Rotenberg, and J. D. Denlinger, "Resonant excitation x-ray-fluorescence from C_{60}", *Phys. Rev. B: Condens. Matter Mater. Phys.* **52**, 10681 (1995).

[64] R. Nakajima, J. Stöhr, and Y. U. Idzerda, "Electron-yield saturation effects in L-edge x-ray magnetic circular dichroism spectra of Fe, Co, and Ni", *Phys. Rev. B: Condens. Matter Mater. Phys.* **59**, 6421 (1999).

[65] T. J. Regan, H. Ohldag, C. Stamm, F. Nolting, J. Lüning, J. Stöhr, and R. L. White, "Chemical effects at metal/oxide interfaces studied by x-ray-absorption spectroscopy", *Phys. Rev. B: Condens. Matter Mater. Phys.* **6421**, 214422 (2001).

[66] S. Gota, M. Gautier-Soyer, and M. Sacchi, "Fe 2p absorption in magnetic oxides: Quantifying angular-dependent saturation effects", *Phys. Rev. B: Condens. Matter Mater. Phys.* **62**, 4187 (2000).

[67] B. T. Thole, G. van der Laan, J. C. Fuggle, G. A. Sawatzky, R. C. Karnatak, and J. M. Esteva, "3d x-ray absorption lines and the $3d^9 4f^{n+1}$ multiplets of the lanthanides", *Phys. Rev. B: Condens. Matter Mater. Phys.* **32**, 5107 (1985).

[68] H. C. Burger and P. H. van Cittert, "Verbreiterung von Spektrallinien durch Selbstabsorption", *Z. Phys. A* **51**, 638 (1928).

[69] D. Kondo, K. Sakamoto, H. Takeda, F. Matsui, K. Amemiya, T. Ohta, W. Uchida, and A. Kasuya, "Unoccupied molecular orbitals of C_{60} molecules adsorbed on Si(001)-(2 x 1) and Si(111)-(7 x 7) surfaces studied by NEXAFS", *Surf. Sci.* **514**, 337 (2002).

[70] B. M. Messer, C. D. Cappa, J. D. Smith, K. R. Wilson, M. K. Gilles, R. C. Cohen, and R. J. Saykally, "pH dependence of the electronic structure of glycine", *J. Phys. Chem. B* **109**, 5375 (2005).

[71] L. A. Näslund, J. Lüning, Y. Ufuktepe, H. Ogasawara, P. Wernet, U. Bergmann, L. G. M. Pettersson, and A. Nilsson, "X-ray absorption spectroscopy measurements of liquid water", *J. Phys. Chem. B* **109**, 13835 (2005).

[72] J. D. Denlinger, "Ultrahigh-vacuum (UHV) bendable refocus mirrors", *ALS Activity Report 2006* , 116 (2007).

[73] A. T. PLC, "Operating manual for CCD model DO-436", (2005).

[74] T. A. Callcott, K. L. Tsang, C. H. Zhang, D. L. Ederer, and E. T. Arakawa, "High-efficiency soft-x-ray emission spectrometer for use with synchrotron radiation excitation", *Rev. Sci. Instrum.* **57**, 2680 (1986).

[75] J. Nordgren, G. Bray, S. Cramm, R. Nyholm, J. E. Rubensson, and N. Wassdahl, "Soft-x-ray emission-spectroscopy using monochromatized synchrotron radiation", *Rev. Sci. Instrum.* **60**, 1690 (1989).

[76] J. J. Jia, T. A. Callcott, J. Yurkas, A. W. Ellis, F. J. Himpsel, M. G. Samant, J. Stöhr, D. L. Ederer, J. A. Carlisle, E. A. Hudson, L. J. Terminello, D. K. Shuh, and R. C. C. Perera, "First experimental results from IBM/Tenn/Tulane/LLNL/LBL undulator beamline at the Advanced Light-Source", *Rev. Sci. Instrum.* **66**, 1394 (1995).

[77] J. Nordgren and J. H. Guo, "Instrumentation for soft X-ray emission spectroscopy", *J. Electron Spectrosc. Relat. Phenom.* **110**, 1 (2000).

[78] S. Shin, A. Agui, M. Fujisawa, Y. Tezuka, T. Ishii, and N. Hirai, "Soft-X-Ray Emission Spectrometer For Undulator Radiation", *Rev. Sci. Instrum.* **66**, 1584 (1995).

[79] H. Rowland, "The concave diffraction grating", *Philos. Mag.* **13**, 469 (1882).

[80] K. D. Osborn and T. A. Callcott, "2 new optical designs for soft-x-ray spectrometers using variable-line-space gratings", *Rev. Sci. Instrum.* **66**, 3131 (1995).

[81] C. F. Hague, J. H. Underwood, A. Avila, R. Delaunay, H. Ringuenet, M. Marsi, and M. Sacchi, "Plane-grating flat-field soft x-ray spectrometer", *Rev. Sci. Instrum.* **76**, 023110 (2005).

[82] C. Dallera, E. Puppin, G. Trezzi, N. Incorvaia, A. Fasana, L. Braicovich, N. B. Brookes, and J. B. Goedkoop, "Soft X-ray emission spectroscopy at ESRF beamline 26 based on a helical undulator", *J. Synchrotron Radiat.* **3**, 231 (1996).

[83] D. Cocco, M. Zangrando, M. Matteucci, F. Bondino, M. Platè, M. Zacchigna, F. Parmigiani, B. Nelles, and K. C. Prince, "ComIXS on BACH: a compact soft x-ray spectrometer operating at Elettra", in T. Warwick, J. Arthur, H. A. Padmore, and J. Stöhr, editors, "American Institute of Physics Conference Series", volume 705 of *American Institute of Physics Conference Series*, 873–876 (2004).

[84] T. Tokushima, Y. Harada, H. Ohashi, Y. Senba, and S. Shin, "High performance slit-less spectrometer for soft x-ray emission spectroscopy", *Rev. Sci. Instrum.* **77**, 063107 (2006).

[85] M. C. Hettrick, J. H. Underwood, P. J. Batson, and M. J. Eckart, "Resolving power of 35,000 (5-ma) in the extreme ultraviolet employing a grazing-incidence spectrometer", *Appl. Optics* **27**, 200 (1988).

[86] M. C. Hettrick and J. H. Underwood, "Stigmatic high throughput monochromator for soft x-rays", *Appl. Optics* **25**, 4228 (1986).

[87] M. C. Hettrick and J. H. Underwood, "Varied-space grazing incidence gratings in high resolution scanning spectrometers", in T. Warwick, J. Arthur, H. A. Padmore, and J. Stöhr, editors, "American Institute of Physics Conference Series", volume 147 of *American Institute of Physics Conference Series*, 237–245 (1986).

[88] M. C. Hettrick and J. H. Underwood, "Optical system for high resolution spectrometer/monochromator", *U. S. Patent No. 4,776,696* (Oct. 11, 1988).

[89] J. H. Underwood, Z. Hussain, W. R. McKinney, and W. T., "1.5 meter VLS emission spectrometer", *Light Source Note* **LSBL #622**, 1 (2002).

[90] Y. D. Chuang, J. Pepper, W. McKinney, Z. Hussain, E. Gullikson, P. Batson, D. Qian, and M. Z. Hasan, "High-resolution soft X-ray emission spectrograph at advanced light source", *J. Phys. Chem. Solids* **66**, 2173 (2005).

[91] G. Ghiringhelli, A. Piazzalunga, C. Dallera, G. Trezzi, L. Braicovich, T. Schmitt, V. N. Strocov, R. Betemps, L. Patthey, X. Wang, and M. Grioni, "SAXES, a high resolution spectrometer for resonant x-ray emission in the 400–1600 eV energy range", *Rev. Sci. Instrum.* **77**, 113108 (2006).

[92] O. Fuchs, L. Weinhardt, C. Heske, E. Umbach, R. Follath, Y. Chuang, W. McKinney, and H. Z., "Design of a soft x-ray emission spectrograph for the study of biologically relevant molecules", *Light Source Note* **LSBL #875**, 1 (2002).

[93] H. Tsunemi, S. Nomoto, K. Hayashida, E. Miyata, H. Murakami, Y. Kato, G. Yuan, K. Murai, R. Kodama, and H. Daido, "Application of a newly developed CCD for spectral-width measurements of a 53 eV germanium laser", *Appl. Phys. B: Photophys. Laser Chem.* **57**, 331 (1993).

[94] H. C. Burger and P. H. van Cittert, "Wahre und scheinbare Intensitätsverteilung in Spektrallinien", *Z. Phys. A* **79**, 722 (1932).

[95] P. H. van Cittert, "Zum Einfluß der Spaltbreite auf die Intensitätsverteilung in Spektrallinien. II", *Z. Phys. A* **69**, 298 (1932).

[96] O. Fuchs, F. Maier, L. Weinhardt, M. Weigand, M. Blum, M. Zharnikov, J. Denlinger, M. Grunze, C. Heske, and E. Umbach, "A liquid flow cell to study the electronic structure of liquids with soft x-rays", *Nucl. Instrum. Methods Phys. Res., Sect. A* **585**, 172 (2008).

[97] T. Head-Gordon and G. Hura, "Water structure from scattering experiments and simulation", *Chem. Rev.* **102**, 2651 (2002).

[98] P. Wernet, D. Nordlund, U. Bergmann, M. Cavalleri, M. Odelius, H. Ogasawara, L. A. Naslund, T. K. Hirsch, L. Ojamae, P. Glatzel, L. G. M. Pettersson, and A. Nilsson, "The structure of the first coordination shell in liquid water", *Science* **304**, 995 (2004).

[99] J. D. Smith, C. D. Cappa, K. R. Wilson, B. M. Messer, R. C. Cohen, and R. J. Saykally, "Energetics of hydrogen bond network rearrangements in liquid water", *Science* **306**, 851 (2004).

[100] J. D. Smith, C. D. Cappa, K. R. Wilson, R. C. Cohen, P. L. Geissler, and R. J. Saykally, "Unified description of temperature-dependent hydrogen-bond rearrangements in liquid water", *Proc. Natl. Acad. Sci. U. S. A.* **102**, 14171 (2005).

[101] J. D. Smith, C. D. Cappa, B. M. Messer, W. S. Drisdell, R. C. Cohen, and R. J. Saykally, "Probing the local structure of liquid water by x-ray absorption spectroscopy", *J. Phys. Chem. B* **110**, 20038 (2006).

[102] R. L. C. Wang, H. J. Kreuzer, and M. Grunze, "Theoretical modeling and interpretation of X-ray absorption spectra of liquid water", *Phys. Chem. Chem. Phys.* **8**, 4744 (2006).

[103] D. Laage and J. T. Hynes, "A molecular jump mechanism of water reorientation", *Science* **311**, 832 (2006).

[104] U. Bergmann, P. Glatzel, and S. P. Cramer, "Bulk-sensitive XAS characterization of light elements: from X-ray Raman scattering to X-ray Raman spectroscopy", *Microchem. J.* **71**, 221 (2002).

[105] D. Nolting, E. F. Aziz, N. Ottosson, M. Faubel, I. V. Hertel, and B. Winter, "pH-induced protonation of lysine in aqueous solution causes chemical shifts in X-ray photoelectron spectroscopy", *J. Am. Chem. Soc.* **129**, 14068 (2007).

[106] R. Weber, B. Winter, P. M. Schmidt, W. Widdra, I. V. Hertel, M. Dittmar, and M. Faubel, "Photoemission from aqueous alkali-metal-iodide salt solutions using EUV synchrotron radiation", *J. Phys. Chem. B* **108**, 4729 (2004).

[107] B. Winter, E. F. Aziz, U. Hergenhahn, M. Faubel, and I. V. Hertel, "Hydrogen bonds in liquid water studied by photoelectron spectroscopy", *J. Chem. Phys.* **126**, 124504 (2007).

[108] B. Winter and M. Faubel, "Photoemission from liquid aqueous solutions", *Chem. Rev.* **106**, 1176 (2006).

[109] B. Winter, M. Faubel, I. V. Hertel, C. Pettenkofer, S. E. Bradforth, B. Jagoda-Cwiklik, L. Cwiklik, and P. Jungwirth, "Electron binding energies of hydrated H_3O^+ and OH^-: Photoelectron spectroscopy of aqueous acid and base solutions combined with electronic structure calculations", *J. Am. Chem. Soc.* **128**, 3864 (2006).

[110] B. Winter, U. Hergenhahn, M. Faubel, O. Bjorneholm, and I. V. Hertel, "Hydrogen bonding in liquid water probed by resonant Auger-electron spectroscopy", *J. Chem. Phys.* **127**, 094501 (2007).

[111] B. Winter, R. Weber, I. V. Hertel, M. Faubel, P. Jungwirth, E. C. Brown, and S. E. Bradforth, "Electron binding energies of aqueous alkali and halide ions: EUV photoelectron spectroscopy of liquid solutions and combined ab initio and molecular dynamics calculations", *J. Am. Chem. Soc.* **127**, 7203 (2005).

[112] B. Winter, R. Weber, I. V. Hertel, M. Faubel, L. Vrbka, and P. Jungwirth, "Effect of bromide on the interfacial structure of aqueous tetrabutylammonium iodide: Photoelectron spectroscopy and molecular dynamics simulations", *Chem. Phys. Lett.* **410**, 222 (2005).

[113] B. Winter, R. Weber, P. M. Schmidt, I. V. Hertel, M. Faubel, L. Vrbka, and P. Jungwirth, "Molecular structure of surface-active salt solutions: Photoelectron spectroscopy and molecular dynamics simulations of aqueous tetrabutylammonium iodide", *J. Phys. Chem. B* **108**, 14558 (2004).

[114] B. Winter, R. Weber, W. Widdra, M. Dittmar, M. Faubel, and I. V. Hertel, "Full valence band photoemission from liquid water using EUV synchrotron radiation", *J. Phys. Chem. A* **108**, 2625 (2004).

[115] K. R. Wilson, B. S. Rude, J. Smith, C. Cappa, D. T. Co, R. D. Schaller, M. Larsson, T. Catalano, and R. J. Saykally, "Investigation of volatile liquid surfaces by synchrotron x-ray spectroscopy of liquid microjets", *Rev. Sci. Instrum.* **75**, 725 (2004).

[116] S. Myneni, Y. Luo, L. A. Naslund, M. Cavalleri, L. Ojamae, H. Ogasawara, A. Pelmenschikov, P. Wernet, P. Vaterlein, C. Heske, Z. Hussain, L. G. M. Pettersson, and A. Nilsson, "Spectroscopic probing of local hydrogen-bonding structures in liquid water", *J. Phys.: Condens. Matter* **14**, L213 (2002).

[117] M. Freiwald, S. Cramm, W. Eberhardt, and S. Eisebitt, "Soft X-ray absorption spectroscopy in liquid environments", *J. Electron Spectrosc. Relat. Phenom.* **137-40**, 413 (2004).

[118] S. Yagi, Y. Matsumura, K. Soda, E. Hashimoto, and M. Taniguchi, "Interface study for liquid-solid state surface by means of the SK-edge NEXAFS method", *Surf. Interface Anal.* **36**, 1064 (2004).

[119] J. H. Guo, Y. Luo, A. Augustsson, J. E. Rubensson, C. Sathe, H. Agren, H. Siegbahn, and J. Nordgren, "X-ray emission spectroscopy of hydrogen bonding and electronic structure of liquid water", *Phys. Rev. Lett.* **89**, 137402 (2002).

[120] C. Heske, U. Groh, O. Fuchs, L. Weinhardt, E. Umbach, T. Schedel-Niedrig, C. H. Fischer, M. C. Lux-Steiner, S. Zweigart, T. P. Niesen, and F. Karg, "Monitoring chemical reactions at a liquid-solid interface: Water on $CuIn(S,Se)_2$ thin film solar cell absorbers", *J. Chem. Phys.* **119**, 10467 (2003).

[121] L. C. Duda, T. Schmitt, A. Augustsson, and J. Nordgren, "Resonant soft X-ray emission of solids and liquids", *J. Alloys Compd.* **362**, 116 (2004).

[122] M. Odelius, H. Ogasawara, D. Nordlund, O. Fuchs, L. Weinhardt, F. Maier, E. Umbach, C. Heske, Y. Zubavichus, M. Grunze, J. D. Denlinger, L. G. M. Pettersson, and A. Nilsson, "Ultrafast core-hole-induced dynamics in water probed by x-ray emission spectroscopy", *Phys. Rev. Lett.* **94**, 227401 (2005).

[123] T. Tokushima, Y. Harada, O. Takahashi, Y. Senba, H. Ohashi, L. G. M. Pettersson, A. Nilsson, and S. Shin, "High resolution X-ray emission spectroscopy of liquid water: The observation of two structural motifs", *Chem. Phys. Lett.* **460**, 387 (2008).

[124] O. Fuchs, M. Zharnikov, L. Weinhardt, M. Blum, M. Weigand, Y. Zubavichus, M. Bär, F. Maier, J. D. Denlinger, C. Heske, M. Grunze, and E. Umbach, "Isotope and temperature effects in liquid water probed by x-ray absorption and resonant x-ray emission spectroscopy", *Phys. Rev. Lett.* **100**, 027801 (2008).

[125] C. Heske, "Spectroscopic investigation of buried interfaces and liquids with soft X-rays", *Appl. Phys. A: Mater. Sci. Process.* **78**, 829 (2004).

[126] N. S. Sariciftci, "Role of Buckminsterfullerene, C_{60}, in organic photoelectric devices", *Prog. Quant. Electron.* **19**, 131 (1995).

[127] R. Bakry, R. M. Vallant, M. Najam-Ul-Haq, M. Rainer, Z. Szabo, C. W. Huck, and G. K. Bonn, "Medicinal applications of fullerenes", *Int. J. Nanomed.* **2**, 639 (2007).

[128] H. W. Kroto, J. R. Heath, S. C. Obrien, R. F. Curl, and R. E. Smalley, "C_{60} - Buckminsterfullerene", *Nature* **318**, 162 (1985).

[129] P. J. Benning, D. M. Poirier, N. Troullier, J. L. Martins, R. E. Weaver, J. H.and Haufler, L. P. F. Chibante, and R. E. Smalley, "Electronic states of solid C_{60} - symmetries and photoionization cross-sections", *Phys. Rev. B: Condens. Matter Mater. Phys.* **44**, 1962 (1991).

[130] P. A. Brühwiler, A. J. Maxwell, A. Nilsson, R. L. Whetten, and N. Martensson, "Resonant photoemission of solid C_{60}", *Chem. Phys. Lett.* **193**, 313 (1992).

[131] S. He, M. Arita, H. Namatame, M. Taniguchi, H. N. Li, and H. Y. Li, "Angle-dependent oscillations in valence-band photoemission intensity of C_{60}", *J. Phys.: Condens. Matter* **19**, 026202 (2007).

[132] E. Sohmen, J. Fink, and W. Kratschmer, "Electronic-structure studies of undoped and n-type doped fullerene C_{60}", *Europhys. Lett.* **17**, 51 (1992).

[133] L. J. Terminello, D. K. Shuh, F. J. Himpsel, D. A. Lapianosmith, J. Stöhr, D. S. Bethune, and G. Meijer, "Unfilled orbitals of C_{60} and C_{70} from carbon K-shell x-ray absorption fine structure", *Chem. Phys. Lett.* **182**, 491 (1991).

[134] L. Kjeldgaard, T. Kaambre, J. Schiessling, I. Marenne, J. N. O'Shea, J. Schnadt, C. J. Glover, M. Nagasono, D. Nordlund, M. G. Garnier, L. Qian, J. E. Rubensson, P. Rudolf, N. Martensson, J. Nordgren, and P. A. Brühwiler, "Intramolecular vibronic dynamics in molecular solids: C-60", *Physical Review B* **72**, 205414 (2005).

[135] O. Fuchs, L. Weinhardt, A. Fischer, M. Weigand, M. Blum, M. Bär, S. Pookpanratana, J. Denlinger, C. Heske, and E. Umbach, "Symmetry-resolved resonant x-ray emission study of an ordered PTCDA multilayer on Ag(111)", *in preparation* (2009).

[136] M. Friedrich, T. Wagner, G. Salvan, S. Park, T. U. Kampen, and D. R. T. Zahn, "Optical constants of 3,4,9,10-perylenetetracarboxylic dianhydride films on silicon and gallium arsenide studied by spectroscopic ellipsometry", *Appl. Phys. A: Mater. Sci. Process.* **75**, 501 (2002).

[137] M. Friedrich, G. Gavrila, C. Himcinschi, T. U. Kampen, A. Y. Kobitski, H. Mendez, G. Salvan, I. Cerrillo, J. Mendez, N. Nicoara, A. M. Baro, and D. R. T. Zahn, "Optical properties and molecular orientation in organic thin films", *J. Phys.: Condens. Matter* **15**, S2699 (2003).

[138] J. B. Gustafsson, H. M. Zhang, E. Moons, and L. S. O. Johansson, "Electron spectroscopy studies of PTCDA on Ag/Si(111)-root 3x root 3", *Phys. Rev. B: Condens. Matter Mater. Phys.* **75**, 155413 (2007).

[139] M. Tengelin-Nilsson, L. Ilver, and J. Kanski, "Photoemission and low-energy electron diffraction studies of 3,4,9,10-perylene tetracarboxylic dianhydride layers on Si(111): H", *Surf. Sci.* **464**, 265 (2000).

[140] K. Iwasaki, K. Umishita, M. Sakata, and S. Hino, "Electrical conductivity and electronic structure of potassium doped PTCDA", *Synth. Met.* **121**, 1395 (2001).

[141] M. Tengelin-Nilsson, L. Ilver, and J. Kanski, "Photoelectron spectroscopic studies of thin PTCDA layers on TiSe$_2$", *Org. Electron.* **3**, 73 (2002).

[142] H. Yamane and S. Kera, "Intermolecular energy-band dispersion in PTCDA multilayers", *Phys. Rev. B: Condens. Matter Mater. Phys.* **68**, 033102 (2003).

[143] G. G. Fuentes and M. Knupfer, "Electronic structure and work function of potassium-doped PTCDA thin films", *Appl. Phys. A: Mater. Sci. Process.* **84**, 329 (2006).

[144] N. Nicoara, E. Roman, J. M. Gomez-Rodriguez, J. A. Martin-Gago, and J. Mendez, "Scanning tunneling and photoemission spectroscopies at the PTCDA/Au(111) interface", *Org. Electron.* **7**, 287 (2006).

[145] R. Hudej, G. Bratina, and M. Onellion, "Morphology and electronic structure of thin 3,4,9,10-perylenetetracarboxylic dianhydride layers on Si(001)", *Thin Solid Films* **515**, 1424 (2006).

[146] I. G. Hill, A. Kahn, J. Cornil, D. A. dos Santos, and J. L. Bredas, "Occupied and unoccupied electronic levels in organic pi-conjugated molecules: comparison between experiment and theory", *Chem. Phys. Lett.* **317**, 444 (2000).

[147] N. Sato, H. Yoshida, and K. Tsutsumi, "Unoccupied electronic structure in organic thin films studied by inverse photoemission spectroscopy", *J. Mater. Chem.* **10**, 85 (2000).

[148] P. J. Unwin, C. P. A. Mulcahy, and T. S. Jones, "Unoccupied electronic states in ordered PTCDA and H_2Pc thin films grown on InAs and InSb: a resonance HREELS study", *Surf. Sci.* **482**, 1222 (2001).

[149] T. Nakamura, K. Iwasawa, S. Kera, Y. Azuma, K. K. Okudaira, and N. Ueno, "Low-energy molecular exciton in indium/perylene-3,4,9, 10-tetracarboxylic dianhydride system observed by electronic energy loss spectroscopy", *Appl. Surf. Sci.* **212**, 515 (2003).

[150] A. Kraft, R. Temirov, S. K. M. Henze, S. Soubatch, M. Rohlfing, and F. S. Tautz, "Lateral adsorption geometry and site-specific electronic structure of a large organic chemisorbate on a metal surface", *Phys. Rev. B: Condens. Matter Mater. Phys.* **74**, 041402 (2006).

[151] M. Rohlfing, R. Temirov, and F. S. Tautz, "Adsorption structure and scanning tunneling data of a prototype organic-inorganic interface: PTCDA on Ag(111)", *Phys. Rev. B: Condens. Matter Mater. Phys.* **76**, 115421 (2007).

[152] G. Salvan, C. Himcinschi, A. Y. Kobitski, M. Friedrich, H. P. Wagner, T. U. Kampen, and D. R. T. Zahn, "Crystallinity of PTCDA films on silicon derived via optical spectroscopic measurements", *Appl. Surf. Sci.* **175**, 363 (2001).

[153] A. Y. Kobitski, G. Salvan, H. P. Wagner, and D. R. T. Zahn, "Time-resolved photoluminescence characterisation of thin PTCDA films on Si(100)", *Appl. Surf. Sci.* **179**, 209 (2001).

[154] A. Y. Kobitski, R. Scholz, G. Salvan, T. U. Kampen, H. P. Wagner, and D. R. T. Zahn, "Time-resolved photoluminescence study of excitons in thin PTCDA films at various temperatures", *Appl. Surf. Sci.* **212**, 428 (2003).

[155] A. Y. Kobitski, R. Scholz, D. R. T. Zahn, and H. P. Wagner, "Time-resolved photoluminescence study of excitons in alpha-PTCDA as a function of temperature", *Phys. Rev. B: Condens. Matter Mater. Phys.* **68**, 155201 (2003).

[156] R. Scholz and M. Schreiber, "Linear optical properties of perylene-based chromophores", *Chem. Phys.* **325**, 9 (2006).

[157] H. P. Steinrück, "Angle-Resolved UV-Photoelectron Spectroscopy", *Vacuum* **45**, 715 (1994).

[158] Y. Azuma, T. Hasebe, T. Miyamae, K. K. Okudaira, Y. Harada, K. Seki, E. Morikawa, V. Saile, and N. Ueno, "Angle-resolved UV photoelectron spectra (UPS) of thin films of perylene-3,4,9,10-tetracarboxylic dianhydride on MoS_2", *Journal Of Synchrotron Radiation* **5**, 1044 (1998).

[159] A. Andreasson, M. Tengelin-Nilsson, L. Ilver, and J. Kanski, "Photoelectron spectroscopic studies of ultra-thin CuPc and PTCDA layers on Cu(100)", *Synthetic Metals* **158**, 45 (2008).

[160] J. E. Rubensson, J. Lüning, S. Eisebitt, and W. Eberhardt, "It's always a one-step process", *Applied Physics A-Materials Science & Processing* **65**, 91 (1997).

[161] A. Nilsson, M. Weinelt, T. Wiell, P. Bennich, O. Karis, N. Wassdahl, J. Stöhr, and M. G. Samant, "An atom-specific look at the surface chemical bond", *Phys. Rev. Lett.* **78**, 2847 (1997).

[162] A. Nilsson, N. Wassdahl, M. Weinelt, O. Karis, T. Wiell, P. Bennich, J. Hasselström, A. Föhlisch, J. Stöhr, and M. Samant, "Local probing of the surface chemical bond using X-ray emission spectroscopy", *Appl. Phys. A: Mater. Sci. Process.* **65**, 147 (1997).

[163] P. Skytt, J. H. Guo, N. Wassdahl, J. Nordgren, Y. Luo, and H. Agren, "Probing symmetry-breaking upon core excitation with resonant x-ray-fluorescence", *Phys. Rev. A: At., Mol., Opt. Phys.* **52**, 3572 (1995).

[164] Y. Luo, H. Agren, F. Gel'mukhanov, J. H. Guo, P. Skytt, N. Wassdahl, and J. Nordgren, "Symmetry-selective resonant inelastic x-ray-scattering of C_{60}", *Phys. Rev. B: Condens. Matter Mater. Phys.* **52**, 14479 (1995).

[165] P. Bennich, T. Wiell, O. Karis, M. Weinelt, N. Wassdahl, A. Nilsson, M. Nyberg, L. G. M. Pettersson, J. Stöhr, and M. Samant, "Nature of the surface chemical bond in N_2 On Ni(100) studied by x-ray-emission spectroscopy and ab initio calculations", *Phys. Rev. B: Condens. Matter Mater. Phys.* **57**, 9274 (1998).

[166] J. Hasselström, A. Föhlisch, O. Karis, N. Wassdahl, M. Weinelt, A. Nilsson, M. Nyberg, L. G. M. Pettersson, and J. Stöhr, "Ammonia adsorbed on Cu(110): An angle resolved x-ray spectroscopic and ab initio study", *J. Chem. Phys.* **110**, 4880 (1999).

[167] M. Stichler, C. Keller, C. Heske, M. Staufer, U. Birkenheuer, N. Rosch, W. Wurth, and D. Menzel, "X-ray emission spectroscopy of NO adsorbates on Ru(001)", *Surf. Sci.* **448**, 164 (2000).

[168] A. Föhlisch, J. Hasselström, P. Bennich, N. Wassdahl, O. Karis, A. Nilsson, L. Triguero, M. Nyberg, and L. G. M. Pettersson, "Ground-state interpretation of x-ray emission spectroscopy on adsorbates: CO adsorbed on Cu(100)", *Phys. Rev. B: Condens. Matter Mater. Phys.* **61**, 16229 (2000).

[169] J. Hasselström, O. Karis, M. Nyberg, L. G. M. Pettersson, M. Weinelt, N. Wassdahl, and A. Nilsson, "The bonding and electronic structure changes upon adsorption of important functional groups: Glycine on copper", *J. Phys. Chem. B* **104**, 11480 (2000).

[170] H. Öström, L. Triguero, K. Weiss, H. Ogasawara, M. G. Garnier, D. Nordlund, M. Nyberg, L. G. M. Pettersson, and A. Nilsson, "Orbital rehybridization in n-octane adsorbed on Cu(110)", *J. Chem. Phys.* **118**, 3782 (2003).

[171] H. Öström, A. Föhlisch, M. Nyberg, M. Weinelt, C. Heske, L. G. M. Pettersson, and A. Nilsson, "Ethylene on Cu(110) and Ni(110): electronic structure and bonding derived from X-ray spectroscopy and theory", *Surf. Sci.* **559**, 85 (2004).

[172] H. Öström, D. Nordlund, H. Ogasawara, K. Weiss, L. Triguero, L. G. M. Pettersson, and A. Nilsson, "Geometric structure and chemical bonding of acetylene adsorbed on Cu(110)", *Surf. Sci.* **565**, 206 (2004).

[173] E. Tegeler, M. Iwan, and E. E. Koch, "Electronic structure of the valence bands of H_2-phthalocyanine, Mg-phthalocyanine and Pt-phthalocyanine derived from soft-x-ray emission and photoelectron emission spectra", *J. Electron Spectrosc. Relat. Phenom.* **22**, 297 (1981).

[174] E. Z. Kurmaev, S. N. Shamin, V. R. Galakhov, A. Moewes, T. Otsuka, S. Koizume, K. Endo, H. E. Katz, M. Bach, M. Neumann, D. L. Ederer, and M. Iwami, "Electronic structure of thiophenes and phtalocyanines", *Phys. Rev. B: Condens. Matter Mater. Phys.* **6404**, 045211 (2001).

[175] J. E. Downes, C. McGuinness, P. A. Glans, T. Learmonth, D. F. Fu, P. Sheridan, and K. E. Smith, "Electronic structure near the Fermi level of the organic semiconductor copper phthalocyanine", *Chem. Phys. Lett.* **390**, 203 (2004).

[176] Y. F. Zhang, S. C. Wang, T. Learmonth, L. Plucinski, A. Y. Matsuura, S. Bernardis, C. O'Donnell, J. E. Downes, and K. E. Smith, "Electronic excitations in vanadium oxide phthalocyanine studied via resonant soft X-ray emission and resonant inelastic X-ray scattering", *Chem. Phys. Lett.* **413**, 95 (2005).

[177] Y. F. Zhang, J. E. Downes, S. C. Wang, T. Learmonth, L. Plucinski, A. Y. Matsuura, C. McGuinness, P. A. Glans, S. Bernardis, C. O'Donnell, and K. E. Smith, "Electronic structure in thin film organic semiconductors studied using soft X-ray emission and resonant inelastic X-ray scattering", *Thin Solid Films* **515**, 394 (2006).

[178] Y. F. Zhang, T. Learmonth, S. C. Wang, A. Y. Matsuura, J. Downes, L. Plucinski, S. Bernardis, C. O'Donnell, and K. E. Smith, "Electronic structure of the organic semiconductor vanadyl phthalocyanine (VO-Pc)", *J. Mater. Chem.* **17**, 1276 (2007).

[179] G. McCormick and W. Gordy, "Electron spin resonance studies of radiation damage to peptides", *J. Phys. Chem.* **62**, 783 (1958).

[180] K. S. Stenn and G. F. Bahr, "A study of mass loss and product formation after irradiation of some dry amino acids, peptides, polypeptides and proteins with an electron beam of low current density", *J. Histochem. Cytochem.* **18**, 574 (1970).

[181] H. C. Box and E. E. Budzinsk, "Oxidation and reduction of amino acids by ionizing radiation", *J. Chem. Phys.* **55**, 2446 (1971).

[182] H. C. Box, "Radiation damage mechanisms as revealed through electron spin resonance spectroscopy", *Annu. Rev. Nucl. Part. Sci.* **22**, 355 (1972).

[183] M. Isaacson, D. Johnson, and A. V. Crewe, "Electron-beam excitation and damage of biological molecules - its implications for specimen damage in electron microscopy", *Radiat. Res.* **55**, 205 (1973).

[184] H. C. Box, E. Budzinsk, and H. G. Freund, "Effects of ionizing-radiation on tyrosine", *J. Chem. Phys.* **61**, 2222 (1974).

[185] S. D. Lin, "Electron radiation-damage of thin-films of glycine, diglycine, and aromatic amino-acids", *Radiat. Res.* **59**, 521 (1974).

[186] S. M. Adams, E. E. Budzinski, and H. C. Box, "Primary oxidation and reduction products in x-irradiated aspartic-acid", *J. Chem. Phys.* **65**, 998 (1976).

[187] A. Benninghoven, W. Lange, M. Jirikowsky, and D. Holtkamp, "Investigations on the mechanism of secondary ion formation from organic compounds — amino-acids", *Surf. Sci.* **123**, L721 (1982).

[188] W. Eberhardt, T. K. Sham, R. Carr, S. Krummacher, M. Strongin, S. L. Weng, and D. Wesner, "Site-specific fragmentation of small molecules following soft-x-ray excitation", *Phys. Rev. Lett.* **50**, 1038 (1983).

[189] R. H. Wade, "The temperature-dependence of radiation damage in organic and biological materials", *Ultramicroscopy* **14**, 265 (1984).

[190] T. Strunskus, C. Hahn, and M. Grunze, "Mechanism of x-ray-induced degradation of pyromellitic dianhydride", *J. Electron Spectrosc. Relat. Phenom.* **61**, 193 (1993).

[191] M. J. Bozack, Y. Zhou, and S. D. Worley, "Structural modifications in the amino-acid lysine induced by soft-x-ray irradiation", *J. Chem. Phys.* **100**, 8392 (1994).

[192] A. C. Cheng and M. Caffrey, "Free radical mediated x-ray damage of model membranes", *Biophys. J.* **70**, 2212 (1996).

[193] L. Sanche, "Secondary electrons in radiation chemistry and biology", *Journal de Chimie Physique* **94**, 216 (1997).

[194] W. P. Burmeister, "Structural changes in a cryo-cooled protein crystal owing to radiation damage", *Acta Crystallographica Section D-Biological Crystallography* **56**, 328 (2000).

[195] H. Abdoul-Carime, P. C. Dugal, and L. Sanche, "Desorption induced by electronic transitions (DIET) of neutral fragments from chemisorbed biological molecular systems", *Surf. Sci.* **451**, 102 (2000).

[196] P. Feulner, R. Romberg, S. P. Frigo, R. Weimar, M. Gsell, A. Ogurtsov, and D. Menzel, "Recent progress in the investigation of core hole-induced photon stimulated desorption from adsorbates: excitation site-dependent bond breaking, and charge rearrangement", *Surf. Sci.* **451**, 41 (2000).

[197] K. Heister, M. Zharnikov, M. Grunze, L. S. O. Johansson, and A. Ulman, "Characterization of X-ray induced damage in alkanethiolate monolayers by high-resolution photoelectron spectroscopy", *Langmuir* **17**, 8 (2001).

[198] M. A. H. du Penhoat, M. A. Huels, P. Cloutier, J. P. Jay-Gerin, and L. Sanche, "Electron stimulated desorption of H- from thin films of thymine and uracil", *J. Chem. Phys.* **114**, 5755 (2001).

[199] E. S. Kempner, "Effects of high-energy electrons and gamma rays directly on protein molecules", *J. Pharm. Sci.* **90**, 1637 (2001).

[200] T. Coffey, S. G. Urquhart, and H. Ade, "Characterization of the effects of soft X-ray irradiation on polymers", *J. Electron Spectrosc. Relat. Phenom.* **122**, 65 (2002).

[201] L. Sanche, "Nanoscopic aspects of radiobiological damage: Fragmentation induced by secondary low-energy electrons", *Mass Spectrom. Rev.* **21**, 349 (2002).

[202] V. Cherezov, K. M. Riedl, and M. Caffrey, "Too hot to handle? Synchrotron X-ray damage of lipid membranes and mesophases", *J. Synchrotron Radiat.* **9**, 333 (2002).

126

[203] Y. Zubavichus, O. Fuchs, L. Weinhardt, C. Heske, E. Umbach, J. D. Den-linger, and M. Grunze, "Soft x-ray-induced decomposition of amino acids: An XPS, mass spectrometry, and NEXAFS study", *Radiat. Res.* **161**, 346 (2004).

[204] Y. Zubavichus, M. Zharnikov, A. Shaporenko, O. Fuchs, L. Weinhardt, C. Heske, E. Umbach, J. D. Denlinger, and M. Grunze, "Soft X-ray induced decomposition of phenylalanine and tyrosine: A comparative study", *J. Phys. Chem. A* **108**, 4557 (2004).

[205] B. Krause, A. C. Dürr, K. Ritley, F. Schreiber, H. Dosch, and D. Smilgies, "Structure and growth morphology of an archetypal system for organic epitaxy: PTCDA on Ag(111)", *Phys. Rev. B: Condens. Matter Mater. Phys.* **66**, 235404 (2002).

[206] A. Schöll, Y. Zou, T. Schmidt, R. Fink, and E. Umbach, "Energy calibration and intensity normalization in high-resolution NEXAFS spectroscopy", *J. Electron Spectrosc. Relat. Phenom.* **129**, 1 (2003).

[207] A. Schöll, unpublished data (2008).

[208] Y. Muramatsu, S. Hirono, S. Umemura, Y. Ueno, T. Hayashi, M. M. Grush, E. M. Gullikson, and R. C. C. Perera, "Soft X-ray emission and absorption spectra in the C K region of sputtered amorphous carbon films", *Carbon* **39**, 1403 (2001).

[209] N. Kosugi and H. Kuroda, "Efficient methods for solving the open-shell SCF problem and for obtaining an initial guess - the one-hamiltonian and the partial SCF methods", *Chem. Phys. Lett.* **74**, 490 (1980).

[210] N. Kosugi, "Strategies to vectorize conventional SCF-CL algorithms", *Theor. Chim. Acta* **72**, 149 (1987).

[211] O. Fuchs, M. Zharnikov, L. Weinhardt, M. Blum, M. Weigand, Y. Zubavichus, M. Bär, F. Maier, J. D. Denlinger, C. Heske, M. Grunze, and E. Umbach, "Comment on "Isotope and temperature effects in liquid water probed by x-ray absorption and resonant x-ray emission spectroscopy" - Fuchs et al. reply", *Phys. Rev. Lett.* **100**, 249802 (2008).

[212] L. G. M. Pettersson, T. Tokushima, Y. Harada, O. Takahashi, S. Shin, and A. Nilsson, "Comment on "Isotope and temperature effects in liquid water probed by x-ray absorption and resonant x-ray emission spectroscopy"", *Phys. Rev. Lett.* **100**, 249801 (2008).

[213] M. Odelius and O. Takahashi, "Information content in O 1s K-edge X-ray emission spectroscopy of hydrogen-bonded liquids", *submitted to Phys. Rev. B* (2008).

[214] R. T. Hart, C. J. Benmore, J. Neuefeind, S. Kohara, B. Tomberli, and P. A. Egelstaff, "Temperature dependence of isotopic quantum effects in water", *Phys. Rev. Lett.* **94**, 047801 (2005).

[215] B. Hetenyi, F. De Angelis, P. Giannozzi, and R. Car, "Calculation of near-edge x-ray-absorption fine structure at finite temperatures: Spectral signatures of hydrogen bond breaking in liquid water", *J. Chem. Phys.* **120**, 8632 (2004).

[216] D. Prendergast and G. Galli, "X-ray absorption spectra of water from first principles calculations", *Phys. Rev. Lett.* **96**, 215502 (2006).

[217] M. Leetmaa, M. Ljungberg, H. Ogasawara, M. Odelius, L. A. Naslund, A. Nilsson, and L. G. M. Pettersson, "Are recent water models obtained by fitting diffraction data consistent with infrared/Raman and x-ray absorption spectra?", *J. Chem. Phys.* **125**, 244510 (2006).

[218] M. Odelius, M. Cavalleri, A. Nilsson, and L. G. M. Pettersson, "X-ray absorption spectrum of liquid water from molecular dynamics simulations: Asymmetric model", *Phys. Rev. B: Condens. Matter Mater. Phys.* **73**, 024205 (2006).

[219] C. G. Elles, I. A. Shkrob, R. A. Crowell, and S. E. Bradforth, "Excited state dynamics of liquid water: Insight from the dissociation reaction following two-photon excitation", *J. Chem. Phys.* **126**, 164503 (2007).

[220] S. Kashtanov, A. Augustsson, Y. Luo, J. H. Guo, C. Sathe, J. E. Rubensson, H. Siegbahn, J. Nordgren, and H. Agren, "Local structures of liquid water studied by x-ray emission spectroscopy", *Phys. Rev. B: Condens. Matter Mater. Phys.* **69**, 024201 (2004).

[221] E. Gilberg, M. J. Hanus, and B. Foltz, "Investigation of the electronic-structure of ice by high-resolution x-ray spectroscopy", *J. Chem. Phys.* **76**, 5093 (1982).

[222] D. Nordlund, H. Ogasawara, H. Bluhm, O. Takahashi, M. Odelius, M. Nagasono, L. G. M. Pettersson, and A. Nilsson, "Probing the electron delocalization in liquid water and ice at attosecond time scales", *Phys. Rev. Lett.* **99**, 217406 (2007).

[223] J. Nordgren, L. O. Werme, H. Agren, C. Nordling, and K. Siegbahn, "X-ray-emission spectrum of water", *J. Phys. B: At., Mol. Opt. Phys.* **8**, L18 (1975).

[224] R. A. Kuharski and P. J. Rossky, "A quantum-mechanical study of structure in liquid H_2O and D_2O", *J. Chem. Phys.* **82**, 5164 (1985).

[225] G. Nemethy and H. A. Scheraga, "Structure of water + hydrophobic bonding in proteins: 4. thermodynamic properties of liquid deuterium oxide", *J. Chem. Phys.* **41**, 680 (1964).

[226] J. D. Simon, "Time-resolved studies of solvation in polar media", *Acc. Chem. Res.* **21**, 128 (1988).

[227] R. M. Stratt and M. Maroncelli, "Nonreactive dynamics in solution: The emerging molecular view of solvation dynamics and vibrational relaxation", *J. Phys. Chem.* **100**, 12981 (1996).

[228] J. D. Bernal and R. H. Fowler, "A theory of water and ionic solution, with particular reference to hydrogen and hydroxyl ions", *J. Chem. Phys.* **1**, 515 (1933).

[229] M. Tuckerman, K. Laasonen, M. Sprik, and M. Parrinello, "Ab-initio molecular-dynamics simulation of the solvation and transport of H_3O^+ and OH^- ions in water", *J. Phys. Chem.* **99**, 5749 (1995).

[230] B. Brena, D. Nordlund, M. Odelius, H. Ogasawara, A. Nilsson, and L. G. M. Pettersson, "Ultrafast molecular dissociation of water in ice", *Phys. Rev. Lett.* **93**, 148302 (2004).

[231] I. Hjelte, M. N. Piancastelli, R. F. Fink, O. Bjorneholm, M. Bassler, R. Feifel, A. Giertz, H. Wang, K. Wiesner, A. Ausmees, C. Miron, S. L. Sorensen, and S. Svensson, "Evidence for ultra-fast dissociation of molecular water from resonant Auger spectroscopy", *Chem. Phys. Lett.* **334**, 151 (2001).

[232] J. D. Bryngelson and E. M. Billings, "From interatomic interactions to protein structure", *Lecture Notes in Physics* **480**, 320 (2003).

[233] D. A. Snyder, Y. Chen, N. G. Denissova, T. Acton, J. M. Aramini, M. Ciano, R. Karlin, J. F. Liu, P. Manor, P. A. Rajan, P. Rossi, G. V. T. Swapna, R. Xiao, B. Rost, J. Hunt, and G. T. Montelione, "Comparisons of NMR spectral quality and success in crystallization demonstrate that NMR and X-ray crystallography are complementary methods for small protein structure determination", *J. Am. Chem. Soc.* **127**, 16505 (2005).

[234] K. V. Ewart, Q. Lin, and C. L. Hew, "Structure, function and evolution of antifreeze proteins", *Cell. Mol. Life Sci.* **55**, 271 (1999).

[235] M. M. Beerbom, R. Gargagliano, and R. Schlaf, "Determination of the electronic structure of self-assembled L-cysteine/Au interfaces using photoemission spectroscopy", *Langmuir* **21**, 3551 (2005).

[236] J. Hasselström, O. Karis, M. Weinelt, N. Wassdahl, A. Nilsson, M. Nyberg, L. G. M. Pettersson, M. G. Samant, and J. Stöhr, "The adsorption structure of glycine adsorbed on Cu(110); comparison with formate and acetate/Cu(110)", *Surf. Sci.* **407**, 221 (1998).

[237] M. Nyberg, J. Hasselström, O. Karis, N. Wassdahl, M. Weinelt, A. Nilsson, and L. G. M. Pettersson, "The electronic structure and surface chemistry of glycine adsorbed on Cu(110)", *J. Chem. Phys.* **112**, 5420 (2000).

[238] M. Nyberg, M. Odelius, A. Nilsson, and L. G. M. Pettersson, "Hydrogen bonding between adsorbed deprotonated glycine molecules on Cu(110)", *J. Chem. Phys.* **119**, 12577 (2003).

[239] Y. Zubavichus, A. Shaporenko, M. Grunze, and M. Zharnikov, "NEXAFS spectroscopy of homopolypeptides at all relevant absorption edges: Poly-isoleucine, polytyrosine, and polyhistidine", *J. Phys. Chem. B* **111**, 9803 (2007).

[240] Y. Zubavichus, A. Shaporenko, M. Grunze, and M. Zharnikov, "Innershell absorption spectroscopy of amino acids at all relevant absorption edges", *J. Phys. Chem. A* **109**, 6998 (2005).

[241] Y. Zubavichus, A. Shaporenko, M. Grunze, and M. Zharnikov, "Solid-state near-edge X-ray absorption fine structure spectra of glycine in various charge states", *J. Phys. Chem. B* **110**, 3420 (2006).

[242] J. Boese, A. Osanna, C. Jacobsen, and J. Kirz, "Carbon edge XANES spectroscopy of amino acids and peptides", *J. Electron Spectrosc. Relat. Phenom.* **85**, 9 (1997).

[243] M. Tanaka, K. Nakagawa, T. Koketsu, A. Agui, and A. Yokoya, "Oxygen K-edge X-ray absorption near edge structures (XANES) of sublimated films of amino acids", *J. Synchrotron Radiat.* **8**, 1009 (2001).

[244] M. L. Gordon, G. Cooper, C. Morin, T. Araki, C. C. Turci, K. Kaznatcheev, and A. P. Hitchcock, "Inner-shell excitation spectroscopy of the peptide bond: Comparison of the C 1s, N 1s, and O 1s spectra of glycine, glycyl-glycine, and glycyl-glycyl-glycine", *J. Phys. Chem. A* **107**, 6144 (2003).

[245] K. Kaznacheyev, A. Osanna, C. Jacobsen, O. Plashkevych, O. Vahtras, and H. Agren, "Innershell absorption spectroscopy of amino acids", *J. Phys. Chem. A* **106**, 3153 (2002).

[246] Y. Zubavichus, M. Zharnikov, A. Schaporenko, and M. Grunze, "NEXAFS study of glycine and glycine-based oligopeptides", *J. Electron Spectrosc. Relat. Phenom.* **134**, 25 (2004).

[247] G. Cooper, M. Gordon, D. Tulumello, C. Turci, K. Kaznatcheev, and A. R. Hitchcock, "Inner shell excitation of glycine, glycyl-glycine, alanine and phenylalanine", *J. Electron Spectrosc. Relat. Phenom.* **137-40**, 795 (2004).

[248] G. Tzvetkov, G. Koller, Y. Zubavichus, O. Fuchs, M. B. Casu, C. Heske, E. Umbach, M. Grunze, M. G. Ramsey, and F. P. Netzer, "Bonding and structure of glycine on ordered Al_2O_3 film surfaces", *Langmuir* **20**, 10551 (2004).

[249] Y. Zubavichus, M. Zharnikov, Y. J. Yang, O. Fuchs, C. Heske, E. Umbach, G. Tzvetkov, F. P. Netzer, and M. Grunze, "Surface chemistry of ultrathin films of histidine on gold as probed by high-resolution synchrotron photoemission", *J. Phys. Chem. B* **109**, 884 (2005).

[250] O. Plekan, V. Feyer, R. Richter, M. Coreno, M. de Simone, K. C. Prince, and V. Carravetta, "An X-ray absorption study of glycine, methionine and proline", *J. Electron Spectrosc. Relat. Phenom.* **155**, 47 (2007).

[251] L. H. Coutinho, M. G. P. Homem, R. L. Cavasso, R. R. T. Marinho, A. F. Lago, G. G. B. de Souza, and A. N. de Brito, "Photoabsorption and photoionization studies of the amino acid proline in the VUV region", *Brazilian J. Phys.* **35**, 940 (2005).

[252] O. Plekan, V. Feyer, R. Richter, M. Coreno, M. de Simone, K. C. Prince, and V. Carravetta, "Investigation of the amino acids glycine, proline, and methionine by photoemission spectroscopy", *J. Phys. Chem. A* **111**, 10998 (2007).

[253] O. Plekan, V. Feyer, R. Richter, M. Coreno, M. de Simone, K. C. Prince, and V. Carravetta, "Photoemission and the shape of amino acids", *Chem. Phys. Lett.* **442**, 429 (2007).

[254] I. Powis, E. E. Rennie, U. Hergenhahn, O. Kugeler, and R. Bussy-Socrate, "Investigation of the gas-phase amino acid alanine by synchrotron radiation photoelectron spectroscopy", *J. Phys. Chem. A* **107**, 25 (2003).

[255] A. R. Slaughter and M. S. Banna, "Core-photoelectron binding-energies of gaseous glycine - correlation with its proton affinity and gas-phase acidity", *J. Phys. Chem.* **92**, 2165 (1988).

[256] L. Klasinc, "Application of photoelectron-spectroscopy to biologically-active molecules and their constituent parts .3. amino-acids", *J. Electron Spectrosc. Relat. Phenom.* **8**, 161 (1976).

[257] P. H. Cannington and N. S. Ham, "Photoelectron-Spectra Of Amino-Acids - Survey", *J. Electron Spectrosc. Relat. Phenom.* **15**, 79 (1979).

[258] P. H. Cannington and N. S. Ham, "He(I) And He(II) photoelectron-spectra of glycine and related molecules", *J. Electron Spectrosc. Relat. Phenom.* **32**, 139 (1983).

[259] B. M. Messer, C. D. Cappa, J. D. Smith, W. S. Drisdell, C. P. Schwartz, R. C. Cohen, and R. J. Saykally, "Local hydration environments of amino acids and dipeptides studied by X-ray spectroscopy of liquid microjets", *J. Phys. Chem. B* **109**, 21640 (2005).

[260] R. N. S. Sodhi and C. E. Brion, "Reference energies for inner shell electron energy-loss spectroscopy", *J. Electron Spectrosc. Relat. Phenom.* **34**, 363 (1984).

[261] A. F. Lago, L. H. Coutinho, R. R. T. Marinho, A. N. de Brito, and G. G. B. de Souza, "Ionic dissociation of glycine, alanine, valine and proline as induced by VUV (21.21 eV) photons", *Chem. Phys.* **307**, 9 (2004).

[262] O. Plekan, V. Feyer, R. Richter, M. Coreno, M. de Simone, and K. C. Prince, "Photofragmentation of guanine, cytosine, leucine and methionine", *Chem. Phys.* **334**, 53 (2007).

[263] D. L. Nelson and M. M. Cox, *Lehninger Principles of Biochemistry*, Worth Publishers (2000).

[264] M. Blum, unpublished data (2008).

[265] Internet, URL http://www-cxro.lbl.gov.

OWN PUBLICATIONS

Own publications as first author in peer-reviewed journals

[A01]   O. Fuchs, L. Weinhardt, A. Fischer, M. Weigand, M. Blum, M. Bär, S. Pookpanratana, J. Denlinger, C. Heske, and E. Umbach, "Symmetry-resolved resonant x-ray emission study of an ordered PTCDA multilayer on Ag(111)", *in preparation* (2009).

[A02]   O. Fuchs, M. Blum, M. Weigand, E. Umbach, L. Weinhardt, M. Bär, C. Heske, J. Denlinger, Y.-D. Chuang, W. McKinney, Z. Hussain, E. Gullikson, M. Jones, P. Batson, and R. Follath, "High-resolution, high-transmission soft x-ray spectrometer for the study of biological samples", *Rev. Sci. Instrum.* **80**, 063103 (2009).

[A03]   O. Fuchs, F. Maier, L. Weinhardt, M. Weigand, M. Blum, M. Zharnikov, J. Denlinger, M. Grunze, C. Heske, and E. Umbach, "A liquid flow cell to study the electronic structure of liquids with soft x-rays", *Nucl. Instrum. Methods Phys. Res., Sect. A* **585**, 172 (2008).

[A04]   O. Fuchs, M. Zharnikov, L. Weinhardt, M. Blum, M. Weigand, Y. Zubavichus, M. Bär, F. Maier, J. D. Denlinger, C. Heske, M. Grunze, and E. Umbach, "Isotope and temperature effects in liquid water probed by x-ray absorption and resonant x-ray emission spectroscopy", *Phys. Rev. Lett.* **100**, 027801 (2008).

[A05]   O. Fuchs, M. Zharnikov, L. Weinhardt, M. Blum, M. Weigand, Y. Zubavichus, M. Bär, F. Maier, J. D. Denlinger, C. Heske, M. Grunze, and E. Umbach, "Comment on "Isotope and temperature effects in liquid water probed by x-ray absorption and resonant x-ray emission spectroscopy" - Fuchs *et al.* reply", *Phys. Rev. Lett.* **100**, 249802 (2008).

[A06]   O. Fuchs, L. Weinhardt, C. Heske, E. Umbach, R. Follath, Y. Chuang, W. McKinney, and H. Z., "Design of a soft x-ray emission spectrograph for the study of biologically relevant molecules", *Light Source Note* **LSBL** #875, 1 (2002).

Own publications as coauthor in peer-reviewed journals

[C01]   M. Bär, K.-S. Ahn, S. Shet, Y. Yan, L. Weinhardt, O. Fuchs, M. Blum, S. Pookpanratana, K. George, W. Yang, J. D. Denlinger, M. Al-Jassim, and C. Heske, "Impact of air-exposure on the chemical and electronic structure of ZnO:Zn$_3$N$_2$ thin films", *Appl. Phys. Lett.* **94**, 012110 (2009).

[C02]   M. Bär, L. Weinhardt, S. Pookpanratana, C. Heske, S. Nishiwaki, W. Shafarman, O. Fuchs, M. Blum, W. Yang, and J. D. Denlinger, "Depth-resolved band gap in Cu(In,Ga)(S,Se)$_2$ thin films", *Appl. Phys. Lett.* **93**, 244103 (2008).

[C03]   L. Weinhardt, O. Fuchs, M. Blum, M. Bär, M. Weigand, J. D. Denlinger, Y. Zubavichus, M. Zharnikov, M. Grunze, C. Heske, and E. Umbach, "Resonant x-ray emission spectroscopy of liquid water: novel instrumentation, high resolution, and the 'map' approach", *J. Electron. Spectrosc. Relat. Phenom., in print* doi:10.1016/j.elspec.2009.02.014 (2009).

[C04]   S. Pookpanratana, M. Bär, L. Weinhardt, C. Heske, R. France, T. D. Moustakas, O. Fuchs, M. Blum, W. Yang, and J. D. Denlinger, "Intermixing and chemical structure at the interface between n-GaN and V-based contacts", *Appl. Phys. Lett.* **93**, 172106 (2008).

[C05]   L. Weinhardt, O. Fuchs, A. Fleszar, M. Bär, M. Blum, M. Weigand, J. D. Denlinger, W. Yang, W. Hanke, E. Umbach, and C. Heske, "Resonant inelastic soft x-ray scattering of CdS: A two-dimensional electronic structure map approach", *Phys. Rev. B* **79** 165305 (2009).

[C06]   L. Weinhardt, O. Fuchs, E. Umbach, C. Heske, A. Fleszar, W. Hanke, and J. D. Denlinger, "Resonant inelastic soft x-ray scattering, x-ray absorption spectroscopy, and density functional theory calculations of the electronic band structure of CdS", *Phys. Rev. B* **75**, 165207 (2007).

[C07]   L. Weinhardt, M. Blum, M. Bar, C. Heske, O. Fuchs, E. Umbach, J. D. Denlinger, K. Ramanathan, and R. Noufi, "Chemical properties of the $Cu(In,Ga)Se_2$/MO/glass interfaces in thin film solar cells", *Thin Solid Films* **515**, 6119 (2007).

[C08]   L. Weinhardt, O. Fuchs, A. Peter, E. Umbach, C. Heske, J. Reichardt, M. Bär, I. Lauermann, I. Kötschau, A. Grimm, S. Sokoll, M. C. Lux-Steiner, T. P. Niesen, S. Visbeck, and F. Karg, "Spectroscopic investigation of the deeply buried $Cu(In,Ga)(S,Se)_2$/Mo interface in thin-film solar cells", *J. Chem. Phys.* **124**, 074705 (2006).

[C09]   L. Weinhardt, O. Fuchs, D. Gross, E. Umbach, C. Heske, N. G. Dhere, A. A. Kadam, and S. S. Kulkarni, "Surface modifications of $Cu(In,Ga)S_2$ thin film solar cell absorbers by KCN and H_2O_2/H_2SO_4 treatments", *J. Appl. Phys.* **100**, 024907 (2006).

[C10]   L. Weinhardt, O. Fuchs, D. Gross, G. Storch, N. G. Dhere, A. A. Kadam, S. S. Kulkarni, S. Visbeck, T. P. Niesen, F. Karg, C. Heske, and E. Umbach, "Comparison of band alignments at various $CdS/Cu(In,Ga)(S,Se)_2$ interfaces in thin film solar cells", *Conference Record of the 2006 IEEE 4th World Conference on Photovoltaic Energy Conversion, Vols 1 and 2*, 412 (2006).

[C11]   D. Eich, O. Fuchs, U. Groh, L. Weinhardt, R. Fink, E. Umbach, C. Heske, A. Fleszar, W. Hanke, E. K. U. Gross, C. Bostedt, T. Von Buuren, N. Franco, L. J. Terminello, M. Keim, G. Reuscher, H. Lugauer, and A. Waag, "Resonant inelastic soft x-ray scattering of Be chalcogenides", *Phys. Rev. B: Condens. Matter Mater. Phys.* **73**, 115212 (2006).

[C12]   M. Bär, L. Weinhardt, O. Fuchs, J. Klaer, J. Peiser, H. W. Schock, and C. Heske, "Chemical bath deposition of CdS thin films on CuInS2 and Si substrates — A comparative X-ray emission study", *Conference Record of the 2006 IEEE 4th World Conference on Photovoltaic Energy Conversion, Vols 1 and 2*, 416 (2006).

[C13]   Y. Zubavichus, M. Zharnikov, Y. J. Yang, O. Fuchs, E. Umbach, C. Heske, and M. Grunze, "Oxygen K-edge X-ray absorption fine structure studies of vacuum-deposited ice films", *Langmuir* **22**, 7241 (2006).

[C14]   L. Weinhardt, O. Fuchs, D. Gross, G. Storch, E. Umbach, N. G. Dhere, A. A. Kadam, S. S. Kulkarni, and C. Heske, "Band alignment at the CdS/Cu(In,Ga)S$_2$ interface in thin-film solar cells", *Appl. Phys. Lett.* **86**, 062109 (2005).

[C15]   Y. Zubavichus, M. Zharnikov, Y. J. Yang, O. Fuchs, C. Heske, E. Umbach, G. Tzvetkov, F. P. Netzer, and M. Grunze, "Surface chemistry of ultra-thin films of histidine on gold as probed by high-resolution synchrotron photoemission", *J. Phys. Chem. B* **109**, 884 (2005).

[C16]   J. Reichardt, M. Bär, A. Grimm, I. Kötschau, I. Lauermann, S. Sokoll, M. C. Lux-Steiner, C. H. Fischer, C. Heske, L. Weinhardt, O. Fuchs, C. Jung, W. Gudat, T. P. Niesen, and F. Karg, "Inducing and monitoring photoelectrochemical reactions at surfaces and buried interfaces in Cu(In,Ga)(S,Se)$_2$ thin-film solar cells", *Appl. Phys. Lett.* **86**, 172102 (2005).

[C17]   M. Odelius, H. Ogasawara, D. Nordlund, O. Fuchs, L. Weinhardt, F. Maier, E. Umbach, C. Heske, Y. Zubavichus, M. Grunze, J. D. Denlinger, L. G. M. Pettersson, and A. Nilsson, "Ultrafast core-hole-induced dynamics in water probed by x-ray emission spectroscopy", *Phys. Rev. Lett.* **94**, 227401 (2005).

[C18]   Y. Zubavichus, M. Zharnikov, A. Shaporenko, O. Fuchs, L. Weinhardt, C. Heske, E. Umbach, J. D. Denlinger, and M. Grunze, "Soft X-ray induced decomposition of phenylalanine and tyrosine: A comparative study", *J. Phys. Chem. A* **108**, 4557 (2004).

[C19]   Y. Zubavichus, O. Fuchs, L. Weinhardt, C. Heske, E. Umbach, J. D. Denlinger, and M. Grunze, "Soft x-ray-induced decomposition of amino acids: An XPS, mass spectrometry, and NEXAFS study", *Radiat. Res.* **161**, 346 (2004).

[C20]   T. Strunskus, O. Fuchs, L. Weinhardt, C. Heske, M. Guraya, M. Muhler, V. Staemmler, and C. Wöll, "The valence electronic structure of zinc oxide powders as determined by X-ray emission spectroscopy: variation of electronic structure with particle size", *J. Electron Spectrosc. Relat. Phenom.* **134**, 183 (2004).

[C21]   Y. Zubavichus, M. Zharnikov, Y. J. Yang, O. Fuchs, E. Umbach, C. Heske, A. Ulman, and M. Grunze, "X-ray photoelectron spectroscopy and near-edge X-ray absorption fine structure study of water adsorption on pyridine-terminated thiolate self-assembled monolayers", *Langmuir* **20**, 11022 (2004).

[C22]   Y. Zubavichus, Y. J. Yang, M. Zharnikov, O. Fuchs, T. Schmidt, C. Heske, E. Umbach, G. Tzvetkov, F. P. Netzer, and M. Grunze, "Local structure of amorphous ice as revealed by OK-edge EXAFS", *ChemPhysChem* **5**, 509 (2004).

[C23]   G. Tzvetkov, G. Koller, Y. Zubavichus, O. Fuchs, M. B. Casu, C. Heske, E. Umbach, M. Grunze, M. G. Ramsey, and F. P. Netzer, "Bonding and structure of glycine on ordered Al_2O_3 film surfaces", *Langmuir* **20**, 10551 (2004).

[C24]   C. Heske, U. Groh, O. Fuchs, L. Weinhardt, E. Umbach, T. Schedel-Niedrig, C. H. Fischer, M. C. Lux-Steiner, S. Zweigart, T. P. Niesen, and F. Karg, "Monitoring chemical reactions at a liquid-solid interface: Water on $CuIn(S,Se)_2$ thin film solar cell absorbers", *J. Chem. Phys.* **119**, 10467 (2003).

[C25]   L. Weinhardt, T. Gleim, O. Fuchs, C. Heske, E. Umbach, M. Bar, H. J. Muffler, C. H. Fischer, M. C. Lux-Steiner, Y. Zubavichus, T. P. Niesen, and F. Karg, "CdS and $Cd(OH)_2$ formation during Cd treatments of $Cu(In,Ga)(S,Se)_2$ thin-film solar cell absorbers", *Appl. Phys. Lett.* **82**, 571 (2003).

[C26]   C. Heske, U. Groh, O. Fuchs, L. Weinhardt, E. Umbach, M. Grun, S. Petillon, A. Dinger, C. Klingshirn, W. Szuszkiewicz, and A. Fleszar, "Studying the local chemical environment of sulfur atoms at buried interfaces in CdS/ZnSe superlattices", *Appl. Phys. Lett.* **83**, 2360 (2003).

[C27]   C. Barglik-Chory, D. Buchold, M. Schmitt, W. Kiefer, C. Heske, C. Kumpf, O. Fuchs, L. Weinhardt, A. Stahl, E. Umbach, M. Lentze, J. Geurts, and G. Müller, "Synthesis, structure and spectroscopic characterization of water-soluble CdS nanoparticles", *Chem. Phys. Lett.* **379**, 443 (2003).

[C28]   I. Lauermann, M. Bär, A. Ennaoui, U. Fiedeler, C.-H. Fischer, A. Grimm, I. M. Kötschau, M. C. Lux-Steiner, J. Reichardt, B. R. Sankapal, S. Siebentritt, S. Sokoll, L. Weinhardt, O. Fuchs, C. Heske, C. Jung, W. Gudat, F. Karg, and T. P. Niesen, "Analysis of zinc compound buffer layers in Cu(In,Ga)(S,Se)2 thin film solar cells by synchrotron-based soft X-ray spectroscopy", *Mat. Res. Soc. Symp. Proc. Vol.* **763**, ISBN 1-55899-700-8, p. 610-613 (2003).

[C29]   C. Heske, U. Groh, L. Weinhardt, O. Fuchs, B. Holder, E. Umbach, C. Bostedt, L. J. Terminello, S. Zweigart, T. P. Niesen, and F. Karg, "Damp-heat induced sulfate formation in Cu(In,Ga)(S,Se)$_2$-based thin film solar cells", *Appl. Phys. Lett.* **81**, 4550 (2002).

[C30]   C. Heske, U. Groh, O. Fuchs, E. Umbach, N. Franco, C. Bostedt, L. J. Terminello, R. C. C. Perera, K. H. Hallmeier, A. Preobrajenski, R. Szargan, S. Zweigart, W. Riedl, and F. Karg, "X-ray emission spectroscopy of Cu(In,Ga)(S,Se)$_2$-based thin film solar cells: Electronic structure, surface oxidation, and buried interfaces", *Phys. Stat. Sol. A — Appl. Res.* **187**, 13 (2001).

. . . and 17 publications in conference proceedings and annual reports.

ACKNOWLEDGMENT

Last but not least, I want to thank all people who contributed to this thesis! Many thanks to:

- Prof. Dr. Eberhard Umbach for his constant enthusiasm for novel experimental results in spite of his equally constant (no, worse: constantly increasing!) heavy workload. Thanks for the opportunity to contribute with my thesis to such an intriguing field of research!

- Prof. Dr. Kai Fauth for volunteering to be the second assessor of this thesis.

- Prof. Dr. Georg Reents for being the third assessor during my defense and for helping to solve a theoretical aspect on diffraction gratings.

- Prof. Dr. Clemens Heske and his family for their hospitality and support. The best place to stay in Vegas!

- Dr. Lothar Weinhardt for his inspiring ideas. And for the black humor he develops during frustrating beam times, making even those a lot of fun!

- Dr. Jonathan Denlinger for his uncanny dedication to make beamline 8 the best of all.

- Moni Blum for making the first pH-dependent spectra possible.

- Dr. Leeor Kronik for sharing the DFT calculations on the PTCDA molecule.

- Dr. Zahid Hussain and Phil Batson for accepting all of my crazy ideas and changes on the spectrometer design.

- Michael Jones (Gideon) for his careful machining and assembling of the spectrometer, for his technical advice and support.

- Dr. Yi-De Chuang for sharing his experience with 'his' spectrometers.

- Prof. Dr. Franz Himpsel for lending his nanoscience endstation for the first experiments with the new spectrometer.

- My family for their love and understanding even in times of heavy workload.